Department of Physics and Astronomy
Heidelberg University

Bachelor Thesis in Physics
submitted by

Maurice Rieger

born in Koblenz (Germany)

2023

Magnetic field characterisation and spin manipulation in ultracold dysprosium using radio-frequency driving and AC Stark shifts

This Bachelor Thesis has been carried out by Maurice Rieger
at the Physikalisches Institut in Heidelberg
under the supervision of
Prof. Dr. Lauriane Chomaz

Ruprecht Karl University of Heidelberg

Magnetic field characterisation and spin manipulation in ultracold dysprosium using radio-frequency driving and AC Stark shifts

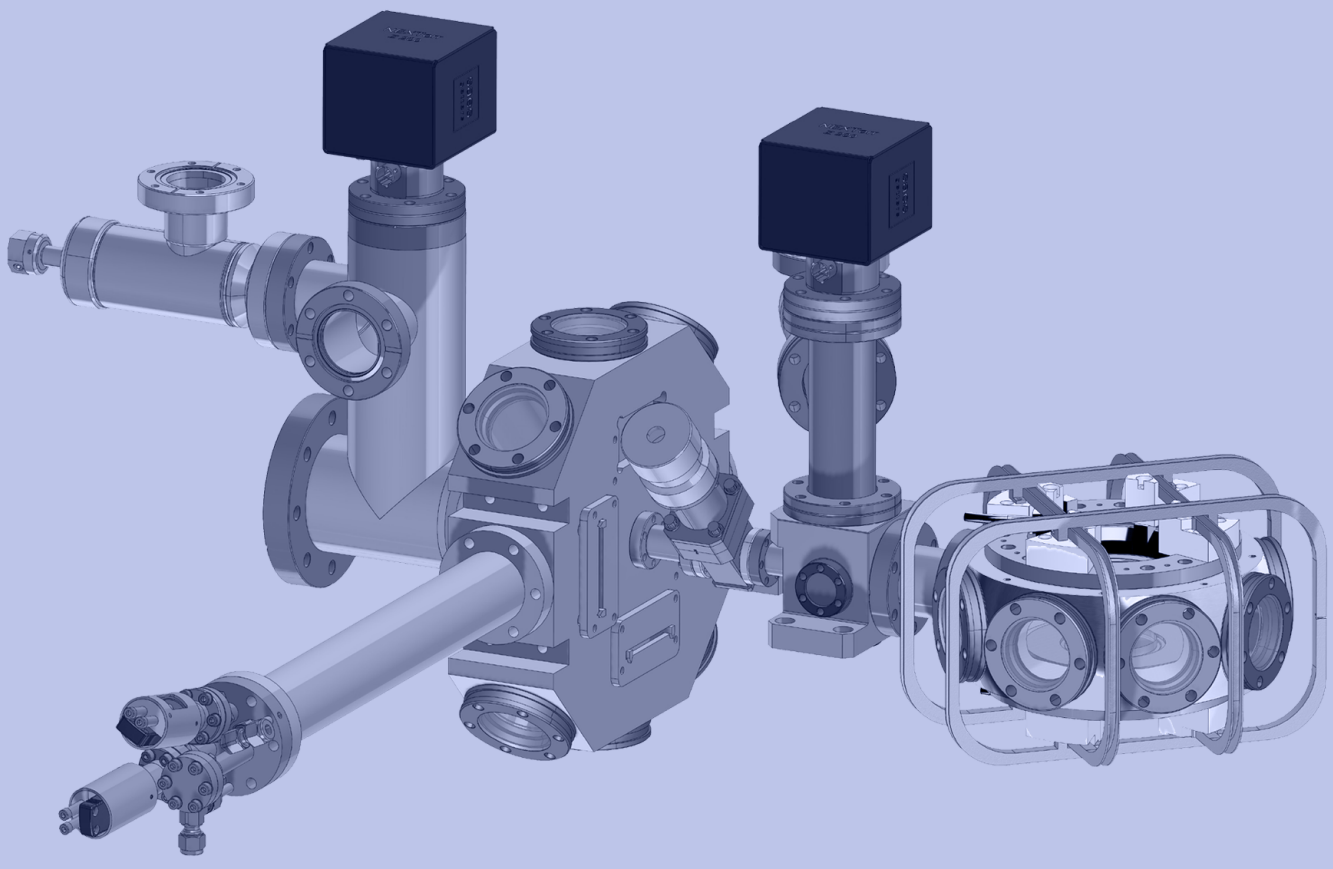

This Bachelor Thesis has been carried out by Maurice Rieger at the
Physikalisches Institut in Heidelberg under the supervision of
Prof. Dr. Lauriane Chomaz

Abstract

The Quantum Fluids group is involved in the study of ultracold dysprosium and the quantum phenomena that arise.

In this Bachelor Thesis a radio frequency spectroscopy setup is developed which allows to characterise the magnetic field of the science chamber coils in the experimental setup without breaking the vacuum. Furthermore, the possibility to drive Rabi oscillations in dysprosium 17-state systems is described, which can be used for spin preparation of the atoms in suitable cases. Impedance matching of the RF coil and the nonlinearity of the AC Stark effect are discussed as possibilities to make these oscillations experimentally measurable. The implementation of a Stark effect laser requires the use of dichroic mirrors, which are characterised with respect to their influence on the wavefront.

Zusammenfassung

Die Quantum Fluids Gruppe beschäftigt sich mit der Untersuchung von ultrakaltem Dysprosium und den dabei aufkommenden Quantenphänomenen.

In dieser Bachelor Thesis wird ein Radiofrequenzspektroskopie-Setup entwickelt, mit dem das Magnetfeld der Experimentierkammerspulen im experimentellen Aufbau charakterisiert werden kann, ohne dabei das Vakuum brechen zu müssen. Es wird die Möglichkeit beschrieben, Rabi-Oszillationen im Dysprosium 17-Zustands-System anzuregen, welche in geeigneten Fällen zu einer Spinpräparation der Atome genutzt werden können. Um diese Oszillationen experimentell messbar zu machen, werden Impedanzanpassung der RF Spule und die Nichtlinearität des AC Stark Effekts als mögliche Methoden diskutiert. Zur Implementierung eines Stark Effekt Lasers ist die Verwendung dichroitischer Spiegel notwendig, deren Einfluss auf die Wellenfront einfallenden Lichts charakterisiert wird.

Contents

1 Thesis Introduction

1.1 Motivation

The history of ultracold quantum gases dates back to 1924, when Albert Einstein predicted the existence of a new state of matter for atoms with integer spin in the ultracold regime on the basis of a paper by Satyendranath Bose [Ein05]. This state of matter is a Bose-Einstein condensate (BEC), however, its experimental realisation took more than 70 years. The reason for this was that the methods of cooling atoms still had to be developed at the time of the prediction. With the invention of the laser in 1960 by Theodore Maiman, the door to laser cooling was opened [KS08]. In the 1980s, the first working magneto optical trap and optical dipole trap were constructed [Krz+10] [Mat09]. Finally, in 1995, the experimental realisation of a BEC was achieved in sodium and rubidium [And+95]. Since the first BEC, many more atoms have been successfully condensed and even molecules, quasi-particles, and photons [Kla+10]. The original prediction of a BEC was made under the assumption of zero atomic interaction, however this condition cannot be realised in experiment. Instead, the study of interactions in BECs has contributed to the discovery of new quantum phenomena like generation of quantized vortices and new phase transitions in ultracold quantum gases in the past decades [FS01] [Lev02].

One atomic family has recently been of particular interest. These are atoms with a large magnetic moment. The presence of magnetic dipoles offers, in addition to the ever-present short-range interaction, another anisotropic long-range interaction. With the help of a magnetic field, the strength of these two interactions can be controlled. This property led to the discovery of new quantum phenomena, such as supersolidity or the formation of droplet crystals [Cho+22]. The Quantum Fluids group in Heidelberg, founded in 2021 and led by Prof. Dr. Lauriane Chomaz, is investigating these phenomena in the case of dysprosium, which has the largest magnetic moment in the periodic table.

Due to it's crucial role in tuning the short-range and long-range interaction strength, the magnetic field at the position of the atoms should be properly characterized. Since the experimental chamber is under ultra-high vacuum, a measurement method must be chosen that can be performed outside

the vacuum and still give meaningful results. This is one of several possible applications of radio frequency spectroscopy that will be discussed in this thesis.

Another research interest in the field of ultracold atoms is spin physics. In particular, the investigation of spin mixtures of two different states or the investigation of dipolar spin exchange processes in spin polarised systems can lead to novel results. The preparation of such spin states can also be achieved by radio frequency spectroscopy, which is discussed as another possible application in the course of this thesis.

1.2 Thesis overview

After giving an overview of dysprosium and the experimental setup in the laboratory in section 2, the structure of this thesis is divided into four parts.

The aim of part A is to characterise three magnetic field coils at the experimental chamber using radio frequency spectroscopy. In section 3 the behaviour of dysprosium atoms in a radio frequent magnetic field is discussed. In section 4 a radio frequency coil is designed and implemented in the experiment. The actual characterisation of the magnetic field will follow in section 5.

In part A, it will be shown that oscillations in the occupation probability of the energy levels - that split equidistantly due to the Zeeman effect - occur by means of radio frequency magnetic fields. The aim of part B is to discuss possibilities of making these oscillations experimentally measurable, which allows to prepare specific pure or mixed spin states. In section 6 dipolar relaxation is explained as a cause for the absence of oscillations in test measurements. The next two sections 7 and 8 present two possible options to make oscillations in dysprosium measurable despite dipolar relaxation. These are impedance matching of the RF coil and the installation of an additional laser, which uses the non-linearity of the AC Stark shift in dysprosium.

For the experimental implementation of the Stark shift laser, it is necessary to superimpose two different laser beams due to the limited optical accessibility of the atoms in the experimental chamber. For this purpose, dichroic mirrors can be used, which are characterised in part C. In section 9, an interferometric setup is developed that can measure the wavefront distortion by the dichroic mirror. In section 10, two dichroic mirrors with different thicknesses are characterised for their transmitting and reflecting wavelengths.

Finally, part D is formed by the summary in section 11 and the appendix A. In the appendix, some long calculations are outsourced, additional physical phenomena are explained and the technical drawings as well as snippets of important Python or C++ code made in the course of this thesis are included.

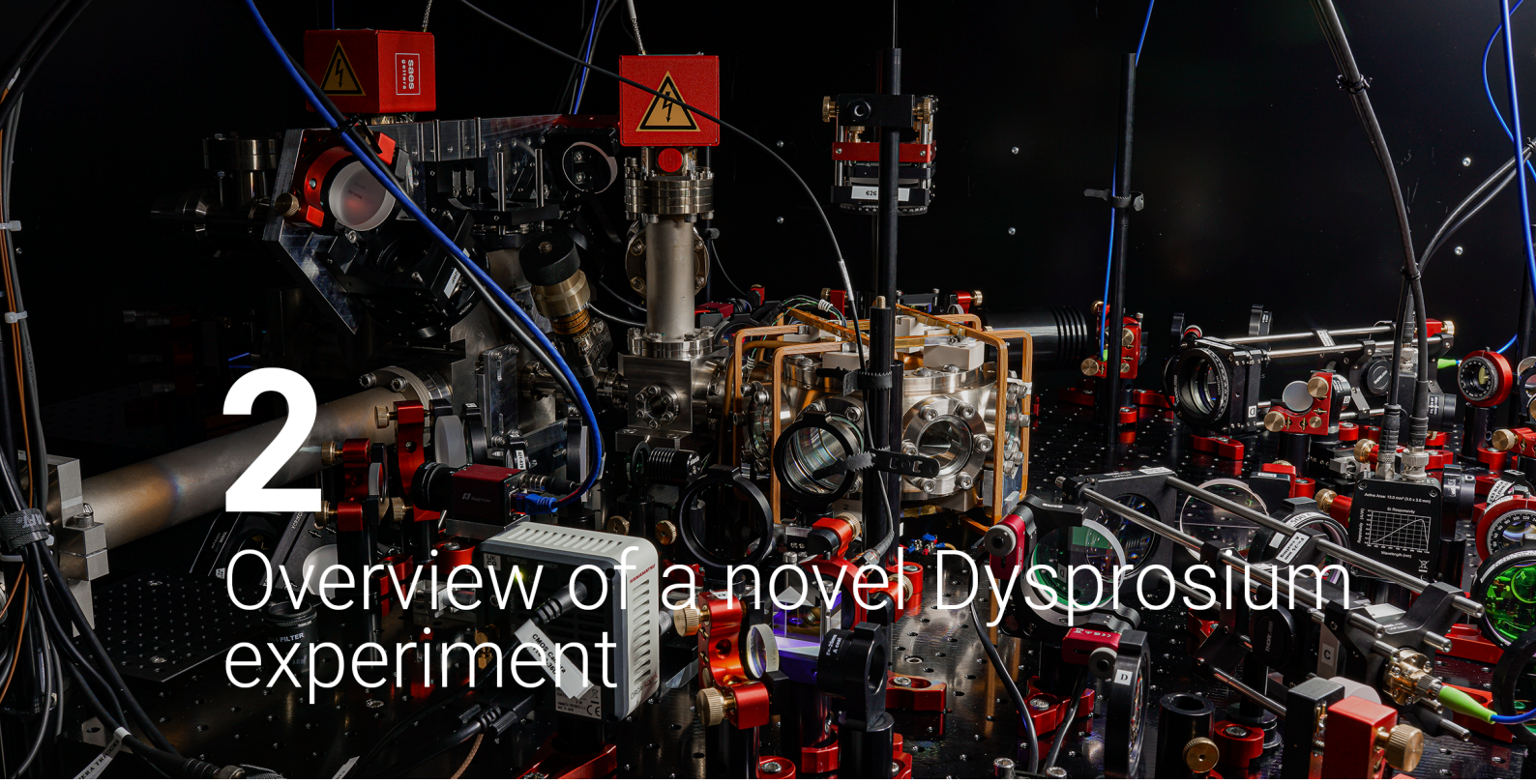

2 Overview of a novel Dysprosium experiment

Introduction

This section gives an introduction to the dysprosium laboratory in Heidelberg. For this purpose, the properties of dysprosium concerning the atomic electron configuration and the magnetic moment are considered in subsection 2.1 and 2.2. In subsection 2.3 several phenomena are mentioned which demonstrate why the study of dysprosium is of particular interest, including especially the tuneable short-range and long-range interactions. In subsection 2.4 an overview of the experimental setup is given, with the last paragraph referring to the work of my group for further reading. Finally, in subsection 2.5 the theory is put into context with the experimental setup, illustrating the perspective of the experiment.

2.1 Basic properties and electron configuration of Dysprosium

Dysprosium is an element of the periodic table with atomic number 66, which therefore belongs to the lanthanides. Since dysprosium is a very base metal, it has a high reactivity and therefore does not usually occur in its pure form in nature. Instead, oxides or alloys of this material are found. After a complex purification process, a mixture of the dysprosium isotopes $^{156}\mathrm{Dy}$, $^{158}\mathrm{Dy}$, $^{160}\mathrm{Dy}$, $^{161}\mathrm{Dy}$, $^{162}\mathrm{Dy}$, $^{163}\mathrm{Dy}$, $^{164}\mathrm{Dy}$ is obtained, whereby only the last five mentioned above occur in relevant quantities [Ems11]. The most important properties of these isotopes are shown in table 1.

The electron ground state of dysprosium is given by $\mathrm{Dy} : [\mathrm{Xe}]\ 4\mathrm{f}^{10}\ 6\mathrm{s}^2$, where $[\mathrm{Xe}]$ describes the electron configuration of the noble gas xenon [Lid04] [NG00]. For the bosonic isotopes, which are of primary interest for the experiment, and assuming LS coupling, the dysprosium ground state can be described by the triplet of quantum numbers (L,S,J), where L is the orbital angular momentum, S is the spin and J is the total angular momentum.

The ground state can be derived from the electron configuration with the help of Hund's rules as

Isotope	^{160}Dy	^{161}Dy	^{162}Dy	^{163}Dy	^{164}Dy
Mass [u]	159.9251	160.9269	161.9267	162.9287	163.9291
Abundance [%]	2.34	18.9	25.5	24.9	28.2
Nuclear spin	0	5/2	0	5/2	0
Statistics	boson	fermion	boson	fermion	boson

Table 1: Atomic mass, percentual abundances, nuclear spin and quantum statistics of the most important naturally occurring dysprosium isotopes.

$L = 6$, $S = 2$ and $J = 8$. In spectroscopic notation $^{2S+1}L_J$, the ground state is denoted by $^5I_8$ in the following.

2.2 Magnetic moment and g-factor of Dysprosium

The magnetic moment of dysprosium is obtained from the magnetic quantum number m_J, the g-factor g_J and the Bohr magneton μ_B as

$$\mu = m_J g_J \mu_B \tag{2.1}$$

while the g-factor can be calculated approximately from the quantum numbers (L,S,J) as

$$\begin{aligned} g_J &= g_L \frac{J(J+1) - S(S+1) + L(L+1)}{2J(J+1)} + g_S \frac{J(J+1) + S(S+1) - L(L+1)}{2J(J+1)} \\ &\approx 1 + \frac{J(J+1) + S(S+1) - L(L+1)}{2J(J+1)} \\ &\approx 1.25. \end{aligned} \tag{2.2}$$

The approximation in the above equation is based on the assumption that $g_S \approx 2$ and $g_L = 1$. The last assumption is justified as the nuclear mass M of dysprosium as part of the lanthanides is very high in comparison to the electron mass m_e and the following relationship applies to the g-factor of the orbital angular momentum:

$$g_L = 1 - \frac{m_e}{M} \approx 1 \tag{2.3}$$

This result is in agreement with experimental measurements, which were able to determine the g-factor of dysprosium to be $g_J = 1.24$ [FDG74]. It also illustrates that the assumption of LS-coupling was justified in the determination of the ground state of dysprosium, which is important to know, since for atoms with higher atomic numbers jj-coupling becomes increasingly relevant.

2.3 Anisotropic dipolar interactions and Feshbach resonances in dysprosium Bose Einstein condensates

The working group in the framework of which this Bachelor Thesis was written deals with the investigation of ultracold dysprosium atoms. The dysprosium isotope ^{164}Dy is cooled down to a few nanokelvin in a science chamber. Due to the bosonic properties of dysprosium, almost all atoms

condense into the energetically lowest motional state and a Bose Einstein condensate (BEC) is formed [BDZ08].

The properties of ultracold quantum gases are usually determined by isotropic short-range interactions. These interactions are typically encompassed by a Lennard Jones Potential which is the sum of a repulsion $\sim r^{-12}$ at a short range and at longer range, a van der Waals (VdW) potential of the form

$$V_{\mathsf{VdW}} = -\frac{C_6}{r^6} \tag{2.4}$$

with C_6 being the VdW coefficient and r being the length of the connection vector $\vec{r}$ of both atoms. The physical basis of this interaction are induced electric dipoles in the two interacting atoms. In the limit of ultracold atoms, the contact interaction can be described by a pseudopotential [Cho+22]

$$V_{\mathsf{cont}}(\vec{r}) = \frac{4\pi\hbar^2 a_{\mathsf{S}}}{M}\,\delta(\vec{r}) \tag{2.5}$$

with the mass M of the dysprosium atoms, the reduced Plank constant $\hbar$ and the s-wave scattering length a_{S}. The scattering length depends on the magnetic field strength

$$a_S = a_{\mathsf{B}}\left(1 - \frac{\Delta_{\mathsf{F}}}{B - B_0}\right) \tag{2.6}$$

where a_{B} is the background scattering length, B is the magnetic field strength and B_0 the position of a Feshbach resonance of width Δ_{F} [Fes58] [Chi+10] [GGP02]. Thus, manipulation of the magnetic field strength allows tuning the short-range interactions in equation (2.5).

Dysprosium and holmium, are the elements of the periodic table with the strongest dipole moment. In the regime of ultracold quantum gases, this has the consequence of an additional long-range and anisotropic interaction whose potential in a fully polarised system is given by [Cho+22]

$$V_{\mathsf{dip}} = \frac{C_{\mathsf{dip}}}{4\pi}\,\frac{1 - 3\,\cos^2(\theta)}{|\vec{r}|^3} \tag{2.7}$$

where C_{dip} is the interaction strength and θ is the angle between the connection vector $\vec{r}$ and the polarisation axis of two dipoles. The interaction strength can be calculated from the vacuum permeability μ_0 and the magnetic moment of dysprosium μ as $C_{\mathsf{dip}} = \mu_0\mu^2$.

The presence of these two interactions in the short-range and long-range regime is of particular interest due to the possibility of tuning them by means of a magnetic field, whereby the field strength influences the short-range interactions and the orientation influences the long-range interactions.

2.4 Experimental setup

The following section will give an overview of the experimental set-up of the main experiment in the dysprosium laboratory. The experimental setup with its most important components marked is shown in figure 1.

To extensively study the unique phenomena of ultracold dysprosium quantum gases firstly a dysprosium source is needed. The source itself is given by a dysprosium sample in a furnace [I]. The

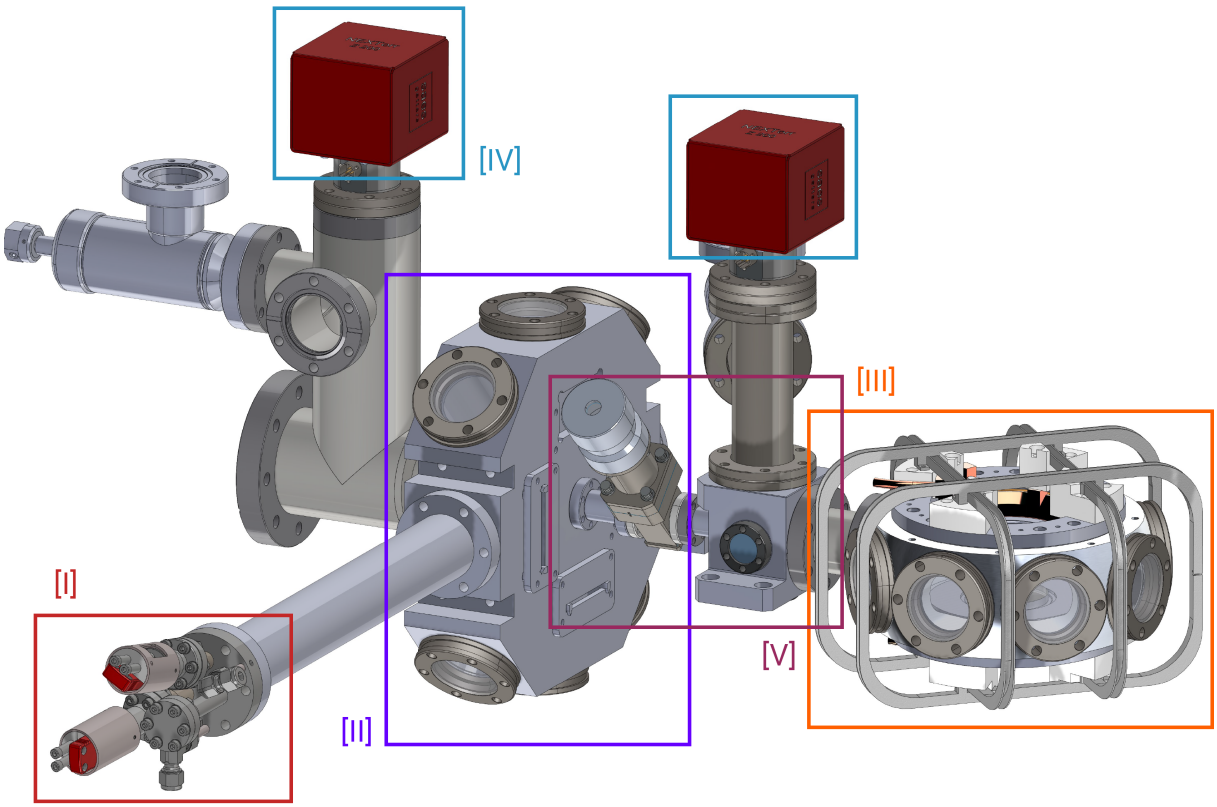

Figure 1: Experimental setup of a novel dysprosium experiment. [I] Dysprosium oven. [II] Titanium chamber with 2D MOT. [III] Experimental chamber with 3D MOT, compensation cage and Helmholtz coils (see figure 2). [IV] Ion vacuum pumps. [V] Differential pumping stage.

dysprosium sample is not purified, but rather a mixture of the different isotopes, where the frequency of occurrence corresponds to the natural frequency in table 1. Dysprosium has a melting temperature of $T = 1680\,\mathrm{K}$ and a vaporisation temperature of $T = 2873\,\mathrm{K}$. The furnace heats up the dysprosium to about $T \approx 1300\,\mathrm{K}$, so no change in the state of aggregation occurs yet, but enough dysprosium evaporates from the surface, that is fed through a water cooled connecting tube into the 2D MOT [II] [Klu19].

In the 2D MOT 8 permanent magnets are used to generate a specific magnetic field structure. The 2D MOT chamber is made of titanium to minimise the influence on the magnetic field and is mounted vertically in the experimental setup. The 2D MOT serves as a decelerator and purifier for the dysprosium raw material by using an atomic transition, so only the bosonic dysprosium used in the experiment is decelerated. The atomic transition necessary for this deceleration occurs at about $\lambda = 421.29\,\mathrm{nm}$, with a large natural linewidth of $\Delta\nu = 32.2\,\mathrm{MHz}$ and therefore a short lifetime of $\tau = 4.94\,\mathrm{ns}$ of the excited state, see e.g. [Ilz+18]. Therefore this 2D MOT configuration allows a fast deceleration of the hot dysprosium atoms and makes a Zeeman slower obsolete.

The dysprosium atoms are transferred into a 3D MOT [III] after the initial deceleration by the 2D MOT. Since the atoms in the 2D MOT are only held in a two-dimensional plane, but not along the orthogonal axis, the atoms are in theory able to diffuse into the 3D MOT. However, to increase the loading efficiency of the 3D MOT and to accelerate the loading, an additional push beam was installed along the orthogonal axis, which operates at a wavelength of $\lambda = 626.082\,\mathrm{nm}$. The 3D MOT also uses this much narrower band atomic transition for cooling at a wavelength of $\lambda = 626.082\,\mathrm{nm}$ with a linewidth of $\Delta\nu = 135\,\mathrm{kHz}$ corresponding to a longer lifetime of $\tau = 1.2\,\mu\mathrm{s}$, see e.g. [Ilz+18].

Due to the oven and the evaporation of the dysprosium, it is not possible to achieve an ultra-high vacuum inside the 2D MOT chamber, but rather only a high vacuum. However, since an ultra-high vacuum is necessary for the physical experiments in the 3D MOT, the 2D and 3D MOT are separated by a differential pumping stage (DPS) [V]. This allows a pressure gradient to be created between the two chambers. Under normal operation (with evaporation of the dysprosium in the furnace), a pressure of $p \approx 2 \cdot 10^{-9}$ mbar in the 2D MOT and a pressure of $p \lesssim 10^{-11}$ mbar in the 3D MOT can be kept stable by means of ion pumps [IV].

Compared to the 2D MOT chamber, the experimental chamber is not made of titanium but of stainless steel. Furthermore, the magnetic field is not generated by permanent magnets but by coils, since strength and orientation have to be varied for tuning the atomic interactions. In figure 2 a cross-section of the experimental chamber is shown, highlighting in particular a pair of water-cooled Helmholtz and anti-Helmholtz coils along the z direction (defining z as vertical axis). In addition, one recognises another small field (SF) coil with one turn. The viewports in the z direction are designed to provide high optical access even at an angle. This is particularly relevant since, at the time of writing this bachelor thesis, high precision imaging is being installed in the z direction. Besides the coils displayed in figure 2, the entire experimental chamber is surrounded by a compensation cage, which allows manipulation of the magnetic field in the x-y plane and is visible in figure 1.

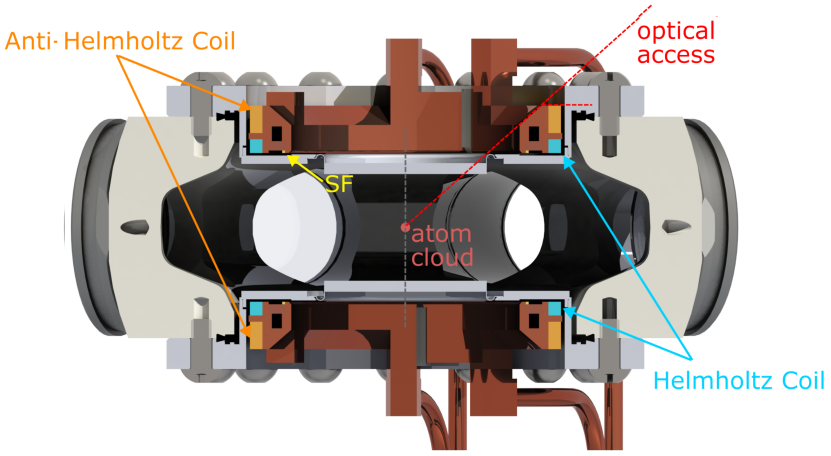

Figure 2: Cross-section of the experimental chamber including the internally mounted Helmholtz coils (cyan), anti-Helmholtz coils (orange) and small field (SF) coils (yellow). The atomic cloud is shown in the center of the chamber (red). This figure has been taken and modified from [Sch22].

However, the 3D MOT alone is not capable of cooling the dysprosium atoms to the point where a BEC formation occurs, since the minimal temperature that has be reached in the experiment is $T \approx 15\,\mu$K. Also, the tuning of the contact interactions should not influence the trapping of the atoms. For a magnetic field-independent atom trap which is able to reach BEC formation temperatures, the use of a crossed optical dipole trap (ODT) is suitable. Using this, temperatures of $T \approx 100\,$nK have been achieved. In order to avoid unwanted atomic transitions and to confine the quantum gas, a wavelength of the laser light with sufficient distance to resonances is chosen [GWO00]. This configuration is referred to below as far detuned. In the experiment, this condition is achieved by using an infrared (IR) laser with a wavelength $\lambda = 1064\,$nm. One of the next steps while writing this thesis is to reduce the dimensionality of the atoms with an optical accordion lattice that is operating far detuned at a wavelength of $\lambda = 532\,$nm. In addition, a digital micromirror device (DMD) setup will be build into the experiment, which will allow arbitrary potentials for trapping dysprosium BECs to be generated.

For more information regarding the setup and deep explanations of the physical principles of the phenomena only briefly touched upon here, I refer to the work of my research group. Concerning the vacuum setup including the 2D MOT field configuration I refer to Christian Gölzhäuser [Göl21]. Regarding the furnace and more information about the 2D MOT I refer to Jianshun Gao [Gao22]. For information on the magnetic coils and the 3D MOT I refer to Joschka Schöner [Sch22] and Lennart Hoenen [Hoe22]. The optical dipole trap was discussed in more detail by Paul Holzenkamp [Len22], while Valentina Salazar and Charles Drevon [Dre23] dealt with the development of an accordion lattice [Sal23]. For a development and characterisation of the DMD setup I refer to Thibault Bourgeois [Bou23].

2.5 Perspective of the experiment

Using bosonic dysprosium allows to make use of the tunability of a short-range interaction under the presence of a competing long-range interaction. Within the last years, these phenomena lead to exciting novel discoveries. Some of these arising exotic phenomena are supersolidity, topological ordering and the formation of droplets or droplet crystals. More information on the current state of research is given for example in [Cho+22].

The goal of the Dysprosium Laboratory under the supervision of Prof. Dr. Lauriane Chomaz is to study these phenomena in more detail. The experiment aims in particular to a reduction of the dimensionality of the dysprosium quantum gas by restricting it to two dimensions. With an accordion lattice, tailorable quasi 2D traps will be realised. The goal here is to investigate the underlying phase diagram and the dynamics of this dysprosium dipolar quantum system. The atomic densities will be probed with sub-micron resolution using a high resolution objective.

Interactive 3D model of the experiment

Under the adjacent QR code an animation of the experimental setup, as well as an interactive 3D model is provided.

For a better experience, viewing on a computer is recommended. To do this, simply click on the QR code or alternatively enter the following link into a browser: `https://www.maurice-rieger.de/experimental-setup`

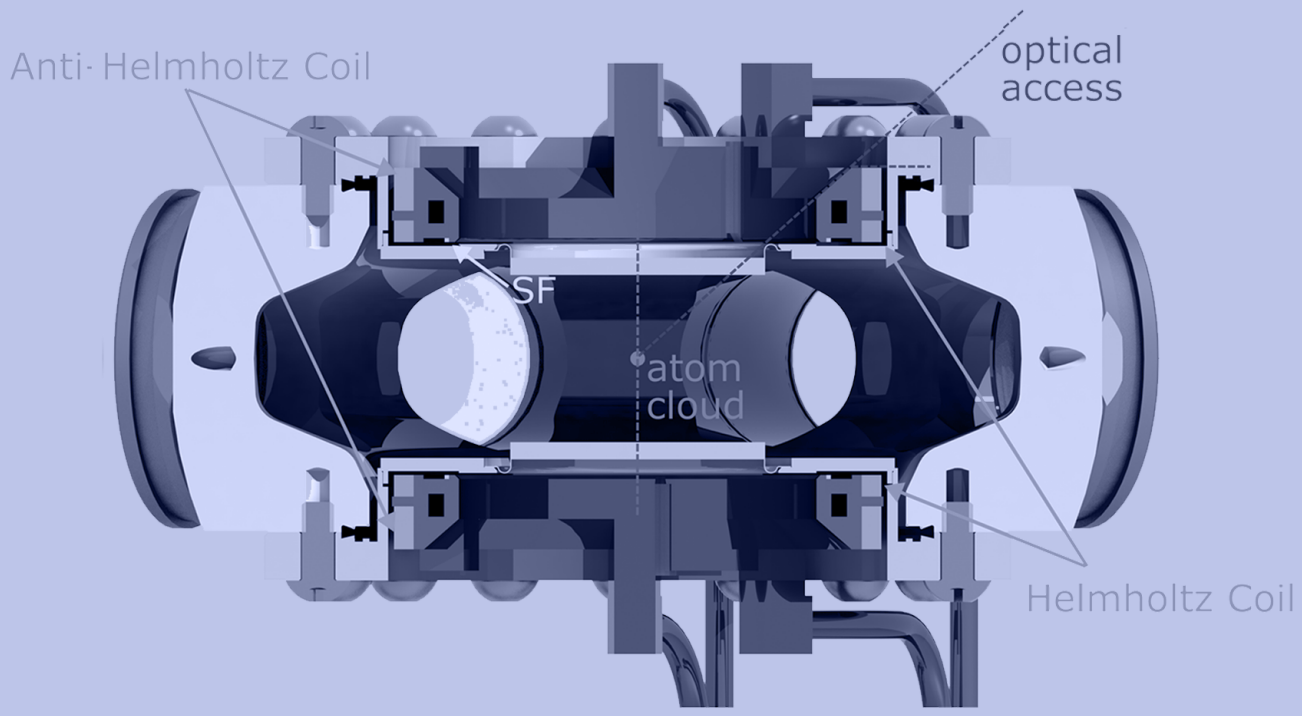

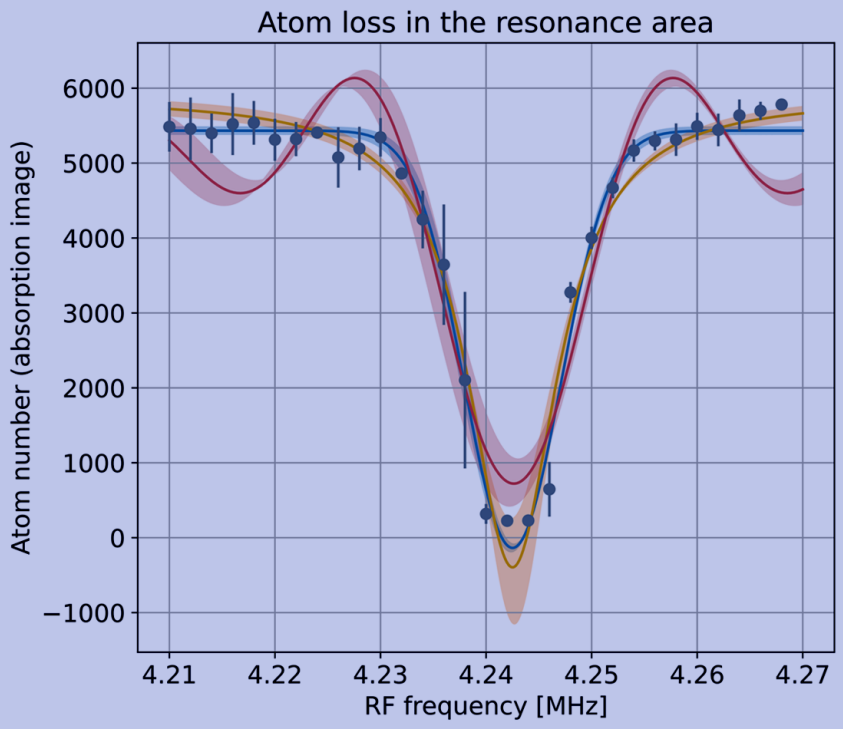

A

Radio frequency spectroscopy in ultracold dysprosium

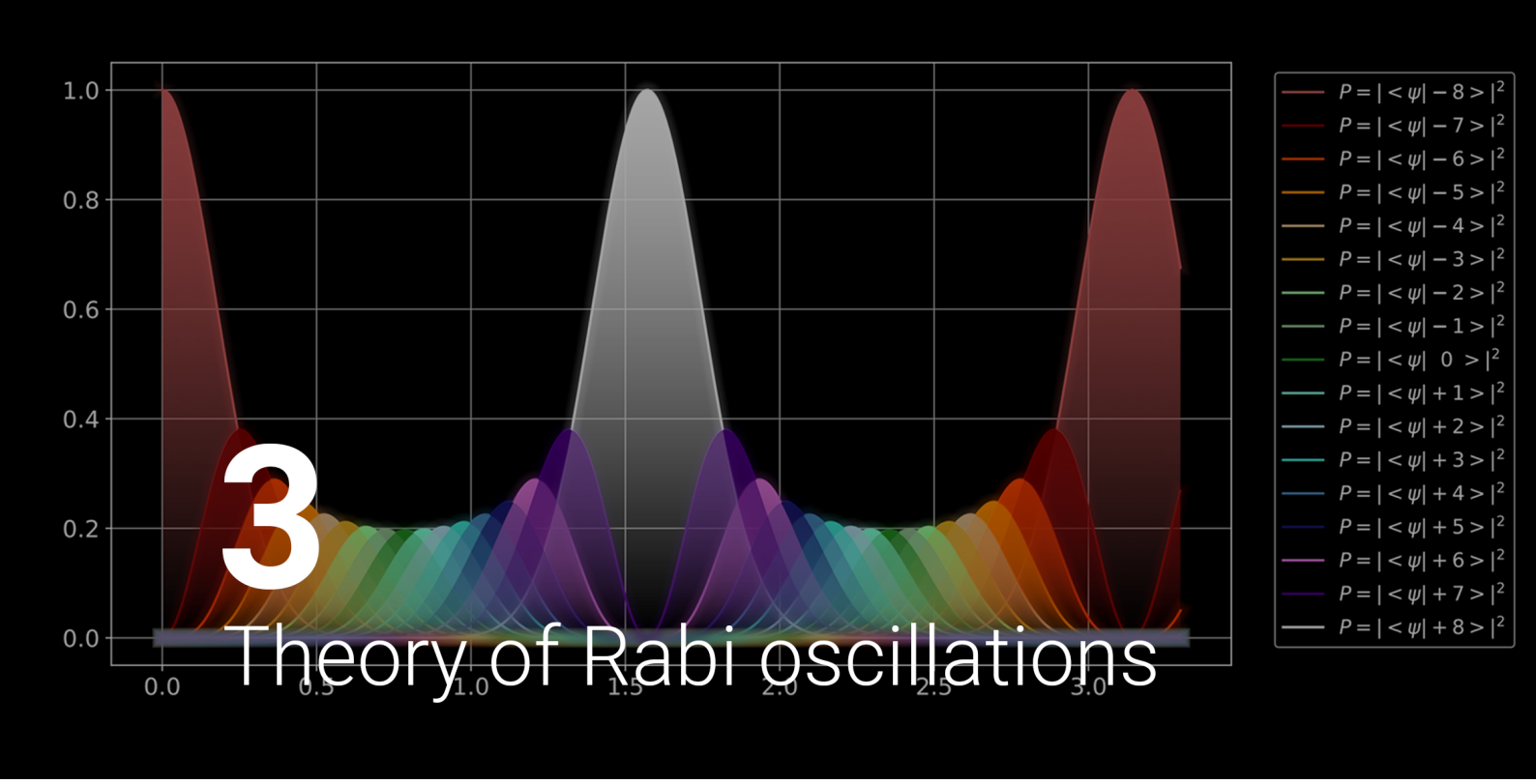

3 Theory of Rabi oscillations

Introduction

This chapter considers the behaviour of dysprosium atoms in a magnetic field. In particular, the Zeeman splitting is considered in subsection 3.1, which leads to an energetically equidistant splitting of the dysprosium ground state into 17 substates. In subsection 3.2 it is explained how individual substates in an atom can be coupled by means of a radio-frequency field orthogonal to the quantisation axis. Within this framework, a general Hamiltonian in the rotating wave approximation is derived. This is first evaluated in subsection 3.3 for a two-state system, where Rabi oscillations occur. This concept of Rabi oscillations is generalised to the dysprosium 17-state system in subsection 3.4. Two numerical methods are presented to determine the time evolution of the substate occupation probabilities and the influence of a detuning from the resonance frequency is investigated. It is shown that the occupation of the states is periodic in time, and the revival time can be determined analytically as a function of the detuning.

3.1 Zeeman effect

The Hamiltonian of an atom in a stationary magnetic field is generally given as

$$H = H_0 + H_B = H_0 + \vec{\mu} \cdot \vec{B} \tag{3.8}$$

where H_B is a perturbation of the field-free Hamiltonian H_0. Since this experiment focuses on phenomena in bosonic dysprosium, as explained in subsection 2.3, a nuclear spin of $I = 0$ is assumed below. This allows to calculate the total magnetic moment as

$$\vec{\mu} = \frac{\mu_B g_J}{\hbar} \vec{J}. \tag{3.9}$$

Starting from a vanishing magnetic field $|\vec{B}| = 0$ the ground state $^5\mathrm{I}_8$ of dysprosium is degenerated due to $m_J \in \{-J, \ldots, J\}$ for a given J and since $J = 8$ this leads to a total of 17 different degenerated energy levels. Choosing the direction of $\vec{B}$ as quantisation axis allows to find a common basis for H_0 and H_B. This basis is given as the different m_J states of the ground state $J = 8$ and will be denoted as $\psi_{m_J} = |m_J\rangle$. The energy of the different basis states ψ_{m_J} in case of a non-vanishing magnetic field $|\vec{B}| \neq 0$, with $\vec{B}$ oriented in the z direction, can be calculated as expectation value of the Hamilton operator:

$$\begin{aligned} E_J &= \langle \psi_{m_J} | H | \psi_{m_J} \rangle \\ &= \langle \psi_{m_J} | H_0 | \psi_{m_J} \rangle + \frac{\mu_B g_J B_z}{\hbar} \langle \psi_{m_J} | J_z | \psi_{m_J} \rangle \\ &= E_0 + \mu_B g_J B_z m_J \end{aligned} \tag{3.10}$$

In equation (3.10) E_0 has been defined as the energy of the ground state with vanishing field. The contribution of the perturbation is shown in figure 3 for magnetic field strengths up to $|\vec{B}| = 12\,\mathrm{G}$.

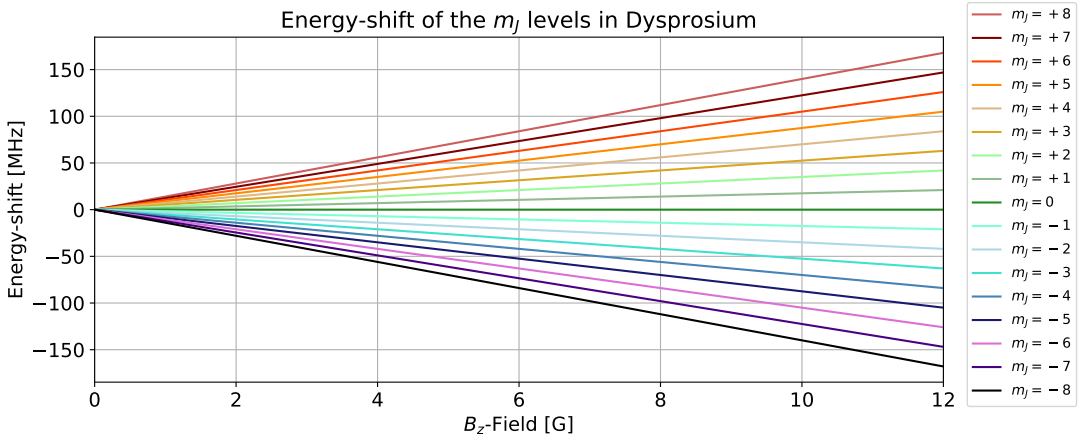

Figure 3: Energy shift of the 17 Zeeman sublevels in dysprosium in relation to the field free dysprosium ground state $^5\mathrm{I}_8$ for magnetic field strengths up to $|\vec{B}| = 12\,\mathrm{G}$ that are commonly used in the main experiment.

The energy shifts are shown to be in the megahertz regime for the field strengths relevant in the Dy experiment with a slope $m = 1.7495\,\mathrm{MHz/G}$ of the $m_J = 1$ state. The slopes of the other m_J states correspond exactly to m_J times the slope m, which results in an equidistant energy splitting.

Note that here the LS coupling scheme is assumed, which is only valid for magnetic field strengths below the $\sim 1\,\mathrm{T}$ regime. For stronger fields the coupling of orbital and spin angular momentum is disturbed and (J, m_J) are no longer appropriate quantum numbers[1].

3.2 Coupling the sublevels with a radio frequency field

Up to this point, only a static magnetic field in the z-direction has been considered where no coupling between the individual basis states ψ_{m_J} occurred. To cause a coupling between the individual basis states, a further oscillating field component orthogonal to the z-axis is required, see e.g.[GS18].

[1] In this case the Paschen Back regime is entered, which will not be further elaborated here.

Therefore a stationary B_z field and an additional oscillating radio frequency (RF) field B_{RF} are considered, the latter being defined as[2]

$$B_{\mathsf{RF}}(t) = B_{\mathsf{RF}} \cos(\omega t). \tag{3.11}$$

The Hamiltonian of the total magnetic field H_B can be expressed as

$$H_B = \omega_0 J_z + 4\Omega_{\mathsf{R}} \cos(\omega t) J_x \quad \text{with} \quad \omega_0 = \frac{\mu_B g_J B_z}{\hbar} \quad \text{and} \quad \Omega_{\mathsf{R}} = \frac{\mu_B g_J B_{\mathsf{RF}}}{4\hbar} \tag{3.12}$$

where ω_0 corresponds to the energy distance of the Zeeman sublevels and the Rabi frequency Ω_{R} has been defined. To solve the Hamiltonian in equation (3.12), properties of the angular momentum algebra are used. These allow to express the operators J_x and J_y as sum of their lowering and raising operator as

$$J_x = \frac{J_+ + J_-}{2} \quad \text{and} \quad J_y = \frac{J_+ - J_-}{2}. \tag{3.13}$$

The effect of lowering and raising operators $J_\pm$ on a basis state $|m_J\rangle$ is defined by

$$J_\pm |m_J\rangle = \hbar\sqrt{J(J+1) - m_J\,(m_J \pm 1)}\, |m_J \pm 1\rangle. \tag{3.14}$$

Using equation (3.13) and the exponential notation of the cosine, the Hamiltonian in equation (3.12) can be expressed as

$$H = \omega_0 J_z + \Omega_{\mathsf{R}} \left(e^{i\omega t} + e^{-i\omega t}\right) (J_+ + J_-). \tag{3.15}$$

In the following, a random state $|\psi\rangle$ is considered, which can be represented as a linear combination over the base states $|m_J\rangle$ with coefficients c_{m_J}. The time evolution of this state follows from the time-dependent Schrödinger equation

$$i\hbar\partial_t |\psi\rangle = H |\psi\rangle \quad \text{with} \quad |\psi\rangle = \sum_{m_J=-J}^{J} c_{m_J} |m_J\rangle. \tag{3.16}$$

However, in this representation of the general state, one gets rapidly oscillating coefficients c_{m_J} due to the time dependency of the Hamiltonian in equation (3.15). To circumvent this problem a unitary transformation into a rotating reference frame

$$U = \exp(i\omega t J_z) = \sum_{m_J=-J}^{J} \exp(i m_J \omega t)\, |m_J\rangle\langle m_J| \tag{3.17}$$

with angular frequency ω of the magnetic RF field oscillation is defined that acts on the arbitrary state $|\psi\rangle$ as well as on the Hamiltonian H with [Ste07]

[2] In the case of a time-varying total magnetic field $\vec{B}(t)$, the assumption that the magnetic dipole moment vectors of the dysprosium atoms align parallel along the magnetic field lines is no longer tenable, since in the general case it must be assumed that the time scale on which the magnetic field changes can be in the order of the relaxation time of the magnetic dipoles, see e.g. [Hor98].

$$|\tilde{\psi}\rangle = U\,|\psi\rangle \qquad \text{and} \qquad \tilde{H} = UHU^{\dagger} + i\hbar(\partial_t U)U^{\dagger}. \tag{3.18}$$

In the rotating wave approximation (RWA) all terms rotating with double the RF frequency are neglected [Dre17] which leads to the following expression for the Hamiltonian:

$$\tilde{H} = (\omega_0 - \omega)J_z + \Omega_{\mathsf{R}}\,(J_+ + J_-) = -\delta J_z + \Omega_{\mathsf{R}}\,(J_+ + J_-) \tag{3.19}$$

Here $\delta = (\omega - \omega_0)$ is defined as the RF detuning. The essential step, which was accomplished by the unitary transformation U, is the change from a time-dependent Hamiltonian H to a time-independent Hamiltonian $\tilde{H}$. The exact calculations and a more detailed explanation of the RWA can be found in the appendix in subsection A.1.1.

3.3 Two state Rabi oscillations

To obtain a better understanding of the underlying physics of Rabi oscillations, this subsection focuses on oscillations in a spin $\pm\frac{1}{2}$ system. The system has two states $|0\rangle$ and $|1\rangle$ with the energy levels $E_0 = 0$ and $E_1 = \hbar\omega_0$.

For an arbitrary state $|\psi\rangle(t) = \tilde{c}_0(t)|0\rangle + \tilde{c}_1(t)|1\rangle$, equation (3.16) leads to its time evolution. At this point the reasoning from subsection 3.2 is followed by applying a unitary transformation on $|\psi\rangle$ and H that transforms them into a reference system rotating with angular frequency ω, followed by applying the RWA. Thus one obtains for the time evolution

$$i\hbar\frac{d}{dt}\begin{pmatrix}\tilde{c}_0\\ \tilde{c}_1\end{pmatrix} = -\hbar\begin{pmatrix}0 & \Omega_{\mathsf{R}}^{*}\\ \Omega_{\mathsf{R}} & \delta\end{pmatrix}\begin{pmatrix}\tilde{c}_0\\ \tilde{c}_1\end{pmatrix}. \tag{3.20}$$

This matrix equation provides a set of two linear differential equations for the two coefficients of the state $|\tilde{\psi}\rangle(t)$ with the second differential equation (DE) being coupled to the first one. This DE can be solved by insertion, resulting in

$$\ddot{\tilde{c}}_1(t) - i\delta\,\dot{\tilde{c}}_1(t) + |\Omega_{\mathsf{R}}|^2\,\tilde{c}_1(t) = 0. \tag{3.21}$$

It is immediately apparent that this is almost a DE of an undriven damped harmonic oscillator except of the imaginary damping constant. Assuming the initial condition $|\psi\rangle_{t=0} = |0\rangle$, the solution for the time evolution of $\tilde{c}_1(t)$ is given as

$$\tilde{c}_1(t) = \exp(i\phi)\,\frac{2|\Omega_{\mathsf{R}}|}{\Omega_{\mathsf{eff}}}\,\sin\left(\frac{\Omega_{\mathsf{eff}}}{2}\,t\right). \tag{3.22}$$

Here in the last equation ϕ is defined as arbitrary global phase and Ω_{eff} as effective Rabi frequency, which can be calculated by

$$\Omega_{\mathsf{eff}} = \sqrt{\delta^2 + 4|\Omega_{\mathsf{R}}|^2} \tag{3.23}$$

where in the case of excitation at energy resonance frequency ω_0 by the RF field, the Rabi frequency Ω_{R} and effective Rabi frequency Ω_{eff} become equal. The exact calculation is provided in

the appendix in subsection A.1.2. In the following the probability of finding the system in state $|1\rangle$ should be determined, which, due to our initial assumption that $|\psi\rangle = |0\rangle$ is valid at time $t = 0$, is equivalent to the statement that the system has made a transition from $|0\rangle$ to $|1\rangle$ after the time t. In general, the probability of finding the state $|\psi\rangle$ in the state $|1\rangle$ can be calculated via Born's probability interpretation as

$$P_{1\leftarrow 0}(t) = |\langle\psi(t)|1\rangle|^2 = \frac{4|\Omega_\mathrm{R}|^2}{\Omega_\mathrm{eff}^2} \sin^2\left(\frac{\Omega_\mathrm{eff}}{2}\, t\right) \tag{3.24}$$

which leads to a modulation of the probability amplitude shown in figure 4 for different detunings from the energy resonance frequency ω_0.

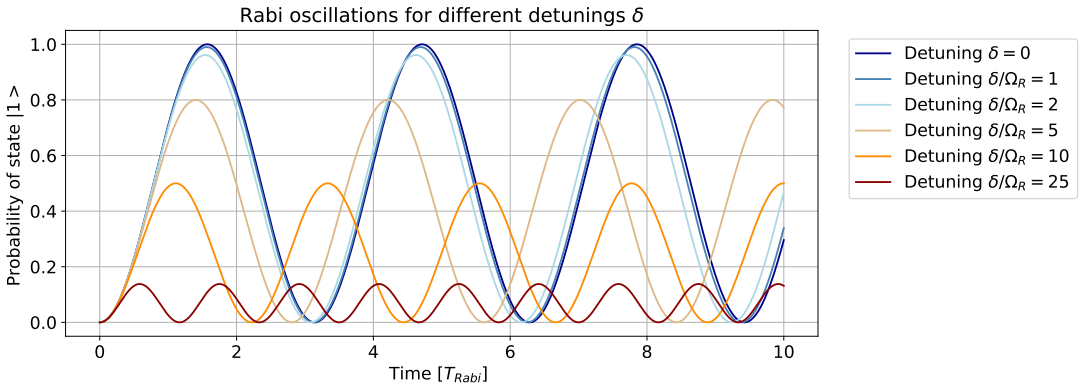

Figure 4: Probability of the $|1\rangle$ state being occupied depending on the time in units of the Rabi time, defined in equation (3.26). Here a two level system with eigenstates $|0\rangle$ and $|1\rangle$ and energy levels $E_0 = 0$ and $E_1 = \hbar\omega_0$ is considered. The Rabi oscillations are shown for different detunings $\delta = \omega - \omega_0$ from the energy resonance frequency ω_0.

In the case of non-vanishing detuning $\delta \neq 0$ the oscillation frequency of the Rabi oscillations increases while the amplitude decreases. The period duration is generally given by

$$T_\mathrm{Period} = \frac{2\pi}{\Omega_\mathrm{eff}} = \frac{2\pi}{\sqrt{\delta^2 + 4|\Omega_\mathrm{R}|^2}} \tag{3.25}$$

while the Rabi time, which is also the unit of the time axis in figure 4, is defined as

$$T_\mathrm{Rabi} = \frac{T_\mathrm{Period}}{\pi}\bigg|_{\delta=0} = \frac{1}{\Omega_\mathrm{R}}. \tag{3.26}$$

3.4 17-state Rabi oscillations

In the case of Dy bosons, the $J = 8$ manifold whose Zeeman effect is described in subsection 3.1 has to be considered. An excitation of the system with the resonance energy of two energetically neighbouring Zeeman sublevels therefore couples all 17 states due to their energetic equidistance. A population of all states is to be expected over time, which will be examined in more detail below. Similar to the two-state system, a general state $|\psi\rangle$ is assumed, which is transformed by means of an unitary transformation into a reference frame rotating with the frequency ω. This transformed state $|\tilde{\psi}\rangle$ can be substituted into equation (3.19) to obtain the time evolution as

$$i\hbar\frac{d}{dt}\begin{pmatrix}\tilde{c}_{-8}\\ \vdots \\ \tilde{c}_{8}\end{pmatrix} = -\hbar\begin{pmatrix}-8\delta & \Omega_{7,8} & 0 & \cdots & 0\\ \Omega_{7,8} & -7\delta & \Omega_{6,7} & \cdots & 0\\ 0 & \Omega_{6,7} & -6\delta & \cdots & 0\\ \vdots & \vdots & \vdots & \ddots & \vdots\\ 0 & 0 & 0 & \cdots & 8\delta\end{pmatrix}\begin{pmatrix}\tilde{c}_{-8}\\ \vdots \\ \tilde{c}_{8}\end{pmatrix}. \tag{3.27}$$

For neighbouring sublevels, individual Rabi frequencies are defined as[3]

$$\begin{aligned}\Omega_{m_J,m_J+1} &= \frac{\mu_B g_J B_{\mathrm{RF}}}{16\hbar}\sqrt{J(J+1)-m_J\,(m_J+1)}\\ \Omega_{m_J,m_J-1} &= \frac{\mu_B g_J B_{\mathrm{RF}}}{16\hbar}\sqrt{J(J+1)-m_J\,(m_J-1)}.\end{aligned} \tag{3.28}$$

In analogy to the two level system in subsection 3.3, Ω_{R} is defined as the Rabi frequency of the initial state $|-8\rangle$, respectively $\Omega_{\mathrm{R}} = \Omega_{-8,-7}$. In equation (3.27) the Rabi frequencies appear as secondary diagonal elements with a symmetry axis along the main diagonal elements. Furthermore a symmetry regarding inversion of the sign of the magnetic quantum number occurs. The Rabi frequencies from equation (3.27) have been calculated in figure 5 for field strengths up to $B_{\mathrm{RF}} = 5\,\mathrm{mG}$.

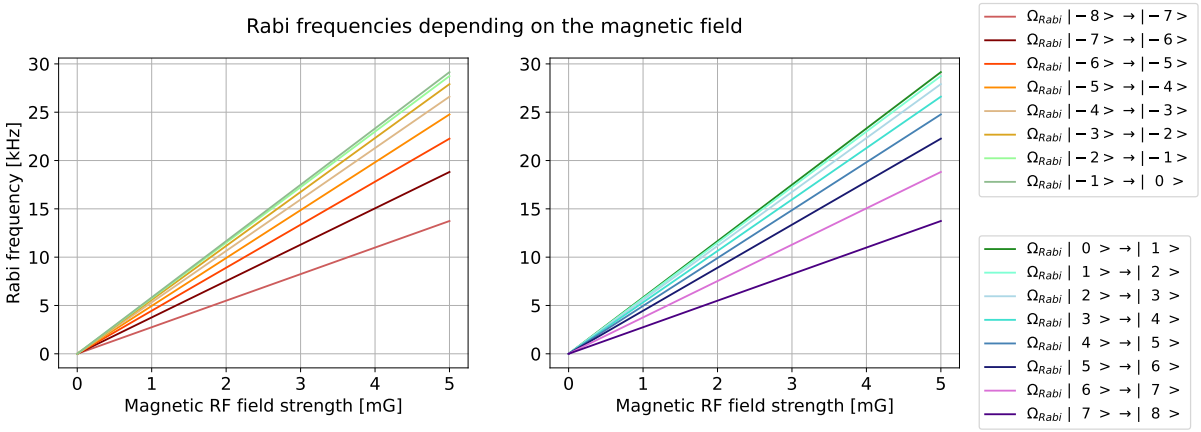

Figure 5: Rabi frequencies of all Zeeman sublevels as a function of magnetic RF field strengths up to $B_{\mathrm{RF}} = 5\,\mathrm{mG}$.

The Rabi frequencies in the selected magnetic field range are in the kHz regime and increase linear with the magnetic field strength. The slope increases for decreasing $|m_J|$ as expected in the definition in equation (3.28). For $|-8\rangle \rightarrow |-7\rangle$ the slope is given as $2748.16\,\mathrm{kHz/mG}$. In analogy to the two state system in equation (3.26), the Rabi time is defined as

$$T_{\mathrm{Rabi}} = \frac{1}{\Omega_{-8,-7}} = \frac{1}{\Omega_{\mathrm{R}}}. \tag{3.29}$$

The next step is to determine the time dependant occupation of the 17 states under RF coupling. Since the Dy atoms of the real experiment are initially in the $m_J = -8$ state, the initial state of the simulation is also set to be $|\psi\rangle_{t=0} = |-8\rangle$. There are various approaches for the time evolution with

[3] It is noted that this topic was addressed in [Nat17]. However the equations derived there differ from the ones obtained here.

two being presented in this thesis. For the first approach the eigenstates and eigenenergies of the Hamiltonian in equation (3.27) need to be calculated. The initial state $|-8\rangle$ can then be expressed in terms of the eigenvectors. Since for eigenvectors $|e\rangle$ with eigenenergy E the time evolution is known as complex rotation $|e\rangle(t) = \exp\left(i\,\frac{E}{\hbar}\,t\right)|e\rangle$, the time evolution for $|-8\rangle$ follows.

This method offers the opportunity to take another closer look at the eigenenergies. In figure 6, the system without RF coupling is shown, thus the eigenenergies of the ψ_{m_J} basis, which in this case also correspond to the eigenstates in the rotating reference frame after the unitary transformation U. This case can be achieved mathematically in equation (3.27), by setting all secondary diagonal elements to zero.

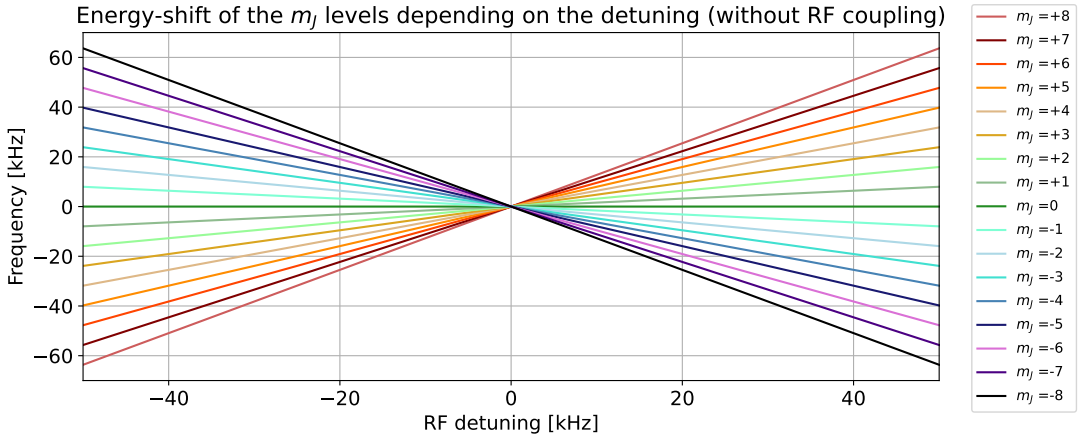

Figure 6: Energy shift of the 17 Zeeman sublevels in a rotating reference system without RF coupling depending on the detuning.

For a vanishing detuning δ the individual Zeeman sublevels degenerate in the rotating reference frame. The energy shifts change linearly with the detuning while the slope is proportional to the magnetic quantum number. In contrast, in figure 7 the new energy states of the Hamiltonian in equation (3.27) with RF coupling of the individual sublevels are shown.

The coupling is achieved by a magnetic field with strength $B_{\mathrm{RF}} = 2.4\,\mathrm{mG}$, since this value is in the same order of magnitude as the field of the RF coil built in section 3.4 will be. In comparison to figure 6, the degeneracy is lifted for $\delta = 0$ and a crossing of the energy levels is avoided. This region of avoided crossings represents the coupling region of the individual Zeeman sublevels, in which the $|m_J\rangle$ states there are no longer eigenstates, indicated by a color gradient in figure 7 [Nat17]. In the limiting case of high detunings, however, the coupling strength decreases and the original eigenstates $|m_J\rangle$ are being recovered.

Returning to the actual goal of determining the time evolution of the Zeeman sublevels under RF coupling, a second, equivalent method is now presented using a matrix exponential. For any system with time-independent Hamiltonian the time evolution operator $U(t, t_0)$ can be calculated and used to determine the time evolution of an arbitrary state:

$$|\psi\rangle_t = U(t, t_0)\,|\psi\rangle_{t_0} = \exp\left(-\frac{i}{\hbar}\,H\,(t - t_0)\right)\,|\psi\rangle_{t_0} \tag{3.30}$$

This procedure can only be used in the RWA approximation, since this eliminates the time dependence of the Hamiltonian in equation (3.12). The matrix exponential is generally defined by the exponential series with matrices as entry. This matrix exponential series reduces in the case of a diagonal matrix as Hamiltonian operator to a matrix with exponential entries on the main diagonal.

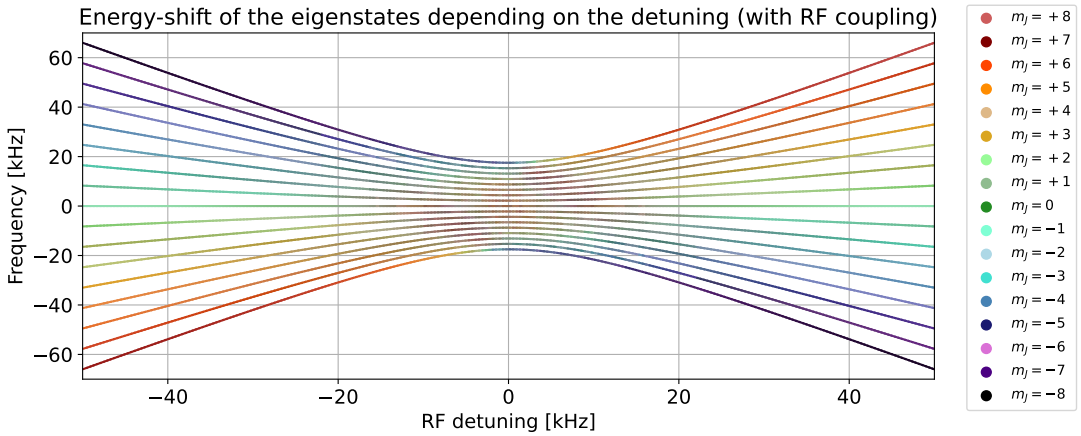

Figure 7: Energy shift of the 17 Zeeman sublevels in a rotating reference system with RF coupling depending on the detuning. The central region of the avoided crossings represents the coupling region where the eigenstates of the Hamiltonian are no longer described by the m_J quantum number. Note that the labels m_J in the legend do not describe the specific lines in the plot but rather are assigned to a specific colors. The lines are given by the individual eigenstates of the Hamiltonian. The colour gradient (which is especially present in the resonance region) is created by projecting each eigenstate onto the different $|m_J\rangle$ states and using these projection coefficients as a weighting for the corresponding colours. In the limiting case of high detunings the eigenstates approximate the $|m_J\rangle$ states.

However, since the $|m_J\rangle$ states are coupled by the orthogonal RF field, there are also side diagonal elements in the Hamiltonian operator, as can be seen in equation (3.27). Therefore, a closed-form expression for the time evolution can not be found and one has to calculate the time evolution numerically. Both methods are equally valid and result in the same time evolution. A Python script for the numerical calculation of the time evolution via eigenstates is provided in subsection A.3.1. The result of this numerical approach is shown in figure 8.

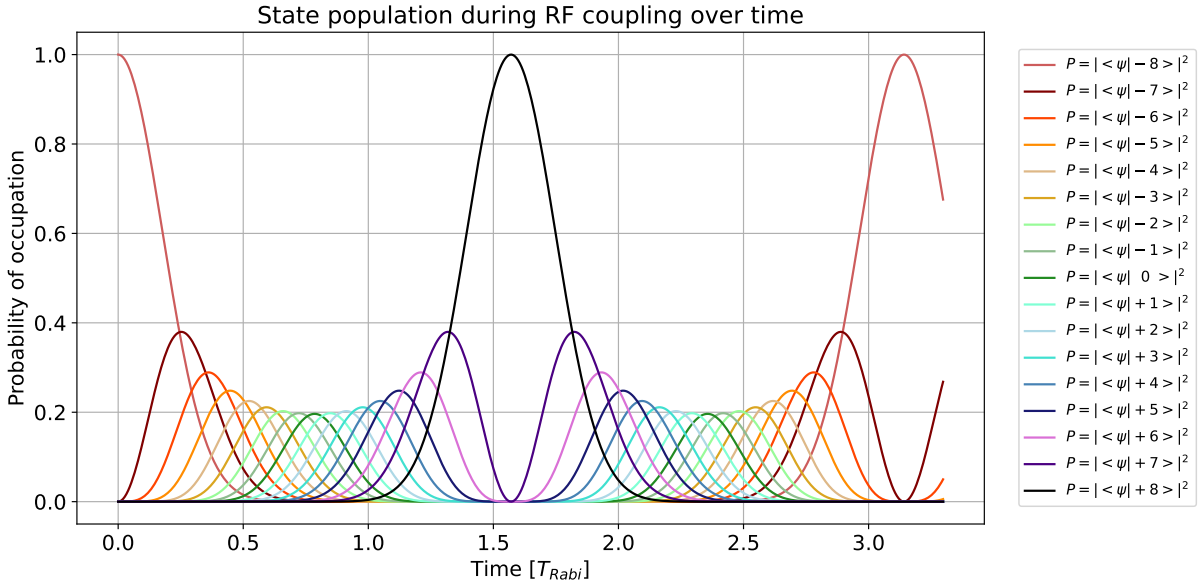

Figure 8: Population probability of the Zeeman sublevels as a function of the time under RF coupling at the resonance $\omega_0 = \omega$. The coupling is performed with a magnetic field strength of $B_{\text{RF}} = 2.4\,\text{mG}$. After a time $t = \pi T_{\text{Rabi}}$ the system has a revival in the ground state and the initial condition is restored. From this point on the state occupation probability evolves periodically.

The occupation of each state is time dependant, whereby after a time $t = \pi T_{\text{Rabi}}$ the initial state is restored, and the occupation of the states evolves periodically from this point onward. An interesting phenomenon is that after a time of $t = \frac{\pi}{2} T_{\text{Rabi}}$ the system is in the energetically highest state $|+8\rangle$ with a probability of 1. In theory, this allows the preparation of the pure spin state $m_J = +8$ for further experiments. To also characterise the influence of a non-vanishing detuning, these cases are displayed in figure 9. For reasons of clarity, only the ground states $m_J = -8$ (solid lines) and the energetically highest state $m_J = +8$ (dashed lines) are shown.

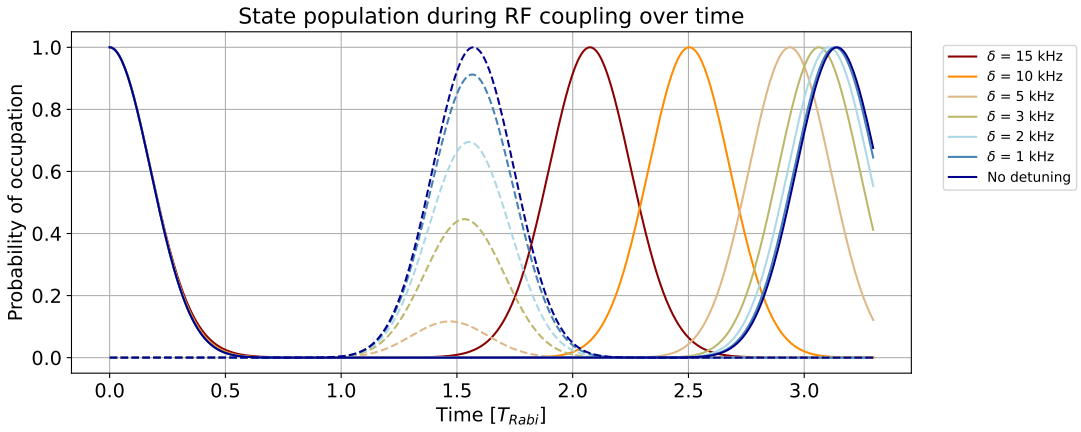

Figure 9: Plot of Rabi oscillations for different detunings $\delta \in \{0, 1, 2, 3, 5, 10, 15\}$ kHz. For reasons of clarity, only the ground states $m_J = -8$ (solid lines) and the energetically highest states $m_J = +8$ (dashed lines) are shown. The calculations were performed assuming a magnetic field strength of $B_{\text{RF}} = 2.4\,\text{mG}$.

For non-vanishing detunings $\delta \neq 0$ the revival time T_{Revival}, which is given by $T_{\text{Revival}} = \pi T_{\text{Rabi}}$ in the case $\delta = 0$, decreases as well as the probability of higher states to be populated. In order to find a functional relation between the detuning of the RF field and the revival time T_{Revival}, a Gaussian function $g(x)$, a Lorentz function $l(x)$ and an inverse root function $w(x)$ are defined as:

$$
\begin{aligned}
g(x) &= \frac{N}{\sqrt{2\pi\sigma^2}} \exp\left(-\frac{(x-\mu)^2}{2\sigma^2}\right) + A && \text{with } [N, \mu, \sigma, A] \text{ as fit parameter} \\
l(x) &= \frac{N}{\pi} \frac{\gamma}{(x-\omega_0)^2+\gamma^2} + A && \text{with } [N, \omega_0, \gamma, A] \text{ as fit parameter} \\
w(x) &= \frac{N}{\sqrt{(x-\mu)^2+\gamma}} + A && \text{with } [N, \mu, \gamma, A] \text{ as fit parameter}
\end{aligned}
\tag{3.31}
$$

The revival time as a function of detuning including the three fit functions is shown in figure 10. The optimal fit parameters including their errors are given in the right column. The 3σ interval around the fit functions are also shown in the plot in form of a slightly transparent coloring.

It is evident, that the inverse root fit describes the system in the best way, since the optical appearance is in agreement with the data and the 3σ interval of the errors is small compared to the Gaussian and Lorentzian fit. A closer look at the fit parameters reveals that for the inverse root fit $N \approx 2\pi$, $A \approx 0$ and $\gamma \approx 4\,|\Omega_{-8,-7}|^2 = 4\,|\Omega_{\text{R}}|^2$ hold, with $T_{\text{Rabi}} = 0.152\,\text{ms}$. With respect to equation (3.25), this indicates that the effective Rabi frequency and the formula for the period time depending on the detuning can be generalised from the two-state system - in which they have been defined - to the 17 state system of dysprosium and describe the revival time of the ground state $|-8\rangle$.

To conclude this theoretical section, one more case is presented, which is interesting from a theoretical perspective, but difficult to realise in the experiment. It concerns the time evolution in dysprosium

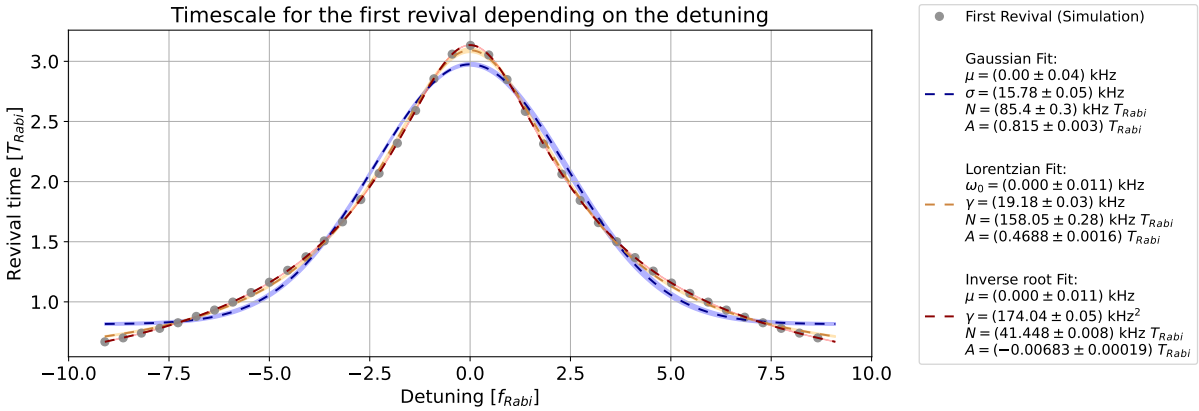

Figure 10: Revival time from numerical simulations depending on the detuning δ including a Gaussian, Lorentzian and inverse root fit. The fit functions are defined in equation (3.31) while their optimal fit parameter are displayed in the right box next to the plot together with their standard deviations. The 3σ interval of the fits is plotted in form of a slightly transparent coloring.

under RF coupling of the sublevels at the resonance frequency, only now with the initial state being given as $|\psi\rangle|_{t=0} = |0\rangle$. The time evolution is shown in figure 11, with some of the sublevels now shown by dashed lines, as this case is a symmetrically evolving system.

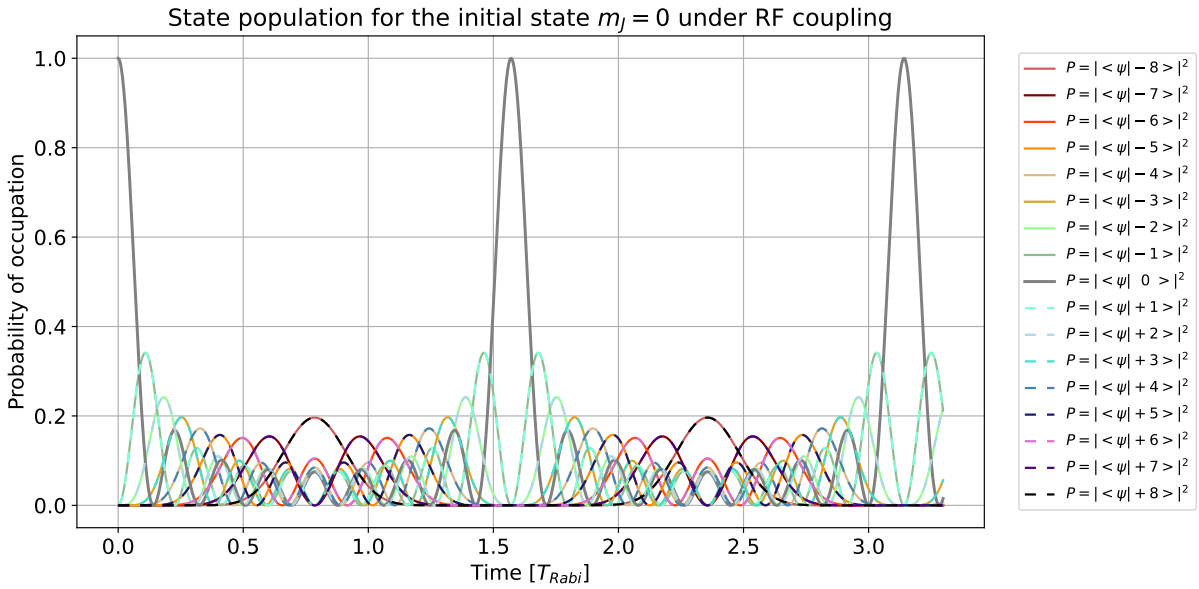

Figure 11: Time evolution of the initial state $|0\rangle$ for RF coupling with the energy resonance frequency. The occupation probability evolves symmetrically towards positive and negative m_J states. Furthermore, the revival time is halved compared to a time evolution of the ground state, that is shown in figure 8.

In addition to the symmetry, the shortened revival time stands out immediately. In figure 8, there was a complete occupation of the highest energy level after half a revival time as a counterpart to the ground state with the lowest energy. In figure 11, on the other hand, the ground state is passed through twice as often, but no further state is occupied with a probability of 1. This also has the direct consequence that no pure spin states different from the initial state can be generated by RF coupling for this initial condition.

Conclusion

In this section, the theoretical background of coupling Zeeman substates by means of radio frequency magnetic fields was discussed. A general equation of the Hamiltonian in the RWA was derived with equation (3.19) and applied to the two-state system as well as the dysprosium 17 state system. For the two state system, an analytical solution was obtained, while for dysprosium, two numerical solution methods were presented. In both cases, a periodic evolution of the occupation probabilities of the sublevels occurred.

These oscillations occur when the frequency of the RF magnetic field approaches the transition frequency between the substates. Thus, RF spectroscopy provides a way to calculate the energy difference between the Zeeman sublevels and, in consequence, the strength of the magnetic field at the position of the atoms, which is the goal of part A of this thesis.

Time evolution of Dysprosium

The adjacent QR code provides animations of the time evolution as a function of B-field strength, detuning and dipolar relaxation which will be dealt with in subsection 6.2.

For a better experience, viewing on a computer is recommended. To do this, simply click on the QR code or alternatively enter the following link into a browser: `https://www.maurice-rieger.de/time-evolution`

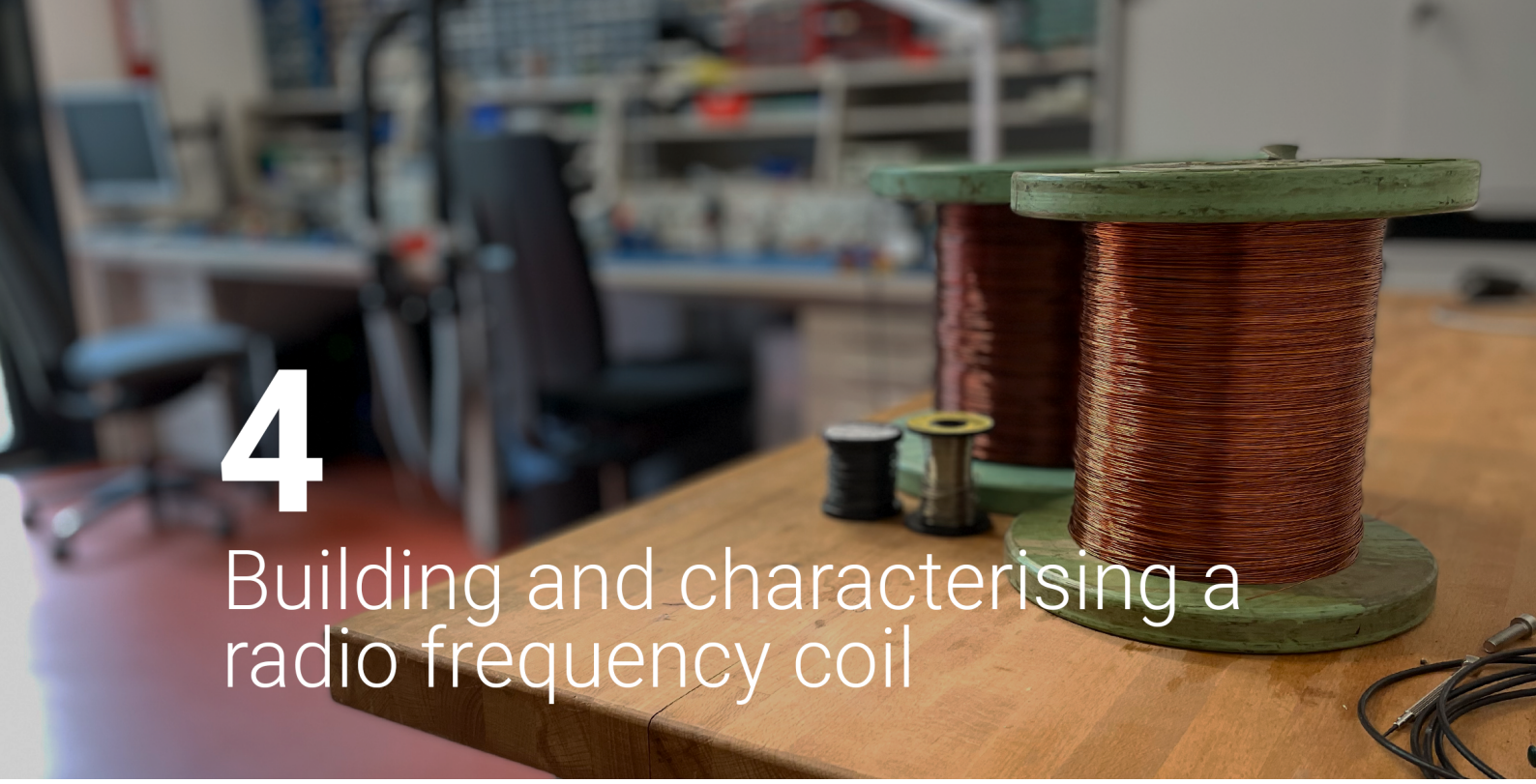

4 Building and characterising a radio frequency coil

Introduction

Now that the theory of coupling the dysprosium Zeeman substates has been dealt with, a coil for the necessary radio frequency field is to be built. The scope of this thesis is limited to circular coils, whose magnetic field along the coil axis is determined in subsection 4.1 for the DC case. In the experiment, the coil is operated with a fixed input power. In the high-frequency case, the frequency dependence of the resistance due to the skin effect must be taken into account when converting the power into a magnetic field strength, which is explained in subsection 4.2. Also it is not immediately true that the entire input power is actually used to generate a magnetic field in the case of high-frequency circuits. A parameter that describes the relation between incoming and reflected power is the S_{11} parameter, which is introduced in subsection 4.3. Subsection 4.4 and 4.5 are about the geometrical constraints in the experiment and an appropriate choice of coil geometry and coil mount design. The coil radius, the influence of different wire thicknesses and different coaxial supply cable lengths are investigated. The final configuration is summarised in a table at the end of subsection 4.5. In subsection 4.6 the driving circuit, including RF amplifier and switch, is considered. Finally, subsection 4.7 shows the theoretically achievable field strengths in the experimental chamber in the frequency range relevant for the application of the RF coil.

4.1 Magnetic field strength

Naturally when designing a RF coil one would aim for a highest possible magnetic field perpendicular to the z axis, which would allow a high flexibility for applications later in the experiment. This is especially true since the Rabi frequencies are directly proportional to the magnetic field as shown in subsection 3.4. One very simple approach would be to enlarge the winding number in the coil. However when dealing with high frequencies, the increase of the loss resistance is strongly non-linear due to the skin and proximity effect [MLB15] [Kar14]. This can potentially lead to the reduction of the current through the RF coil dominating the amplification of the magnetic field by an additional

winding, so the resulting magnetic field could be weakened compared to a single winding [HR76]. To avoid this, the focus here lies on single-turn RF coils.

One of the most important factors that influences the magnetic field strength is the coil geometry. However, when deciding on a coil design, practicality must always be maintained and implementation in the experiment must be easy. Therefore, more complex coil designs involving multiple coils or unnatural geometries are not addressed. In particular the losses in the increased number of soldering and contact points in a multi-coil system are difficult to quantify. The scope of this thesis is therefore limited to circular RF coils. For the DC case the magnetic field strength of a circular coil along its center axis can be determined by the Biot Savart law

$$\vec{B} = \frac{\mu_0}{4\pi} I \int \vec{dl} \times \frac{\vec{r} - \vec{r}\,'}{|\vec{r} - \vec{r}\,'|^3}. \tag{4.32}$$

Here, $\vec{dl}$ is an infinitesimal length element of the conductor at location $\vec{r}\,'$, through which a current I flows. The magnetic field is evaluated at location $\vec{r}$, which corresponds to the location of the atoms in the experiment. To simplify the calculation, $\vec{r}$ is assumed to be the zero vector and x is defined as the scalar distance between the location of the atoms and the conductor loop. In cylindrical coordinates, the infinitesimal conductor loop segment $\vec{dl}$ and the location of this segment on the conductor loop $\vec{r}\,'$ can be written as

$$\vec{dl} = \begin{pmatrix} -r\,\sin(\varphi) \\ r\,\cos(\varphi) \\ 0 \end{pmatrix} d\varphi \quad \text{and} \quad \vec{r}\,' = \begin{pmatrix} r\,\cos(\varphi) \\ r\,\sin(\varphi) \\ x \end{pmatrix}. \tag{4.33}$$

This allows to evaluate the integral in equation (4.32) and leads to an analytic formula of the magnetic field strength along the center axis of the RF coil with radius r_{RF}, which is given as

$$B_{\mathsf{RF}}(x) = \frac{\mu_0}{2} \frac{r_{\mathsf{RF}}^2}{\left(r_{\mathsf{RF}}^2 + x^2\right)^{\frac{3}{2}}} I. \tag{4.34}$$

Initially one would expect that for an angle $\theta \neq 90°$ between the quantisation axis and B_{RF} coil, the effective magnetic field strength can be obtained from equation (4.34) by multiplying with a factor $\cos(\theta)$, since only the horizontal field component couples the Zeeman substates. However, in reality the situation becomes more complex. First the coil is used in the radio frequency regime and therefore can emit electromagnetic waves. Second depending on the placement in the experiment the magnetic field can be distorted due to other conductive materials. Accordingly, even if the quantisation axis is placed parallel to the DC magnetic field, a perpendicular field component can still occur in RF operation.

4.2 Skin effect and resistance

In the experiment, the operation of the RF coil will be power-limited. To calculate a first estimate of the magnetic field strength with equation (4.34), the current I can be calculated from the power using

$$P = UI = RI^2 = \frac{U^2}{R}. \tag{4.35}$$

Therefore to obtain a value for the magic field strength, the resistance R of the RF coil is of decisive

importance in addition to the S_{11} parameter, which will be elaborated in subsection 4.3. Since RF coils are usually constructed with a low winding number and a large wire diameter, to maximise the possible input power, a precise measurement of the resistance is challenging in the sense that the electrodes of a multimeter have a resistivity in the same order as the RF coil. Furthermore, the resistance is generally frequency-dependent, as will be shown in the course of this subsection. Instead the AC resistance R for a power cable with a length l, a cross-sectional area A and a resistivity ρ of the wire material can be calculated as [Lam83]

$$R = \rho \, \frac{l}{\delta \, A} \tag{4.36}$$

with δ being the skin depth depending on the frequency. In the case of direct current or low-frequency alternating current, it is reasonable to assume $\delta \approx 1$. In the high-frequency range, however, the current increasingly flows only through the outer layers of the conductor, until in the limit of high frequencies, only the surface of the conductor is significantly current-carrying. This situation can be explained in electromagnetism theory by a reduced penetration depth of the electromagnetic fields associated with the wave propagation [Str16]. Effectively, a smaller cross-section is available to the current flow at high frequencies, so the resistance increases. The skin depth can be calculated as

$$\delta = \sqrt{\frac{2\rho}{\omega\mu}} = \sqrt{\frac{\rho}{\pi f \mu}} \tag{4.37}$$

where $\omega = 2\pi \, f$ is the angular frequency of the AC current and $\mu = \mu_0 \mu_r$ is the magnetic permeability of the wire. Finally, the temperature dependence of the resistivity ρ must be taken into account especially as the coil could heat up at high powers. For many materials, literature values of the resistivity under normal conditions $T = 20°\mathrm{C}$ are given. The change in resistivity can be approximated by a linear relation, where the slope is given by a material-specific temperature coefficient α. Overall, this results in

$$\rho(T) = \rho_{20°\mathrm{C}} \, (1 + \alpha \, (T - 293.15\,\mathrm{K})) \tag{4.38}$$

for a temperate T in Kelvin. These considerations lead to a final resistance formula

$$R(f, T) = \frac{l}{A} \sqrt{\pi f \mu \, \rho_{20°\mathrm{C}} \, (1 + \alpha \, (T - 293.15\,\mathrm{K}))} \tag{4.39}$$

with l, A, μ, α and $\rho_{20°\mathrm{C}}$ considered to be fixed system parameters and f, T considered to possibly change due to different input frequencies and coil heating.

4.3 Characterising high frequency electrical circuits

Operating an electric circuit in the high-frequency range can cause a frequency-dependent reflection of the input power P. In order to take this reflection into account for the RF coil constructed within the scope of this thesis, a measurement of the S_{11} reflection parameter is performed. A more general explanation of the relevance of this measurement method at high frequencies is given in the appendix in subsection A.2.1. The general measuring principle is based on travelling power waves where the incoming wave E_I and the reflected wave E_R can be defined as

$$E_\mathrm{I} = \frac{U + IZ}{2\sqrt{\mathrm{Re}(Z)}} \quad \text{and} \quad E_\mathrm{R} = \frac{U - IZ}{2\sqrt{\mathrm{Re}(Z)}} \tag{4.40}$$

where Z is the impedance of the circuit [Kur65] [CK14]. In the general case, impedance is a complex quantity consisting of resistance R and reactance Y and is defined as

$$Z = R + iY. \tag{4.41}$$

Thereby R contains the in-phase losses, whereas Y characterises the phase shift between alternating voltage and current. The S_{11} parameter is defined as

$$S_{11} = \frac{E_R}{E_I} = \frac{Z - Z_0}{Z + Z_0} \tag{4.42}$$

where Z_0 is the impedance of the measuring system. In high frequency applications it is common for electrical devices or components to have a reference impedance of $Z_0 = 50\,\Omega$. Usually the S_{11} Parameter is measured in decibel, which can be converted into a ratio of circuit relevant quantities. As energy like quantities E scale with the square of field quantities F, in the S_{11} parameter conversion a distinction has to be made:

$$\begin{aligned} \frac{F}{F} &= 10^{\left(\frac{S_{11}[\mathrm{dB}]}{20}\right)} \quad \text{as well as} \quad S_{11}[\mathrm{dB}] = 20 \cdot \log_{10}\left(\frac{F}{F}\right) \quad \text{for field-like quantities } F \\ \frac{E}{E} &= 10^{\left(\frac{S_{11}[\mathrm{dB}]}{10}\right)} \quad \text{as well as} \quad S_{11}[\mathrm{dB}] = 10 \cdot \log_{10}\left(\frac{E}{E}\right) \quad \text{for energy-like quantities } E \end{aligned} \tag{4.43}$$

In order to determine how much of the input power P is actually effectively converted into a magnetic field, the S_{11} parameter and the conversion for energy-like quantities can be used. This defines the effective power P_{eff} as

$$P_{\mathrm{eff}} = \left(1 - 10^{\left(\frac{S_{ji}[\mathrm{dB}]}{10}\right)}\right) P \tag{4.44}$$

from which the magnetic field strength will be deduced at a later stage. A generalisation of the concept of the S_{11} parameter to electrical networks is provided in the appendix in subsection A.2.1.

4.4 Geometrical constraints of the experiments and outer geometry of the RF coil

The RF coil should be placed as close as possible to the atoms to obtain maximal field strengths. The biggest restriction is the experimental chamber itself, which limits the minimum distance between the coil and the dysprosium atoms to $x = 10\,\mathrm{cm}$. In the experiment, the RF coil was attached to one of the diagonal viewports (see figure 1), as these are used for the 3D MOT beams whose optics have sufficient distance to the experimental chamber. The utility of the RF coil is to characterise the Helmholtz coil in z direction, shown in figure 2 and the two coils of the compensation cage. In this chosen configuration, the RF coil is aligned parallel to one of the compensation cage coils, but as explained in subsection 4.1, an nonzero orthogonal field component is still possible in the RF case.

For the DC case the magnetic field in equation (4.34) reveals a non-trivial dependence of the radius. In figure 12 the field strengths of a circular coil along the coil axis are shown for different radii.

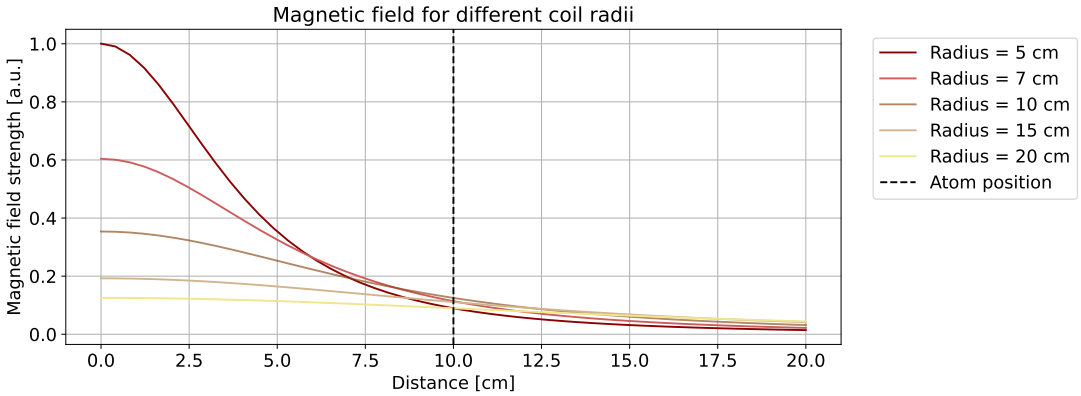

Figure 12: Relative magnetic field strength of circular coils with different radii along the coil axis. The region of the atoms is marked with a vertical dashed line.

The magnetic field differs strongly close to the coil position. Here small radii coils generate much stronger fields. However in the far field region this relation gets reversed and large radii coils generate stronger fields. In the region of the atoms, the field variations are less than 10% with a radius of $10\,\mathrm{cm}$ being optimal. Due to the small variations, the radius of the coil is chosen to fit around the viewports. The viewports have an outer diameter of $d_{\mathrm{VP}} = 69.342\,\mathrm{mm}$, however, some additional clearance is needed for easy attachment and removal of the RF coil. The coil diameter therefore is chosen to be $d_{\mathrm{RF}} = 75\,\mathrm{mm}$.

To maximise compatibility, a RF coil holder with plug connections for a detachable coil is designed. The electrical part of the mounting only consists of a Bayonet Neill Concelman (BNC) plug for the coaxial power cable and two RF coil plugs for the detachable RF coil. The mounting box has three elongated holes for attaching it to the optical table. With the elongation some adaptivity of placement in the experiment is maintained. A 3D model of the mounting as well as a first prototype are shown in figure 13

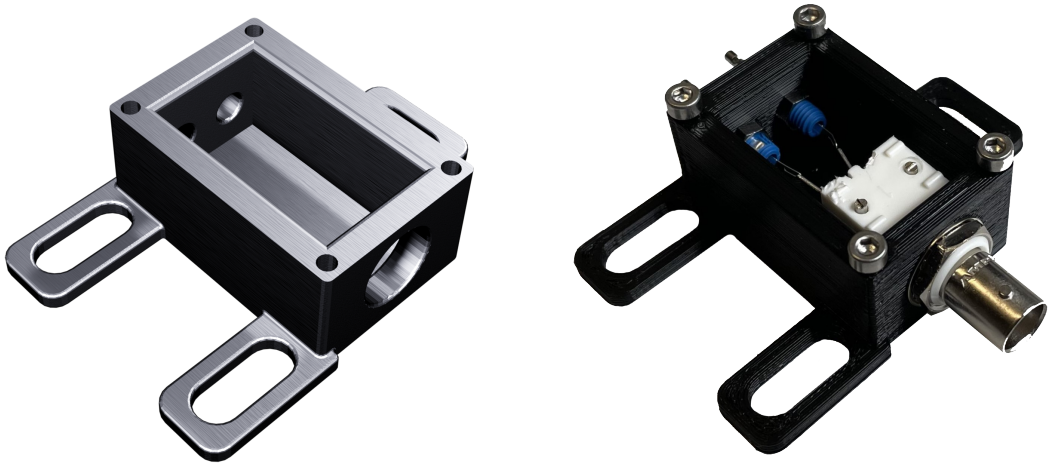

Figure 13: Design of an adaptive RF holder with detachable RF coil. The 3D model for the holder is shown on the left, while a 3D printed prototype made from polylactide filament (PLA) is shown on the right. The prototype consists of a BNC plug for the coaxial power cable and the two RF coil plugs for the detachable RF coil.

Since in the experiment high power lasers are used, several things have to be considered when choosing an appropriate material for the RF holder. First, the material has to be robust in the sense that there is no strong evaporation or melting process in the event that a laser beam reflection hits

the RF mount. Such evaporation could deposit on the very surface-sensitive optics and cause permanent damage. Second, the material should be non reflecting, to provide a higher safety when operating next to the running experiment, since the intensity of possible reflections is lower. Due to these restrictions anodised aluminium was chosen as material, since the aluminium entails the necessary robustness while the anodising process leads to an oxide layer on the surface that has a low reflection coefficient.

Aluminium is not as easy to process as polylactide filament using a 3D printer, so several final adjustments in the design have been made, to increase the manufacturability. These include removing the rounded edges, adding rounded edges in the central recess and aligning the long side to one length compared to figure 13. A technical drawing of final mount that has been manufactured from aluminium is provided in the appendix in subsection A.2.

4.5 Choice of the wire geometry

Once the coil geometry has been determined, the parameters of the wire used must be defined, including the material and diameter. Concerning the material, this thesis is limited to using copper for reasons of availability and good conductive properties. With regard to the thickness of the wire, in theory a high thickness is advantageous in order to be able to assure a maximum input power with a low coil temperature change. However, a possible influence of the wire thickness on the S_{11} parameter must be considered at the same time. In order to estimate this influence, test measurements were carried out in figure 14 for three different wire thicknesses. These measurements have been carried out for a coaxial cable length of $L_1 = 105\,\text{cm}$ and a length of $L_2 = 150\,\text{cm}$. The three different wire diameters are given as $d_{\text{W},1} = 1.45\,\text{mm}$, $d_{\text{W},2} = 1.2\,\text{mm}$ and $d_{\text{W},3} = 0.75\,\text{mm}$.

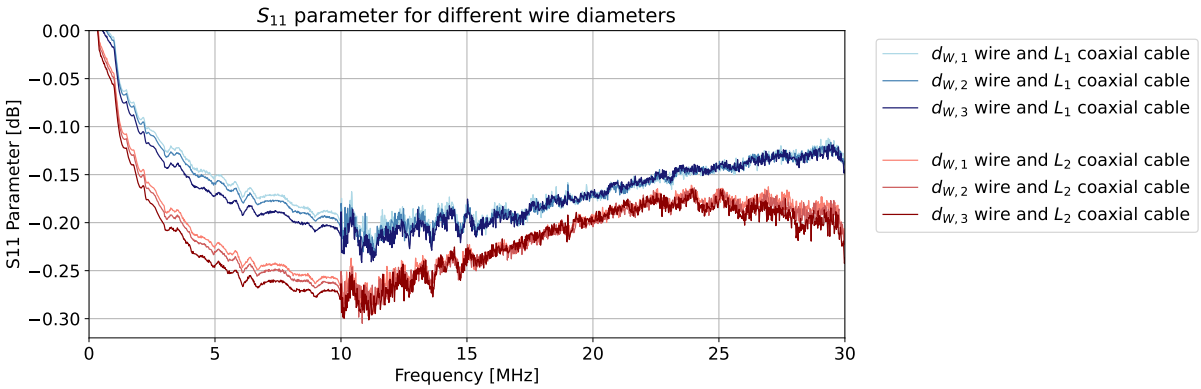

Figure 14: Test measurement to determine the influence of wire diameter and coaxial cable length on the S_{11} parameter value. The measurements have been taken for coaxial cable lengths of $L_1 = 105\,\text{cm}$ and $L_2 = 150\,\text{cm}$. The three different wire diameters are $d_{\text{W},1} = 1.45\,\text{mm}$, $d_{\text{W},2} = 1.2\,\text{mm}$ and $d_{\text{W},3} = 0.75\,\text{mm}$. The influence of the wire diameter on the S_{11} parameter is small compared to the influence of the coaxial cable length.

In general RF coils with thicker wires perform slightly worse because the reflected power is larger. However, it is also evident that the influence of the wire diameter is small compared to the influence of the length of the supply line. This is because the feed line, being a coaxial cable, itself has an impedance affecting the overall circuit impedance [Sca+21]. The theoretical background of impedance matching will be explained in subsection 7.1. In the experiment, a cable length of $L = 150\,\text{cm}$ was determined to be optimal, as this secures a comparatively high output power together with a certain flexibility of mounting the RF amplifier. The S_{11} parameter measurement does not take into account that in the case of a thicker coil wire a higher input power can also be selected, due to a reduced resistance and better thermal properties. Therefore a wire thickness of

$d_W = 1.45\,\text{mm}$ was chosen despite the slightly worse performance in the test measurements. This completes the development of an RF coil. The most important coil characteristics are summarised in table 2. The coil used in the experiment is shown in figure 15.

General information	Coil shape Material	circular copper
Coil parameters	Coil diameter Wire diameter	$d_{RF} = 75\,\text{mm}$ $d_W = 1.45\,\text{mm}$
Driving circuit	Coaxial cable length RF Amplifier Maximal output power	$L = 150\,\text{cm}$ LZY-22+ (Datasheet: [Min17b]) $P_{max} = 30\,\text{W}$

Table 2: Summary of the most important characteristics of the RF coil. This includes general information, the specific coil parameters and information about the driving circuit.

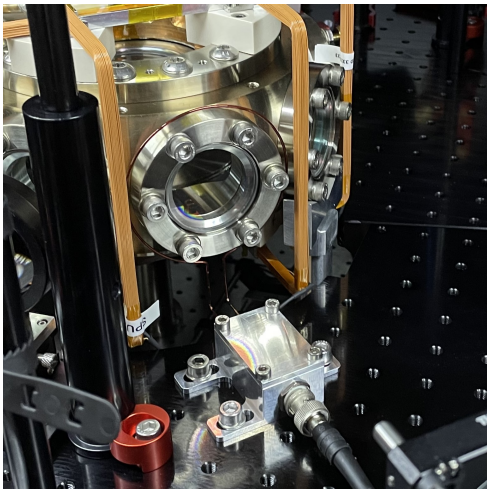

Figure 15: Final RF coil installed in the experiment and placed around one of the diagonal viewports of the experimental chamber. The final configurations of the RF coil are summarised in table 2.

4.6 RF driving circuit

When operating the RF coil in the experiment, a sufficient amount of power has to be supplied into the coil, due to possible losses in the coil itself or distortions of the magnetic field from surrounding metal objects. To achieve a high power input signal while maintaining a good signal quality a two step driving circuit is used. First a high quality but low power RF signal is generated by an arbitrary waveform generator. The output of the waveform generator then gets amplified by the RF amplifier LZY-22+. The amplifier has a maximal input power of $20\,\text{dBm}$, which corresponds to an output voltage of the signal generator of $6.324\,V_{pp}$ [Gur15]. The maximal output power of the LZY-22+ is 30 watts [Min17b], that are directly fed into the RF coil. Since the RF coil will not be driven constantly, a ZASWA-2-50DRA+ RF switch is installed between waveform generator and RF amplifier. This switch is driven by a transistor–transistor logic (TTL) square wave voltage [Min17a]. The ZASWA-2-50DRA+ is configured in such a way that in the event of no TTL voltage, no RF signal is forwarded. In order to avoid radiation losses or disturbing inductions in other metallic objects, all components were connected by coaxial cables. A schematic drawing of the circuit is provided in figure 16.

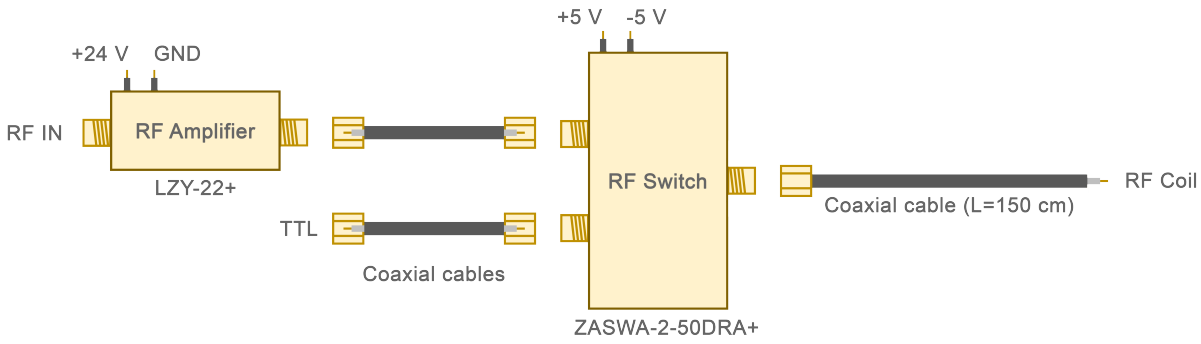

Figure 16: Illustration of the RF driving circuit consisting of a RF Amplifier and a RF Switch. A waveform generator acts as the RF IN. The TTL voltage activates the RF Switch.

Due to the high power gain in the LZY-22+ of $43\,\mathrm{dB}$ averaged over the operating frequency range, a significant amount of heat is generated. In the default configuration the LZY-22+ has an active cooling unit attached, containing a heatsink as thermal reservoir with a large surface area and a fan. The cooling power of this active cooling unit is sufficient, however, since the active cooling contains moving parts, it is better to mechanically isolate the amplifier from the experiment. The easiest solution is to place the LZY-22+ further away from the optical table. The only problem with that is the reduced flexibility in the cable length between RF amplifier and RF coil. It has been shown in subsection 4.5 that the cable length between the amplifier and the RF coil itself has an influence on the behaviour of the coil. Therefore, a mechanically isolated placement of the RF amplifier is not suitable for the application in the experiment. To keep a high flexibility in varying the cable length and still avoid mechanical influences of the cooling unit, the amplifier itself has been detached from the active cooling unit. Instead, it has been integrated in the water cooling system of the dysprosium laboratory. For this purpose, an adapter plate was designed, to mount the RF Amplifier to a water-cooled breadboard. The adapter plate is made of brass to secure good thermal conducting properties. The design is shown in the form of a technical drawing in the appendix in subsection A.2.

To further increase the heat flow from the RF Amplifier to the adapter plate, thermal paste has been applied onto the adapter plate, to prevent unevenness of the surfaces to influence the thermal flow. When choosing a thermal paste, it should be noted that those containing liquid metal have the best thermal conductivity properties. These pastes are usually made of Galinstan®, which is an alloy of gallium, indium, and tin that melts at a temperature of $T = -19^{\circ}\mathrm{C}$ [Han+22]. The only problem with using liquid metal thermal paste is that Galinstan® is corrosive to aluminium, which is the material of the RF holder housing. Therefore, an ordinary thermal paste must be used. These usually consist of metal powder or an oxide ceramic in a liquid carrier, mostly silicone oil or polyethylene glycol [Vis+00].

4.7 Expected magnetic field strength

Now the strength of the magnetic field for a maximum input power of $P_{\mathrm{max}} = 30\,\mathrm{W}$ at the RF coil is to be determined. It has been shown that not the entire input power is converted into a magnetic field, but rather only a proportion that is determined by the S_{11} parameter. This, however, is frequency-dependent, whereby a measurement is shown in figure 17. Before measuring the S_{11} parameter, an Open-Short-Match (OSM) calibration was performed on the network analyser. Open, Short and Match define distinctive points in the Smith chart that are (including the Smith chart itself) further elaborated in subsection 7.1 [TWK98]. The measurement was carried out directly in the experiment, so that possible inductive influences of the surrounding metal parts are taken into account in the measurement. A comparison with the previous measurements in a different environment in figure 14

shows that the environment exerts a noticeable, but not dominating influence on the coil.

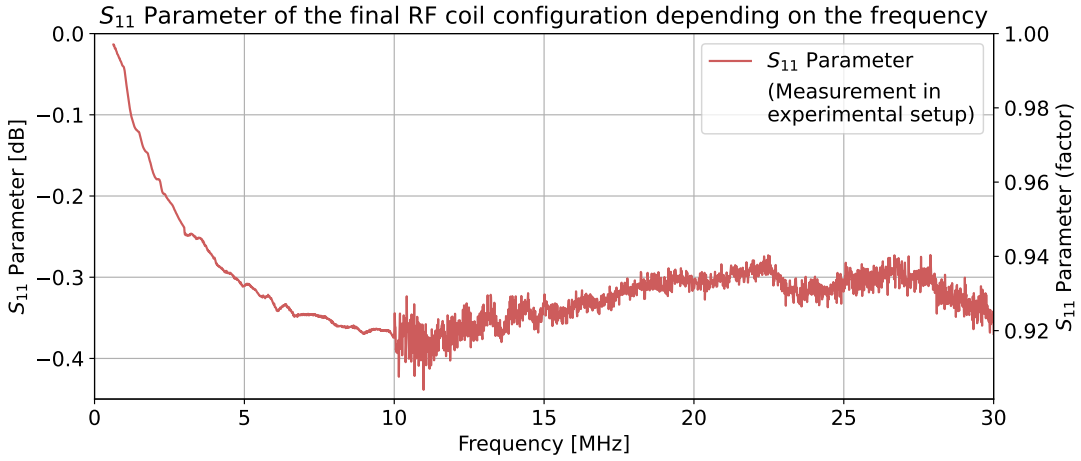

Figure 17: S_{11} Parameter measurement of the final coil assembly depending on the frequency. The measurement was carried out in the experimental setup, to ensure that possible inductive influences of the surrounding metal parts are taken into account. The S_{11} parameter is given in decibel and as a factor for the power with the conversion formula being displayed in equation (4.43). Exactly at a frequency of $f = 10\,\text{MHz}$ the noise suddenly increases. Since this phenomenon also occurred in other measurements it is assumed to have an internal cause in the network analyzer itself.

From the input power, the effective power P_{eff} can be determined with equation (4.44), which results in the effective coil current I_{eff} using equation (4.35). However, when converting the power into current, the frequency and temperature dependence of the resistance must also be taken into account. Test measurements have shown that the temperature of the coil does not change significantly in the time frames relevant for experimental operation, so this is assumed to be constant in the following with $T = 20°\text{C}$. From equation (4.39) as a formula for the resistance and equation (4.34) as formula for the RF field strength depending on the current, one can obtain

$$B_{\text{eff}}(x) = \left(\pi f \mu \rho_{20°\text{C}}\right)^{\frac{-1}{4}} \frac{\mu_0 \sqrt{P_{\text{max}} A}}{2\sqrt{l}} \frac{r_{\text{RF}}^2}{\left(r_{\text{RF}}^2 + x^2\right)^{\frac{3}{2}}} \sqrt{1 - 10^{\left(\frac{S_{ji}[\text{dB}]}{10}\right)}} \tag{4.45}$$

as the formula for the resulting strength of the magnetic field B_{eff} with $r_{\text{RF}} = \frac{d_{\text{RF}}}{2}$. The frequency-dependent effective magnetic field strength at the position of the atoms is shown in figure 18, together with a comparative value neglecting the skin effect in order to demonstrate the influence of the skin effect on the achieved field strengths.

For the field strength visualisation, in figure 18 a resistivity $\rho_{\text{Cu},20°\text{C}} = 17.2 \cdot 10^{-3}\,\Omega\,\text{mm}^3\,\text{m}^{-1}$ of copper at $20°\text{C}$ [Mat79] [Gia84] and a permeability of $\mu = 1.256629 \cdot 10^{-6}\,\text{H}\,\text{m}^{-1}$ [Cla08] have been considered. In the experiment, the frequency range from $f = 2\,\text{MHz}$ up to $f = 10\,\text{MHz}$ will be of particular relevance. In this range, field strengths are between $B_{\text{eff}} \approx 2.20\,\text{mG}$ and $B_{\text{eff}} \approx 2.45\,\text{mG}$. At this point, however, it still has to be taken into account that by placing the RF coil in the immediate vicinity of the steel chamber, the resulting magnetic field can be distorted due to Faraday induction in conductive materials, even if these effects have been considered for the S_{11} parameter measurement. Nevertheless the calculations above give a good indication, especially with regard to the frequency dependence of the magnetic field strength of the coil. To assess whether the magnetic field strengths are sufficient, the photon density can be compared with the atom density in the cloud. This estimation was made in the appendix in subsection A.2.3.

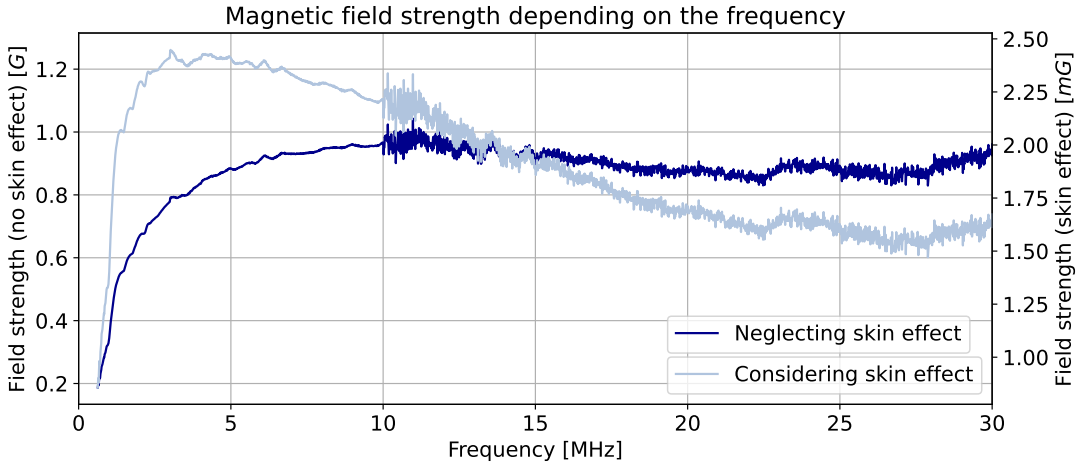

Figure 18: Magnetic field strength at the position of the atomic cloud calculated from the effective power fed into the RF coil. Besides the field strength considering the skin effect, which will be the important value for the experiment, a reference value neglecting the skin effect is given. This shows that the influence of the skin effect is significant and in the order of three magnitudes. For this simulation, a static temperature of the coil of $T = 20°\mathrm{C}$ has been assumed which results in the effective field strength formula displayed in equation (4.45).

Conclusion

This subsection has focused on the experimental setup built for radio frequency spectroscopy. At the beginning, a circular geometry of the coil was defined and its magnetic field in the DC case was derived. Subsequently, two concepts from radio frequency electronics, the skin effect and the S_{11} parameter were introduced. Based on these and the geometric constraints of the experiment, an optimal coil geometry was developed and a suitable mounting designed. After a brief consideration of the driving circuit, a formula for estimating the magnetic field was derived resulting in equation (4.45). In the experimentally relevant frequency range $f \in [2, 10]\,\mathrm{MHz}$, the magnetic field has a strength of $B_{\mathrm{eff}} \in [2.20, 2.45]\,\mathrm{mG}$. The fact that these field strengths are sufficiently strong was also shown in the appendix in subsection A.2.3 by comparing the photon density with the atom density inside the trap.

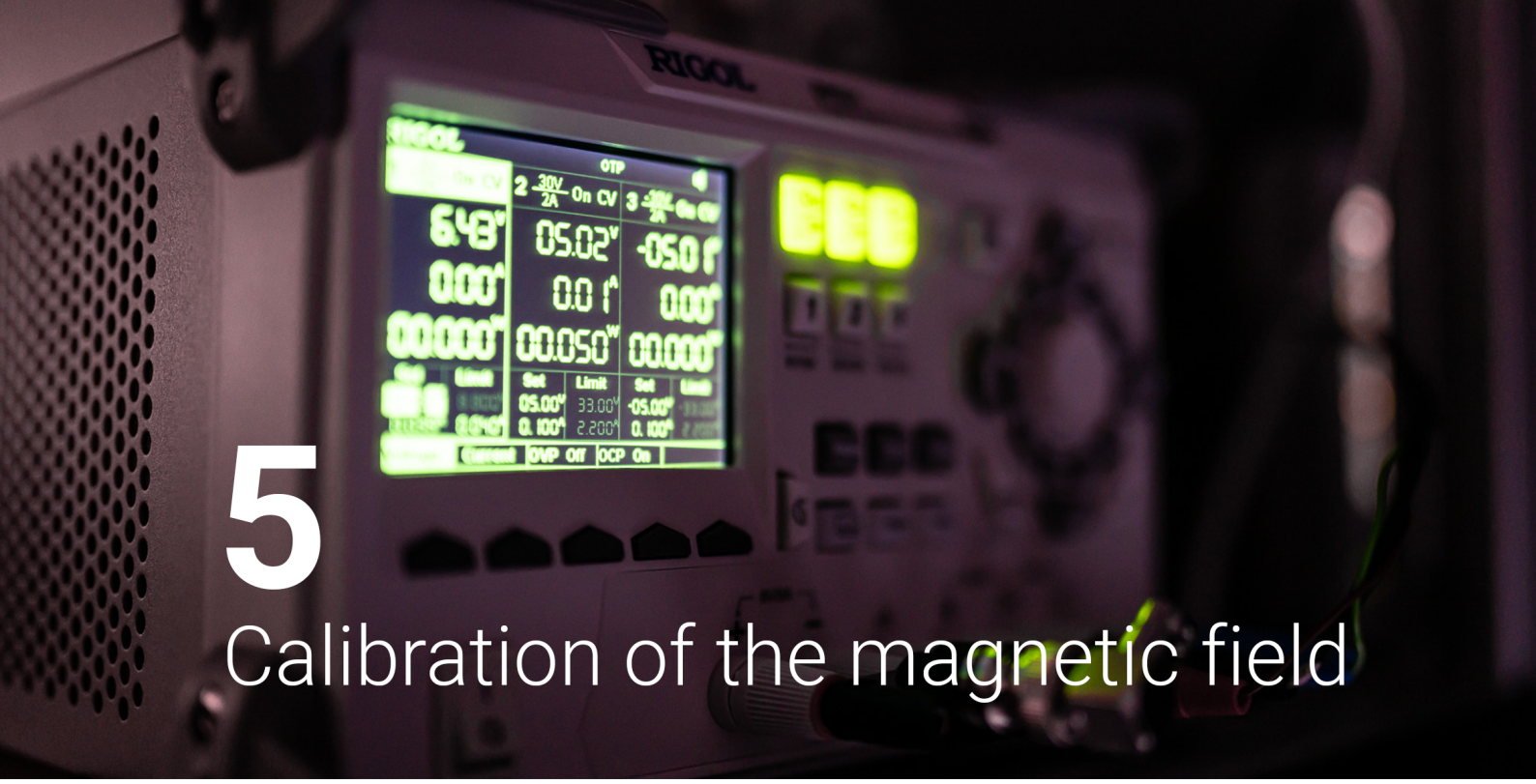

5 Calibration of the magnetic field

Introduction

This chapter deals with the calibration of the magnetic fields of the experimental chamber. In subsection 5.1 the general measurement principle and the configuration of the experiment are presented and explained by means of a test measurement. In subsection 5.2 the actual characterisation of the coils takes place, which in subsection 5.3 allows to perform transformations of the magnetic field.

5.1 Measurement method and atomic resonance

After the construction and characterisation of a RF spectroscopy setup, it will now find its first application, namely characterising the magnetic field of the experimental chamber coils. For an excitation close to the Zeeman splitting energy resonance, there will be an atom loss in the atomic cloud. Therefore, by measuring the atom loss depending on the RF frequency, the resonance can be localised and the energy splitting of the Zeeman sublevels can be determined. From equation (3.10) the strength of the magnetic field follows.

The magnetic field measurements will be taken on a thermal cloud rather than a BEC. The cooling phase to produce an almost pure BEC is divided in three different evaporative cooling phases. The evaporative cooling process is stopped at 50% completion of the second evaporative cooling phase. Since the resonance effects are expected to be very narrow in the given frequency range, instead of taking a lot of measurements at discrete frequency points, frequency sweeps for a given number of equidistant center frequencies are performed. It was taken care to ensure that the span of the frequency sweeps was slightly larger than the distance between two adjacent center frequencies, so overall a measurement over the entire frequency range was captured. Before each of the sweeps the atom trap was reloaded with atoms. After completion of the frequency sweep, the number of atoms was determined via an absorption image.

This overall procedure ensures that even with a very narrow absorption band, losses could be detected and localised in a certain frequency range. By starting from a large interval, the frequency span can be narrowed down to the range of the possible center resonance frequency location. An example measurement for a coil current of $I_z = 0.189\,\text{A}$ of the z coils of the experimental chamber is shown in figure 19.

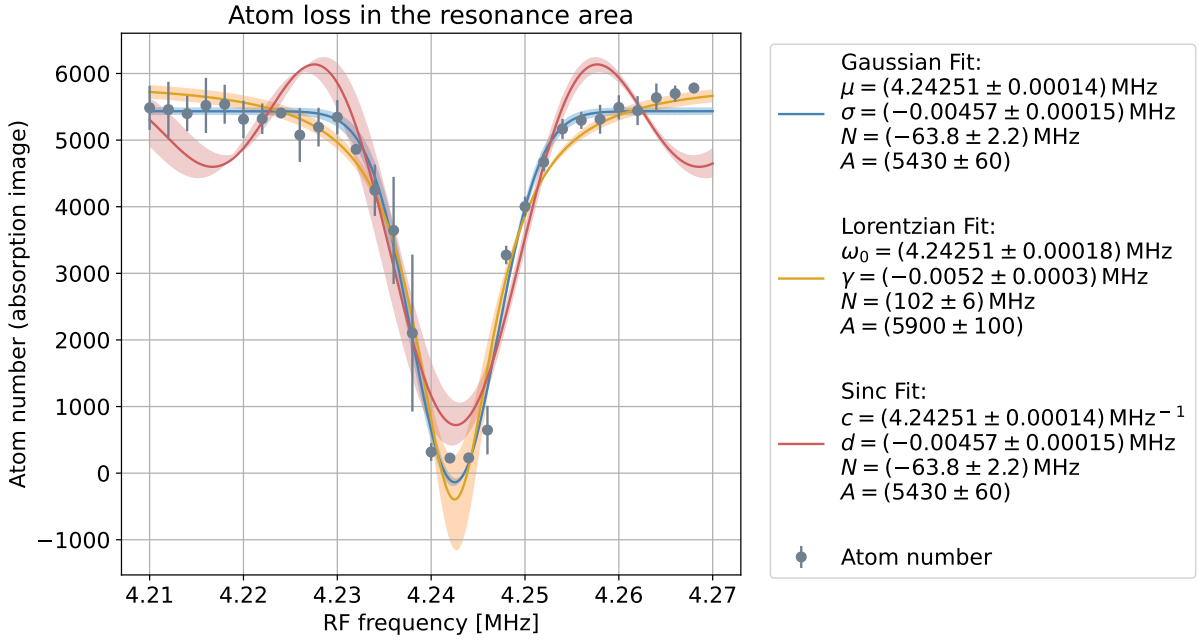

Figure 19: Example measurement of the atomic resonance recorded for a coil current $I_z = 0.189\,\text{A}$ of the z coils of the experimental chamber. After a broad frequency scan with center frequencies between $1.5\,\text{MHz}$ and $5.5\,\text{MHz}$ at a sweep range of $40\,\text{kHz}$, the resonance could be localised to the frequency range between $4.21\,\text{MHz}$ and $4.27\,\text{MHz}$. When this frequency range was measured again, the sweep range was reduced to $4\,\text{kHz}$. For both measurements, the length per sweep was $20\,\text{ms}$. The dip in atom number was localised to $f_{\text{cen}} = (4.24251 \pm 0.00014)\,\text{MHz}$ using three different fit functions defined in equation (3.31) and equation (5.46). The 1σ interval of the fits is displayed as transparent background in the same colour.

Three different functions, a Gaussian, a Lorentzian and a sinc function, were fitted to the measurement. While the former are both defined by equation (3.31), the sinc function $s(x)$ is defined as

$$s(x) = N\,\frac{\sin(c\pi\,(x-d))}{\pi\,(x-d)} + A \qquad \text{with } [N, c, d, A] \text{ as fit parameter.} \tag{5.46}$$

On a large timescale compared to the Rabi time and assuming only one body interaction, it can be expected that the Lorentzian describes the resonance best from atomic resonance theory, see e.g. [Pea81]. However, when other interaction processes occur, the situation can become more complicated. The analyzing code showed that for the determination of the resonance itself, the fit with a Gaussian is somewhat more reliable and faster. Since the center frequencies of the two fits agree within the error limits, this method is also considered a valid means. The Sinc function takes a special position here, since it would correspond to the atom depletion of an RF π pulse. In this example measurement, however, the pulse duration of $20\,\text{ms}$ is too high for a π pulse, so that no oscillations occur besides the main peak.

Using the result of the Gauss fit for the atomic resonance leads to a center frequency of $f_{\text{cen}} = (4.24251 \pm 0.00014)\,\text{MHz}$, from which the field strength of the B_z field can be determined for

a current of $I_z = 0.189\,\text{A}$. With $E = hf$ and equation (3.10) one obtains a field strength of $B_{z,\text{exp}} = (2.42494 \pm 0.00008)\,\text{G}$. This experimental result can now be compared with the theoretical expectation. Using the Biot Savart law in equation (4.32) and taking into account that the two coils in the z direction are in a Helmholtz configuration, one can determine the magnetic field strength using the geometry of the experimental chamber and its coils. One obtains [Sch22]

$$B_{z,\text{theo}} = 10.75\,\text{G}\,\text{A}^{-1} \tag{5.47}$$

as equation for the field strength depending on the coil current at the atom position. This leads to a magnetic field strength of $B_{z,\text{theo}} = 2.03\,\text{G}$ for the current that was used to obtain the measurements in figure 19. The experimentally measured field strength differs significantly from the theoretical expectation. However this is reasonable, due to the fact, that the theoretical value only is true for an ideal system without any disturbing influences. Especially metallic parts like the chamber itself can influence the shape and strength of the magnetic field.

5.2 Characterisation of the experimental chamber coils

After explaining the measurement procedure of the magnetic field strength for an example measurement in subsection 5.1, the magnetic field coils of the experimental chamber are now to be characterised. These are the Helmholtz coil in the z direction and the two compensation cage coils in the x-y plane, which have been shown in subsection 2.4. To characterise the coils, a magnetic field measurement is carried out for a series of known current values for each coil separately. The current field curve is expected to follow a linear relation, except for the region near $I_{x,y,z} = 0\ A$, since there is expected to be an offset in an arbitrary direction. This behaviour can be described by

$$|\vec{B}_{x,y,z}| = \sqrt{(B_0^2 - \beta_{x,y,z}^2) + (\alpha_{x,y,z} I_{x,y,z} + \beta_{x,y,z})^2}. \tag{5.48}$$

With B_0 as the total, external offset field strength, $\beta_{x,y,z}$ as internal offset due to an offset current of the coil power source and $\alpha_{x,y,z}$ as linear slope of the current-field relation. The curves for all spatial directions are displayed in figure 20.

The fit parameters of equation (5.48) are the external offset B_0, the internal offset $\beta_{x,y,z}$ and the linear slope $\alpha_{x,y,z}$. These are summarised in table 3 for all three coils in the x, y and z directions.

Spatial direction	Linear slope $\alpha_{x,y,z}$	Internal offset $\beta_{x,y,z}$	External offset B_0
x coil	$(9.52 \pm 0.05)\,\text{G}\,\text{A}^{-1}$	$-(0.164 \pm 0.017)\,\text{G}$	$(0.435 \pm 0.016)\,\text{G}$
y coil	$(10.30 \pm 0.05)\,\text{G}\,\text{A}^{-1}$	$(0.202 \pm 0.015)\,\text{G}$	$(0.440 \pm 0.009)\,\text{G}$
z coil	$(10.6021 \pm 0.0022)\,\text{G}\,\text{A}^{-1}$	$(0.3254 \pm 0.0008)\,\text{G}$	$(0.4333 \pm 0.0007)\,\text{G}$

Table 3: Linear slope $\alpha_{x,y,z}$, internal offset $\beta_{x,y,z}$ and external offset B_0 as fit parameter of equation (5.48) for all magnetic field coils oriented in the three spatial directions.

With this measurement, the magnetic field coils can be configured to compensate the offset field influences. Having achieved this, the current field relation becomes perfectly linear which simplifies the experimental control.

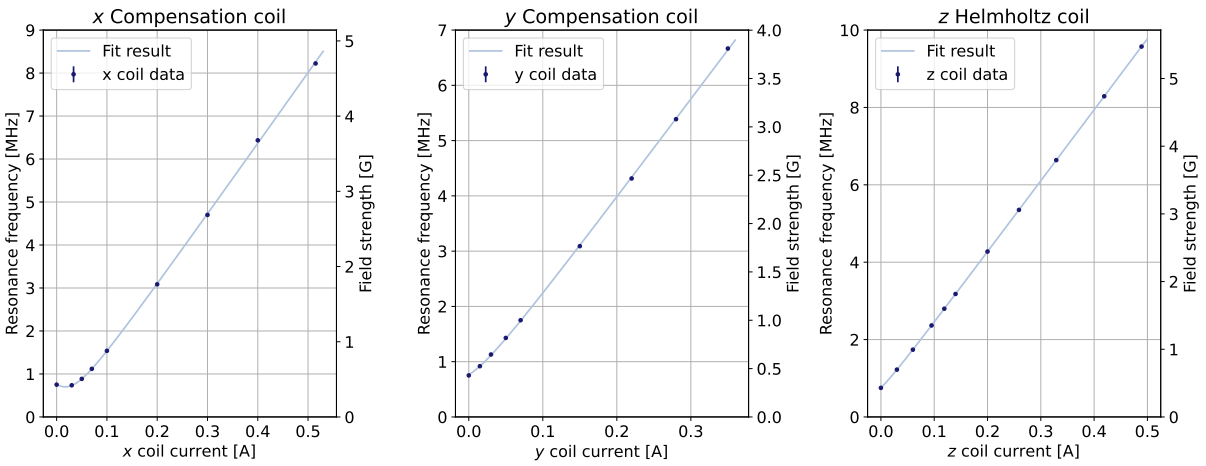

Figure 20: Characterisation of the compensation cage coils in x and y direction as well as the Helmholtz coils in z direction. The coil configuration has been further explained in subsection 2.4. The fit function of the measurements is shown in equation (5.48) and takes into account an external offset field due to environmental influences as well as an internal offset field due to the imperfection of the coil power source that could result in an offset current, even when the current is set to be zero.

5.3 B-field transformations

After the calibration of the magnetic field and compensation of the external offset field, the current field relation is now perfectly linear. This simplifies the control of the experiment, especially for transformations of the magnetic field, which will be dealt with in this subsection. Therefore it is now assumed

$$B_{x,y,z} = \alpha_{x,y,z}\, I_{x,y,z} + \beta_{x,y,z} \qquad \text{and} \qquad I_{x,y,z} = \frac{B_{x,y,z}}{\alpha_{x,y,z}} - \frac{\beta_{x,y,z}}{\alpha_{x,y,z}}. \tag{5.49}$$

Three different transformations are presented in this thesis. The first is a free spatial rotation of the field vector. Two angles θ and ϕ are used to describe this rotation. θ describes the angle between the z axis and the field vector and ϕ the angle between the y axis and the projection of the field vector in the x-y plane. Starting from a position $(\theta_\mathrm{i}, \phi_\mathrm{i})$ the field vector shall move linearly interpolated to a target point $(\theta_\mathrm{f}, \phi_\mathrm{f})$. This transformation should be performed in the time Δt and include a linear scaling of the magnetic field strength from $|\vec{B}| = B_1$ to $|\vec{B}| = B_2$. This framework leads to the equations shown below:

$$\begin{aligned}
B_x(t) &= \left(B_1 + (B_2 - B_1)\,\frac{t}{\Delta t}\right) \sin\left(\phi_1 + (\phi_2 - \phi_1)\,\frac{t}{\Delta t}\right) \sin\left(\theta_1 + (\theta_2 - \theta_1)\,\frac{t}{\Delta t}\right) \\
B_y(t) &= \left(B_1 + (B_2 - B_1)\,\frac{t}{\Delta t}\right) \cos\left(\phi_1 + (\phi_2 - \phi_1)\,\frac{t}{\Delta t}\right) \sin\left(\theta_1 + (\theta_2 - \theta_1)\,\frac{t}{\Delta t}\right) \\
B_z(t) &= \left(B_1 + (B_2 - B_1)\,\frac{t}{\Delta t}\right) \cos\left(\theta_1 + (\theta_2 - \theta_1)\,\frac{t}{\Delta t}\right)
\end{aligned} \tag{5.50}$$

The second transformation should perform multiple rotations of the magnetic field around a spatially fixed axis. To describe the orientation of the rotation axis, the parameters (θ, ϕ) are defined. θ is defined like in the first transformation while ϕ in now the angle between the projection of the rotation axis in the x-y plane and the x axis. Between this rotation axis itself and the rotating field vector an additional angle ξ is defined, while the rotation speed is given as the angular frequency ω. The magnetic field strength B_0 should stay fixed during the rotation. This leads to:

$$
\begin{aligned}
B_x(t) &= B_0\left(\cos(\xi)\,\sin(\theta)\,\cos(\phi) + \sin(\omega t)\,\cos(\theta)\,\cos(\phi)\,\sin(\xi) - \cos(\omega t)\,\sin(\phi)\,\sin(\xi)\right) \\
B_y(t) &= B_0\left(\cos(\xi)\,\sin(\theta)\,\sin(\phi) + \sin(\omega t)\,\cos(\theta)\,\sin(\phi)\,\sin(\xi) + \cos(\omega t)\,\cos(\phi)\,\sin(\xi)\right) \\
B_z(t) &= B_0\left(\cos(\xi)\,\cos(\theta) - \sin(\omega t)\,\sin(\theta)\,\sin(\xi)\right)
\end{aligned}
\tag{5.51}
$$

Finally in the last transformation, the field vector $\vec{B}$ should be spatially fixed with an oscillating field strength containing an offset field B_{off} and an amplitude B_{amp}. The oscillation is characterised by the angular frequency ω, while the orientation is given by the same parameters θ and ϕ as defined in the second rotation. This leads to:

$$
\begin{aligned}
B_x(t) &= \left(B_{\text{off}} + B_{\text{amp}}\,\sin\left(\omega t\right)\right)\,\sin(\theta)\,\cos(\phi) \\
B_y(t) &= \left(B_{\text{off}} + B_{\text{amp}}\,\sin\left(\omega t\right)\right)\,\sin(\theta)\,\sin(\phi) \\
B_z(t) &= \left(B_{\text{off}} + B_{\text{amp}}\,\sin\left(\omega t\right)\right)\,\cos(\theta)
\end{aligned}
\tag{5.52}
$$

By using the equation (5.49), one can directly obtain the corresponding currents for the different coils for all three field transformations. In the experiment, these transformations are implemented via the package Labscript [Sta+13]. An example code for such an implementation in Python can be found in the appendix in subsection A.3.2. In addition to the implementation, a visualisation code is also provided, which outputs a .gif animation of the 3D field vector and a plot of the currents in the individual coils.

Conclusion

After the theoretical foundations were laid and an RF spectroscopy setup was built, the measurements could finally be carried out in this subsection. For the determination of the resonance frequency, a Gaussian fit was used, since this had a faster computation time and the localisation of the resonance by the Gaussian and Lorentz fit corresponded within the error limits. Despite the fact that the RF coil was placed parallel to one of the compensation cage coils, this did not prove to be a problem and the external and internal offset of all three coils could be determined with the help of a fit (see table 3). Reasons why the measurement works despite the suboptimal placement can be the emission of electromagnetic waves and the disturbance of the magnetic field by induction in the metallic environment of the RF coil, as discussed in section 4. It has also been found that the photon density is several orders of magnitude higher than the atom density, so that a reliable measurement is still possible for a weaker magnetic field component orthogonal to the quantisation axis. By characterising the coils, the magnetic offset could be compensated and in the next step different magnetic field transformations could be implemented.

Magnetic field transformations

The adjacent QR code provides animations of the discussed B-Field transformations. This includes the B-Field vector in a 3D plot as well as the corresponding current of the coils in a 2D Plot.

For a better experience, viewing on a computer is recommended. To do this, simply click on the QR code or alternatively enter the following link into a browser: `https://www.maurice-rieger.de/field-transformations`

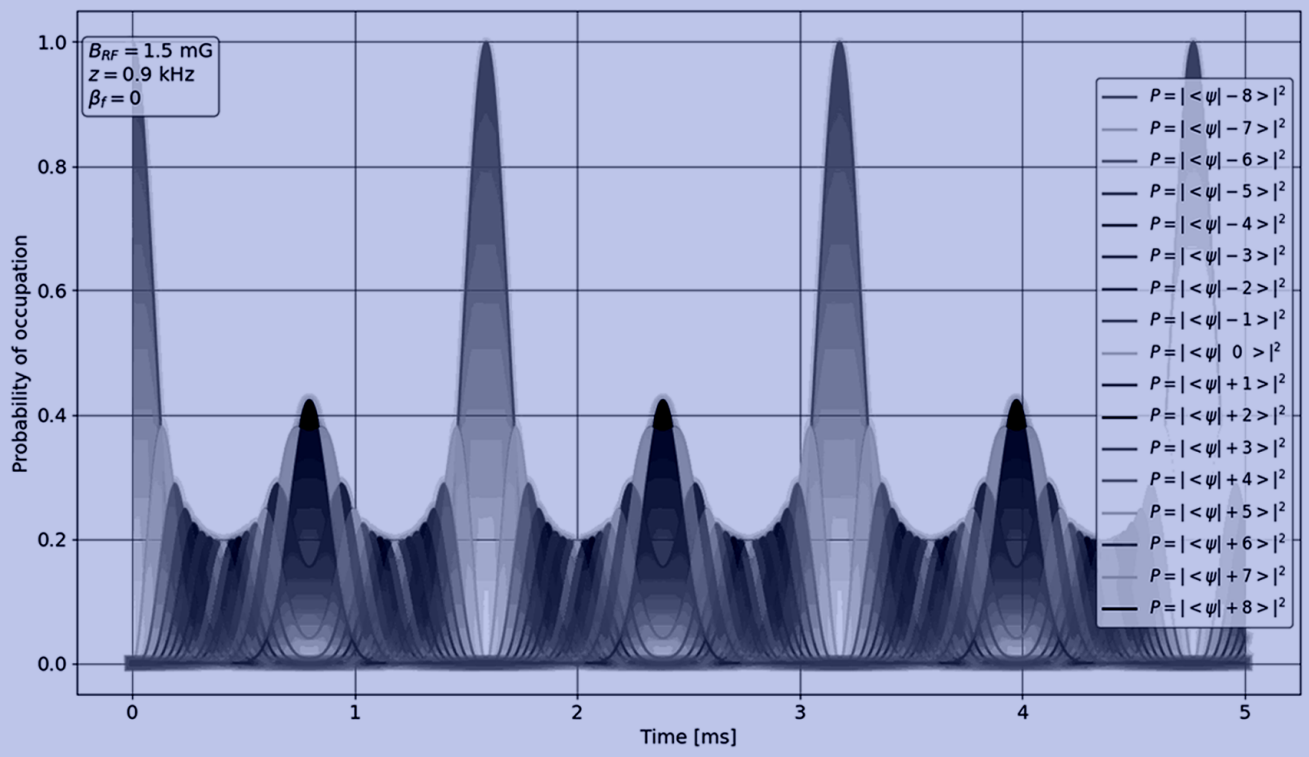

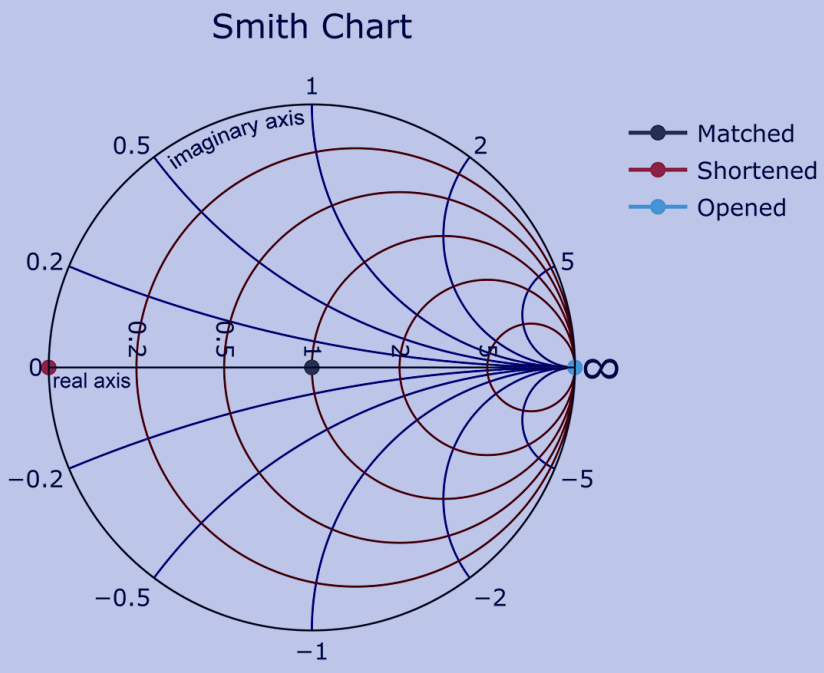

B

Spin preparation in dysprosium using Rabi oscillations

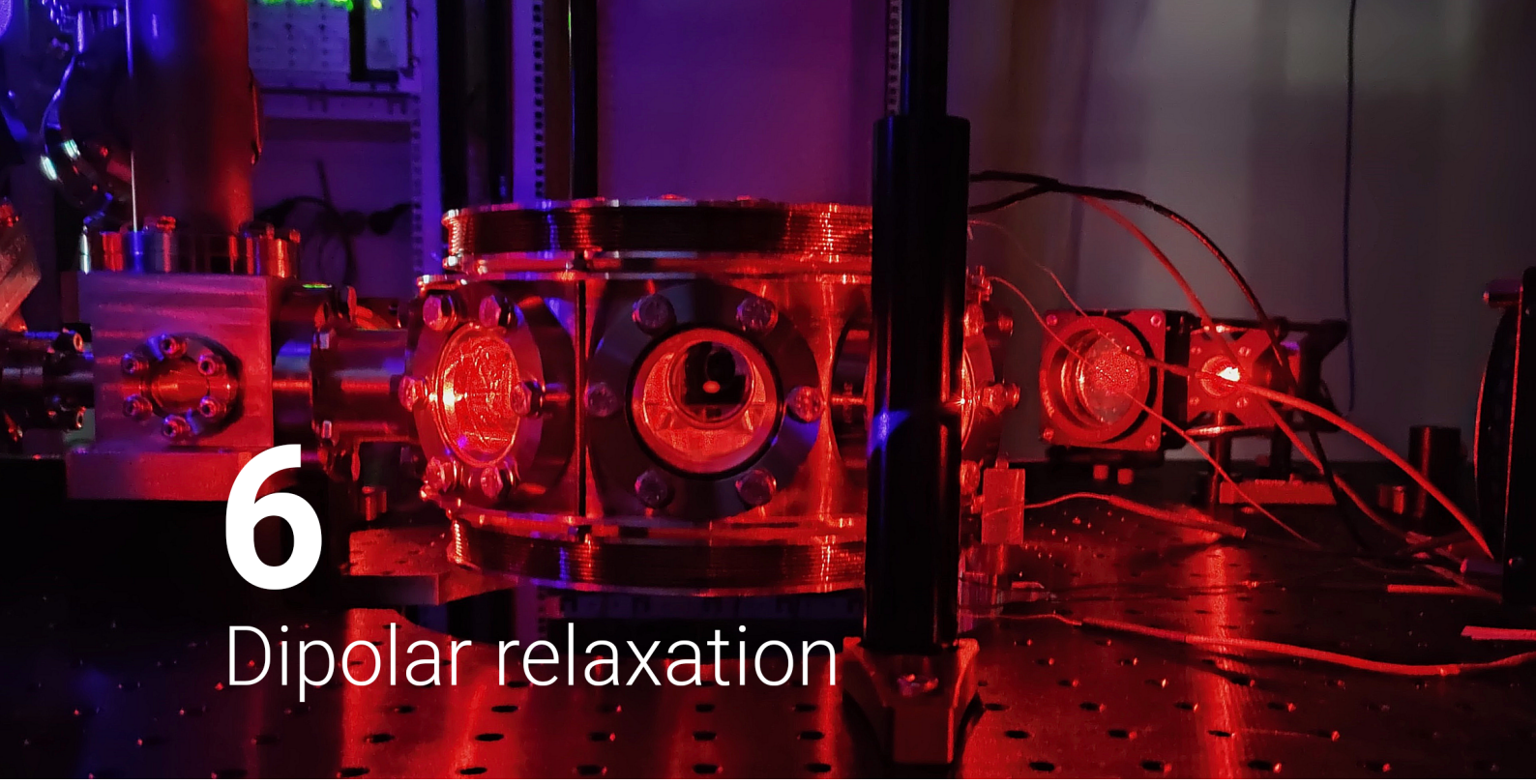

6 Dipolar relaxation

Introduction

In subsection 3.4, simulations of the occupation probabilities of the Zeeman sublevels revealed a periodic behaviour when the dysprosium atoms are excited with radio frequency magnetic fields. This periodic evolution should also be measurable in experiments and could be used to prepare the atoms in a pure $|+8\rangle$ state. In reality, as shown in subsection 6.1, these oscillations have not been detected. The cause is assumed to be dipolar relaxation, which is a two-body loss process. In order to check the plausibility of this assumption, the time scales of dipolar relaxation and Rabi oscillations are to be compared with each other. In the subsections 6.2 and 6.3 two coupled differential equations of dipolar relaxation for atom number and temperature are derived. In subsection 6.4 an analytical solution is presented and the evolution of the occupation probabilities under the presence of dipolar relaxation is simulated in subsection 6.5.

6.1 Experimental challenges of measuring oscillations

Up to this point, the RF coil and the possibility of using it to couple the Zeeman sublevels was used to characterise the magnetic field coils. This took advantage of the fact that an atom loss occurs when the states are coupled. In subsection 3.4, simulations have shown that RF coupling can also drive oscillations in the occupation probability of the states. Since absorption imaging has a different sensitivity for different Zeeman sublevels, these oscillations should also be reflected in measurements and on a time scale similar to the Rabi time. This would allow to determine the Rabi frequency experimentally and thus obtain a comparative value to the theoretical simulations in subsection 3.4.

To prove this assumption, a fixed current of $I_z = 0.189\,\mathrm{A}$ was fed into the B_z coils of the experimental chamber. The RF frequency was fixed to the center of the atomic resonance $f_{\mathrm{cen}} = (4.24251 \pm 0.00014)\,\mathrm{MHz}$ while the pulse length was varied. In these test measurements, however, only atom depletion could be detected, which instead of showing oscillations decreased very

quickly and then flattened out. Therefore, it can be assumed that the loss mechanism responsible for the atom depletion is sufficiently strong to suppress the Rabi oscillations, respectively that the time scale on which the loss takes place is smaller than the time scale of the Rabi oscillations. The primary loss process is assumed to be dipolar relaxation, which is a two-body interaction that becomes active as soon as other states than the ground state get occupied. Dipolar relaxation follows as a consequence from the dipolar interactions in dysprosium. In subsection 2.3 an approximation of these interactions has been presented, however the full interaction involves spin operators and contains spin exchange terms as well as dipolar relaxation terms. For further reading it is referred to chapter I and III of [Cho+22]. To confirm the suspicion that dipolar relaxation causes the absence of a measurable revival, the time scale of the dipolar relaxation will be theoretically determined in the next subsections and compared with the time scale of the Rabi oscillations.

6.2 Differential equation of dipolar relaxation

For dipolar relaxation as an example of a two-body interaction, a differential equation of the density can be found that is similar to that for one body processes, except that the change in density in time for the two-body interaction is proportional to the square of the density, with a dipolar loss coefficient β. In general, the two atom processes of dipolar relaxation dominate and it is reasonable to neglect one-body processes. With this assumption the overall result is [Pas+10]

$$\frac{dn}{dt} = -\beta n^2. \tag{6.53}$$

At this point it should be noted that equation (6.53) is only valid locally, as the density is location-dependent. To obtain a formula for the total atom number one has to integrate over the volume of the thermal cloud. The density distribution of a thermal cloud is generally given by

$$n(\vec{r}) = n_0 \, \exp\left(-\frac{x^2}{\sigma_x^2} - \frac{y^2}{\sigma_y^2} - \frac{z^2}{\sigma_z^2}\right) \tag{6.54}$$

with n_0 being the center density that was already calculated during the photon and atom density comparison in the appendix in equation (13.119). Here $\sigma_{x,y,z}$ is a measure of the expansion of the thermal cloud in the corresponding spatial direction. The concrete values for $\sigma_{x,y,z}$ can be theoretically determined from the equipartition theorem. This results in an analytical formula depending on the trapping frequencies $\omega_{x,y,z}$, which have been measured to be $[\omega_x, \omega_y, \omega_z] = [281.7, 151.7, 314.9]$ Hz. With this one obtains

$$\sigma_{x,y,z} = \sqrt{\frac{k_\mathrm{B} T}{m\omega_{x,y,z}^2}}. \tag{6.55}$$

This finally leads to a DE of the total atom number

$$\begin{aligned} \frac{dN}{dt} &= \beta \int n(\vec{r})^2 \, d\vec{r} \\ &= \beta \, n_0^2 \pi^{\frac{3}{2}} \, \sigma_x \sigma_y \sigma_z \\ &= N^2 \beta \, \frac{\omega^3}{2^{\frac{3}{2}}} \left(\frac{m}{2\pi \, k_\mathrm{B}}\right)^{\frac{3}{2}} \frac{1}{T^{\frac{3}{2}}} \end{aligned} \tag{6.56}$$

where in the last equation, the definition of the geometric average ω of the trapping frequencies $\omega_{x,y,z}$ (shown in equation (13.120) in the appendix) as well as equation (13.119) have been used. It must be noted here that the temperature also has a time dependency, as dipolar relaxation induces heating by preferably depleting the central part of the trap. A differential equation of temperature can be derived as [Web+03] [Wel+23]

$$\frac{\dot{T}}{T} = \frac{\dot{N}}{N} \, \frac{E_{\mathsf{Av}} - E_{\mathsf{Loss}}}{E_{\mathsf{Av}}}. \tag{6.57}$$

The heating energy corresponds to the difference between the average energy E_{Av} and the loss energy E_{Loss} of the dipolar relaxation. The loss energy corresponds to the mean of the potential of the atom trap weighted with the square density and normalized to the mean of the weight, namely the square density. With the trapping frequencies $\omega_{x,y,z}$ the potential of the atom trap can be described as the potential of a harmonic oscillator

$$V(x,y,z) = m \, \frac{\omega_x^2 x^2}{2} + m \, \frac{\omega_y^2 y^2}{2} + m \, \frac{\omega_z^2 z^2}{2}. \tag{6.58}$$

The quadratic density over the volume has already been calculated in equation (6.56) while the calculations of the mean of the trap potential weighted with the quadratic density have been made in the appendix in subsection A.1.3 and lead to

$$\iiint n^2(r) \, V(r) \, d^3r = \frac{m \, n_0^2}{4} \, \pi^{\frac{3}{2}} \, \sigma_x \sigma_y \sigma_z \, \left(\sigma_x^2 \omega_x^2 + \sigma_y^2 \omega_y^2 + \sigma_z^2 \omega_z^2 \right). \tag{6.59}$$

Using the equipartition theorem from equation (6.55) this leads to a loss energy of

$$E_{\mathsf{Loss}} = \frac{\iiint n^2(r) \, V(r) \, d^3r}{\iiint n^2(r) \, d^3r} = \frac{3 k_{\mathsf{B}} T}{4}. \tag{6.60}$$

This result finally provides a differential equation for the temperature development with time, which has a non trivial dependence of the overall atom number and is given as

$$\dot{T} = N \, \frac{\omega^3 \beta}{8 \sqrt{2}} \, \left(\frac{m}{2\pi k_{\mathsf{B}}} \right)^{\frac{3}{2}} \, \frac{1}{T^{\frac{1}{2}}}. \tag{6.61}$$

Thus the dipolar relaxation process can be described by a coupled system of two non-linear differential equations displayed in equation (6.56) and equation (6.61).

6.3 Determination of the loss coefficient

After deriving the two coupled differential equations, which are represented in equation (6.56) and equation (6.61), the crucial dipolar loss parameter still has not yet been treated. This will now be done before two methods of solving the coupled differential equations are presented.

For this it should be first noted, that dipolar relaxation processes do not conserve the spin but rather the total angular momentum [Hen+03]. In the following, a system which is polarised in the highest possible energetic Zeeman sublevel $m_J = +J$ is exemplary considered, since this case is

analytically easy to calculate and only non-spin maintaining processes contribute to the atom loss. In this system, two different decay channels are present because the magnetic quantum number can decrease by one or two. The cross sections of the decay channels $\sigma_{1,2}$ and the cross section of the elastic dipole interactions σ_0 are [Pas+10] [Cho+22]

$$\begin{aligned}
\sigma_0 &= \frac{16\pi}{45}\, S^4 \left(\frac{\mu_0 (g_J \mu_\mathsf{B})^2 m}{4\pi\hbar^2}\right)^2 (1 + \epsilon h(1)) \\
\sigma_1 &= \frac{8\pi}{15}\, S^3 \left(\frac{\mu_0 (g_J \mu_\mathsf{B})^2 m}{4\pi\hbar^2}\right)^2 \left(1 + \epsilon h\left(\frac{k_\mathsf{f}}{k_\mathsf{i}}\right)\right) \frac{k_\mathsf{f}}{k_\mathsf{i}} \\
\sigma_2 &= \frac{8\pi}{15}\, S^2 \left(\frac{\mu_0 (g_J \mu_\mathsf{B})^2 m}{4\pi\hbar^2}\right)^2 \left(1 + \epsilon h\left(\frac{k_\mathsf{f}}{k_\mathsf{i}}\right)\right) \frac{k_\mathsf{f}}{k_\mathsf{i}}
\end{aligned} \tag{6.62}$$

with $f(u)$ being a function, that is defined as

$$f(u) = -\frac{1}{2} - \frac{3}{8}\, \frac{(1-u^2)^2}{u\,(1+u^2)}\, \log\left(\frac{(1-u)^2}{(1+u)^2}\right). \tag{6.63}$$

Here ϵ is a parameter which value is based on the statistics of the particles. Since Dy^{164} has a bosonic characteristic, the parameter is set to $\epsilon = 1$ [Hen+03]. The argument of the function $f(u)$ is given by the ratio of the incoming and outgoing wave vector $u = \frac{k_\mathsf{f}}{k_\mathsf{i}}$. From the energy conservation equation, the ratio can be determined for a given change in the magnetic quantum number Δm_J as

$$\frac{k_\mathsf{f}}{k_\mathsf{i}} = \sqrt{1 + \frac{m \Delta E_{\Delta m_J}}{\hbar^2 k_\mathsf{i}^2}}. \tag{6.64}$$

By multiplying the cross section by the initial relative velocity v between a pair of particles, and taking a thermal average $\langle\cdot\rangle_\mathsf{th}$ the loss rate in units of volume per time follows [Cho+22]

$$\beta_{1,2} = 2\,\langle \sigma_{1,2} v \rangle_\mathsf{th} \qquad \text{with} \qquad v = \frac{\hbar k_\mathsf{i}}{m}. \tag{6.65}$$

The collision loss rates for both decay channels and different temperatures are shown in figure 21.

Therefore the loss rate increases monotonically with increasing magnetic field. In the case of fermions, on the other hand, the loss rate is several orders of magnitude lower and decreases monotonically with increasing magnetic field [Cho+22]. Since the magnetic field strength was determined in subsection 5.1 to be $B_{z,\mathsf{exp}} = (2.42494 \pm 0.00008)$ G for the test measurement in subsection 6.1, a dipolar relaxation rate of $\beta \approx 54.06\,\mu\mathrm{m}^3\,\mathrm{s}^{-1}$ is assumed in the next sections.

6.4 Analytical solution

At this point, a procedure will be presented which allows to obtain an analytical solution. However, for this solution method a non-trivial ansatz is needed, which is inspired by and derived from the three body losses presented in [Kra06]. The approach for particle number $N(t)$ and temperature $T(t)$ considering also one atom processes will be

$$N(t) = N_0\, \exp(-\alpha t)\, x^{-\epsilon} \qquad \text{and} \qquad T = T_0\, x^{\delta} \qquad \text{with} \qquad x = 1 + \frac{\gamma N_0}{\epsilon T_0^{\frac{3}{2}}\, \alpha}\, (1 - \exp(-\alpha t)). \tag{6.66}$$

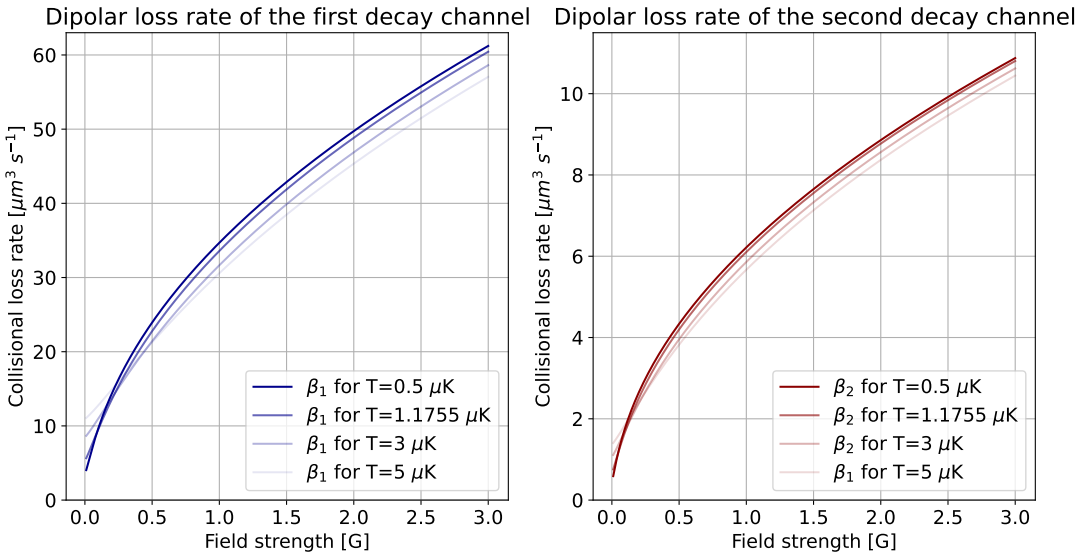

Figure 21: Dipolar relaxation rate of both decay channels of bosonic dysprosium as a function of field strength for different temperatures. In the above plot the values are given in $\mu\mathrm{m}^3\,\mathrm{s}^{-1}$ independent of the density of the thermal cloud. Under experimental conditions, a temperature of $T \approx 1.1755\,\mathrm{K}$ is realised in the experimental chamber. The dipolar loss rate increases monotonically with stronger magnetic fields. In contrast to that, for fermions the loss rates decrease with stronger magnetic fields [Cho+22].

Here ϵ and δ are arbitrary variables. Differentiation from this approach and comparison with the differential equation for dipolar relaxation considering also one atom processes allows values for ϵ and δ to be derived. So it is demanded

$$\begin{aligned} \dot{N} &= -\alpha N - \gamma \frac{N_0^2 \, \exp(-2\alpha t)}{T_0^{\frac{3}{2}} \, x^{\epsilon+1}} \stackrel{!}{=} -\alpha N - \gamma \frac{N^2}{T^{\frac{3}{2}}} = -\alpha N - \gamma \frac{N_0^2 \, \exp(-2\alpha t)}{T_0^{\frac{3}{2}} \, x^{2\epsilon} \, x^{\frac{3\delta}{2}}} \\ \dot{T} &= x^{\delta-1} \frac{\delta\gamma}{\epsilon} \frac{N_0 \, \exp(-\alpha t)}{T_0^{\frac{1}{2}}} \stackrel{!}{=} \frac{\gamma}{4} \frac{N}{T^{\frac{1}{2}}} = \frac{\gamma}{4} \frac{N_0 \, \exp(-\alpha t)}{T_0^{\frac{1}{2}} \, x^{\epsilon} \, x^{\frac{\delta}{2}}} \end{aligned} \tag{6.67}$$

where for simplicity

$$\gamma = \frac{\beta}{2^{\frac{3}{2}}} \, \omega^3 \left(\frac{m}{2\pi \, k_B} \right)^{\frac{3}{2}} \tag{6.68}$$

has been defined. From these demands, conditions for the variables ϵ and δ can be derived in the next step which are given as

$$\text{I)} \quad \epsilon + 1 = 2\epsilon + \frac{3\delta}{2} \qquad \text{II)} \quad \frac{\delta}{\epsilon} = \frac{1}{4} \qquad \text{III)} \quad \epsilon + \frac{\delta}{2} = -\delta + 1. \tag{6.69}$$

These conditions are satisfied by $\epsilon = \frac{8}{11}$ and $\delta = \frac{2}{11}$. Altogether, this leads to an analytical solution of the coupled nonlinear differential equation from dipolar relaxation. If the one atomic interaction processes are neglected, so the limit $\alpha \to 0$ is considered, the solution is given as:

$$N(t) = N_0 \left(1 + \frac{11\,\gamma N_0}{8\,T_0^{\frac{3}{2}}}\,t\right)^{-\frac{8}{11}}$$
$$T(t) = T_0 \left(1 + \frac{11\,\gamma N_0}{8\,T_0^{\frac{3}{2}}}\,t\right)^{\frac{2}{11}} \tag{6.70}$$

The fact that these are actual solutions and the limit of neglecting one atom processes is demonstrated in more detail in the appendix in subsection A.1.4. Due to the complexity of the differential equations and the need of a nontrivial ansatz, an additional numerical approach is presented in the appendix in subsection A.2.4. The analytical and numerical solution of atom number and temperature are shown in figure 22. As initial parameters $N_0 = 7.98 \cdot 10^5$ and $T_0 = 1.1755\,\mu$K were used as determined in the appendix in A.2.3 for the relevant configuration of the experiment.

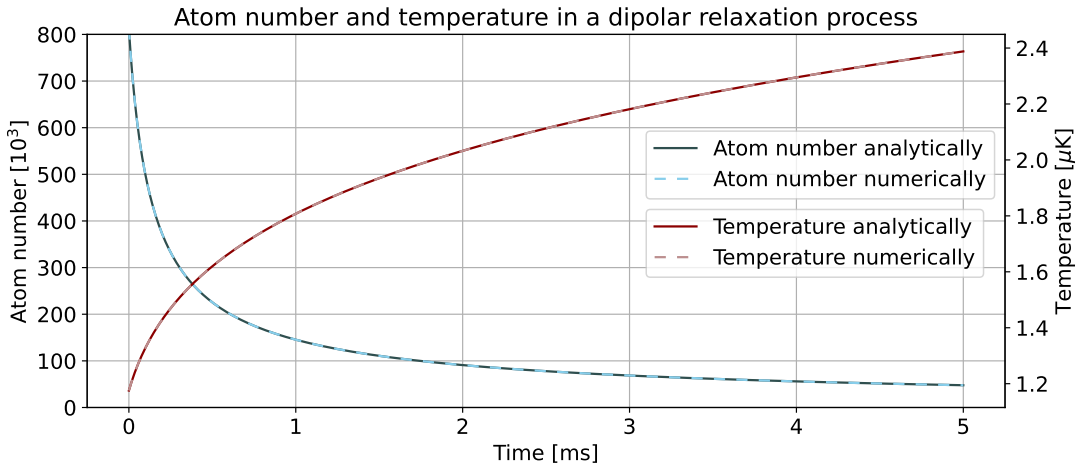

Figure 22: Atomic number and temperature dependent on time during a dipolar relaxation process. The differential equation of dipolar relaxation has been solved numerically with the Runge Kutter method and analytically via a non trivial ansatz. In this plot both solving methods are compared.

6.5 Time evolution considering dipolar relaxation processes

Finally, the influence of dipolar relaxation on the time evolution of the states and whether it can be used as an explanation for the absence of a revival in the ground state will be determined. At this point, however, it must be remembered that this is only an estimate, since a stretched state with $m_J = 8$ was assumed for the calculation of the dipolar loss factor β for reasons of calculability. In reality, however, the loss rates vary between the individual Zeeman sublevels. In the following, it is further assumed that the probability amplitude of a certain state is scaled with the ratio of the existing atoms to the initial atomic number. These assumptions lead to a time evolution, which is shown in figure 23.

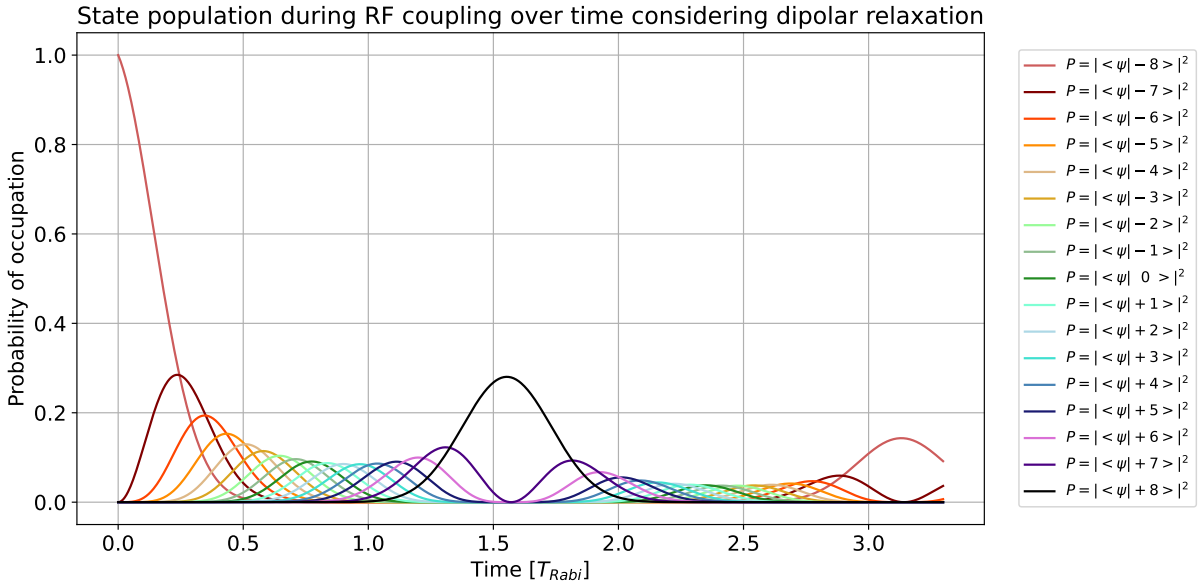

Figure 23: Time evolution in dysprosium considering dipolar relaxation as two body interaction. The nonlinear coupled differential equations describing the dipolar relaxation are shown in equation (6.56) and equation (6.61), while their analytical solution is shown in equation (6.70). In this simulation of the time evolution a stretched state for the calculation of the dipolar relaxation coefficient β is assumed and further that the probability amplitude of measuring the Zeeman sublevels scales with the ratio of momentary atomic number to initial atomic number.

It is obvious that the probability of finding an atom again in the ground state $m_J = -8$ after an oscillation period has strongly decreased, which confirms the initial assumption that dipolar relaxation could be the cause for an absence of oscillation. The remaining part of the atoms in the ground state can easily remain undetected in the noise of the absorption imaging data. Since it is very difficult from a technical point of view to suppress the losses due to dipolar relaxation, the next two sections will discuss other ways of making oscillations in dysprosium measurable.

Conclusion

It is known from theory that Rabi oscillations occur in dysprosium under excitation with radio frequency magnetic fields near the resonance frequency. However, these oscillations could not be measured in the experiment. The cause identified in this subsection is dipolar relaxation as a two-body loss process. Based on its differential equation and its loss coefficient, an analytical solution was determined and an alternative numerical solution method using the Runge-Kutter method was presented in the appendix in subsection A.2.4. Based on the solution, and assuming that the probability of measuring an atom in a given sublevel decreases with the atom loss, the time evolution of subsection 3.4 was adapted to consider this loss process. It has been shown that the time scale of dipolar relaxation is shorter than that of Rabi oscillations, so that the revival is lost in the background noise during measurements.

Time evolution of Dysprosium considering dipolar relaxation

The adjacent QR code provides animations of the time evolution as a function of B-field strength and detuning which have been discussed in subsection 3.4. However, it also shows the influence of the dipolar relaxation parameter on the time evolution of dysprosium.

For a better experience, viewing on a computer is recommended. To do this, simply click on the QR code or alternatively enter the following link into a browser: `https://www.maurice-rieger.de/time-evolution`

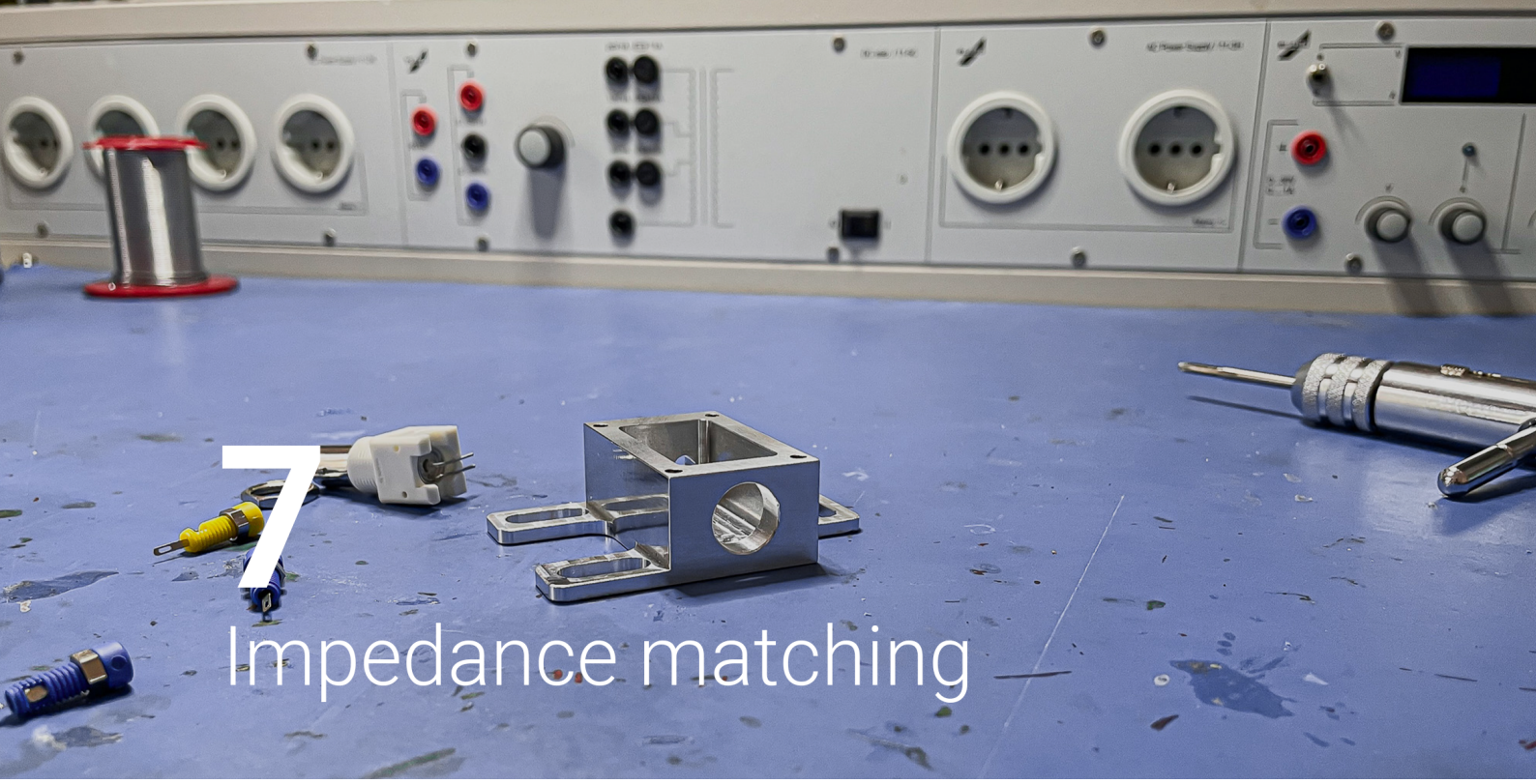

7 Impedance matching

Introduction

It has been shown that dipolar relaxation can indeed be responsible for the absence of a measurable revival. A first approach to still drive measurable oscillations and prepare the system in the stretched spin state is to increase the magnetic field strength of the RF coil. For this purpose, the theoretical basics of impedance matching are explained in subsection 7.1. In subsection 7.2, an optimal matching circuit is determined with the help of a simulation and implemented in the RF mount. Finally, in subsection 7.3 tests of the impedance matched coil are made, focusing in particular on the thermal properties of the matching circuit. With the help of the test measurements, a statement is made as to whether the determined coil configuration is suitable for operation in the experiment.

7.1 Theory of impedance matching

To make Rabi oscillations visible despite dipolar relaxation, one approach is to reduce their period duration. This can be achieved by an amplification of the magnetic field. However, since the magnetic field amplification would need to be ~ 4, this is difficult to achieve only by geometric considerations. This subsection therefore starts at another point, namely the reflection of the input power. In subsection 4.7 it was shown that a large part of the input power (about 94%) is reflected and not converted into an effective magnetic field strength. One method of reducing the proportion is impedance matching, which is explained below.

For DC networks, Jacobi's law states that power transfer is maximised if the source and load have the same resistance [Phi09]. This concept can also be extended to high-frequency AC networks and the impedance Z, defined in equation (4.41). In this more general form, the transferred power is greatest when the load impedance is equal to the complex conjugate of the source impedance. This requires an identical resistance R and sign-inverted reactance X at the ports of source and

load[4]. As already mentioned in subsection 4.3, high-frequency electronic components are mostly standardised to an impedance of $Z_0 = 50\,\Omega$. This also applies to the LZY-22+ amplifier, which acts as the source for the coil. It is useful to define an impedance value Γ which is normalised to the standard impedance Z_0:

$$\Gamma = \frac{Z}{Z_0} \tag{7.71}$$

The optimal parameter value for an ideal power transfer is therefore given by $\Gamma = 1$. One advantage of the definition in equation (7.71) is, that the parameter Γ can be graphically represented in a Smith Chart. For this, it is first noted that in the general definition of Z in equation (4.41), the resistance R can only be positive and the complex vector representation of impedances in the Gaussian number plane occupies only the area with a positive real axis. Therefore, a conformal mapping

$$r(z) = \frac{z-1}{z+1} \tag{7.72}$$

can be applied to the Gaussian plane without any loss of information[5]. The result of the transformation $r(z)$ is shown in figure 24.

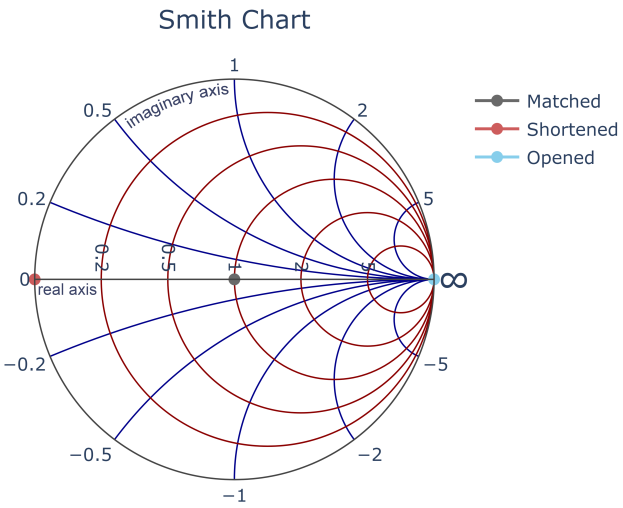

Figure 24: Example of a Smith Chart. The three most prominent points Open, Short and Match are highlighted in colour, corresponding to an infinite impedance, an impedance of 0 and an impedance equal to the reference impedance.

The three most important points are marked in figure 24 being open (for an infinite resistance and a reactance of 0), matched (for the case that the impedance Z is equal to the reference impedance Z_0) and short (for a vanishing impedance). These three points are used in particular when calibrating a network analyser. This so-called Open-Short-Match (OSM) method was carried out before the measurements of this thesis to minimise errors in the data.

In real measurements, usually a frequency range is sampled and the impedance changes depending on the frequency. Therefore, measurements will not produce points in the Smith chart, but rather lines. If this line runs through $\Gamma = 1$, impedance matching is achieved for a specific frequency in the chosen range.

[4] In general, the reactances are so small for low-frequency AC that they can be ignored.
[5] From a mathematical point of view, this is a special case of a Möbius transformation.

7.2 Development of a matching circuit

Having set the objective of matching the impedance Z of the RF coil to the reference impedance Z_0 for a frequency in the frequency range $f \in [2, 10]$ MHz, an appropriate matching circuit is now to be determined in this subsection. For this the S_{11} parameter measurement in subsection 4.7 is used. This data is loaded in the software Qucs Studio [Mar11]. This software calculates an optimal matching circuit based on an .s1p file for a chosen frequency interval in which the S_{11} parameter needs to undercut a certain threshold. The matching circuit shown in figure 25 has proven to be optimal.

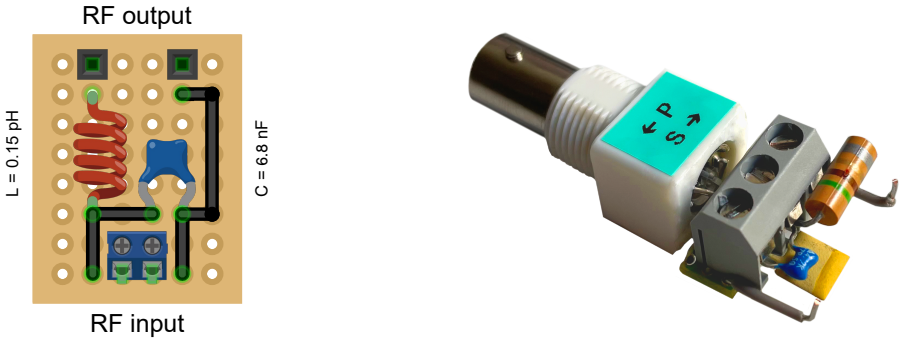

Figure 25: RF coil impedance matching circuit. A schematic drawing is given on the left, while the experimental implementation is shown on the right. The matching circuit consists of a coil with an inductance $L = 0.1$ pH and a capacitor with a capacitance of $C = 6.8$ nF.

The selected matching circuit is a series-connected coil with an inductance of $L = 0.1$ pH and a parallel-connected capacitor with a capacitance of $C = 6.8$ nF. During construction, attention was paid to a modular compact design that fits into the mount developed in subsection 4.4. This configuration achieves a S_{11} parameter of -5.712 dB for an RF frequency of $f = 3.641$ MHz, which corresponds to an effective power fraction of $\sim 73.16\%$. The complete S_{11} parameter measurement is shown in figure 26.

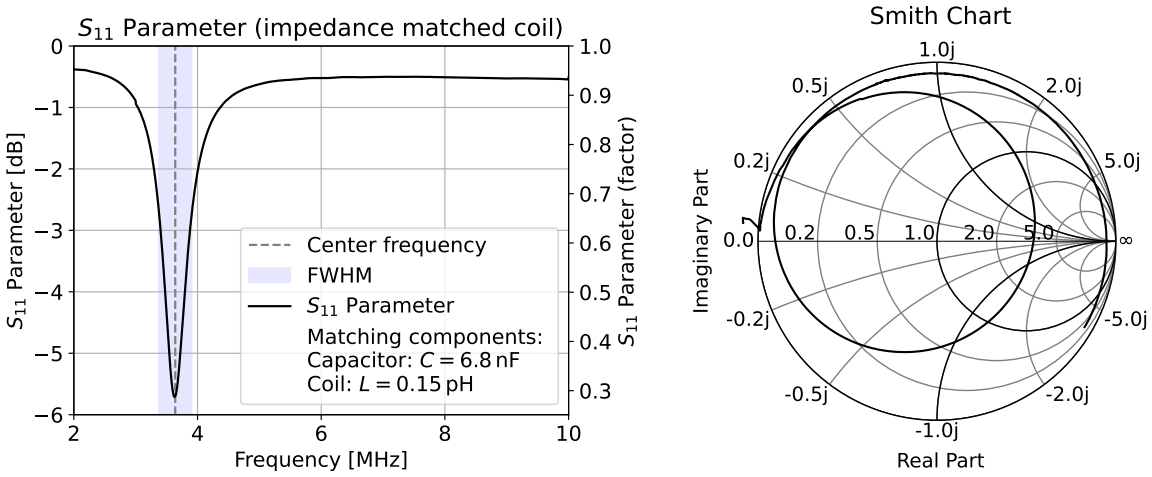

Figure 26: In the left plot the S_{11} parameter of the impedance matched coil depending on the frequency for $f \in [2, 10]$ MHz is shown. The center frequency is marked with a dotted line and the full width at half maximum (FWHM) is marked by a transparent background coloring. In the right plot the real and imaginary part of the impedance are shown in a Smith chart for the frequency range $f \in [0, 30]$ MHz.

A resonance peak is noticeable while the other frequency ranges are not subject to strong changes,

so that the amplified field strength occurs only in a small region with FWHM $= 0.532$ MHz.

7.3 Testing the impedance matched coil

Prior to installation in the experiment, a load test was carried out on the impedance-matched RF coil since the considerably higher effective power could cause the coil to heat up more. The test was carried out at the resonance frequency, where the input voltage fed into the LZY-22+ amplifier was increased stepwise by 100 mV. At an input voltage of $V_{\text{pp}} = 400$ mV, significant heating was observed, not of the RF coil but of the electronic components used in the matching circuit. However, in real experimental conditions, the coil is not operated continuously, but in very small time intervals with a duty cycle $< 1\%$. Since the waveform generator used for the test measurements only allowed a minimum duty cycle of 20% the coil was tested again under these conditions. It was found that heating now only occurred from an input voltage of $V_{\text{pp}} = 800$ mV on. In figure 27 an infrared image of the matching circuit is displayed which shows the heating of the components, while the RF coil itself shows no significant temperature change.

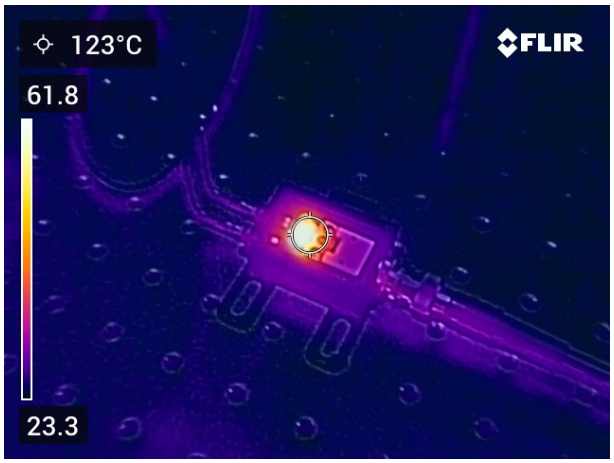

Figure 27: Thermal image of the impedance matching circuit of the radio frequency coil. The temperature is color coded with a scale on the left. The center temperature, which is caused by the capacitor is over $100°$C.

In this figure the heating process is in a thermal equilibrium with a maximal temperature of the capacitor of $123°$C. To prevent the testing setup from taking damage higher input powers have not been investigated. Due to the high sensitivity and the position of the matching circuit in the holder next to the experimental chamber, active air cooling was not an option due to the caused vibration. A rough measurement of the magnetic field strength using a pick-up coil revealed that the strength of the magnetic field was of the same order of magnitude as the field of the non-impedance matched coil, despite a lower input power than the $V_{\text{pp}} = 3$ V used for the field calibration[6]. This shows the potential that impedance matching offers for increasing the RF field strength. To obtain an estimate of the coil behaviour in the experimental setup with duty cycles $\sim 1\%$, it is assumed that the coil behaves identically for equal time-averaged input powers. Since the duty cycle will be reduced by a factor of 20 compared to the test measurement, the input power could increase by a factor of 20 for the same matching circuit heating. With equation (4.35) this corresponds to an increase of the input voltage by a factor ~ 4.47 to $V_{\text{pp}} \approx 3.58$ V, where the RF amplifier already goes into power saturation. This suggests that the use of an impedance matched coil is a suitable option to make the Rabi oscillations in dysprosium measurable despite dipolar relaxation processes.

[6] It was found that in the regime relevant for the experiment, the RF amplifier goes into power saturation at roughly this voltage value, since the output power is limited to $P = 30$ W.

Conclusion

In the experiment, it is desirable to make the Rabi oscillations measurable so that an experimental comparison of the revival time can be obtained and the atoms can be prepared in the spin state $|+8\rangle$. In this subsection, the possibility of amplifying the magnetic field, which would cause an earlier revival time, is discussed. Since a strengthening factor of ~ 4 would have to be achieved, impedance matching is a more promising method than changing the coil geometry. With the help of a simulation software, an ideal matching circuit was determined (see figure 25), which was built into the RF mount in a modular and compact form. The matching circuit increased the effective power from $\sim 6\%$ to over 70% within a small resonance range at $f \approx 0.532\,\mathrm{MHz}$. Test measurements of this coil have shown that the increased power leads to a significant heating of the matching circuit already at input voltages below $1\,\mathrm{V}$ (a smallest possible duty cycle of 20% was chosen). Test measurements of the magnetic field using a pick-up coil and spectrum analyser have shown that even for these lower input voltages a comparable strength to the non-matched coil occurs. Since the coil is only operated with a duty cycle of $\sim 1\%$ in the experiment, it has been estimated that an operation with the same power as the normal coil ($3\,\mathrm{V}$) is possible with the assumption that the thermal properties depend exclusively on the time-average of the input power. Thus, impedance matching is a valid method to drive oscillations in dysprosium.

8 Isolation of a two level system

Introduction

In this section, the possibility of preparing the system in the $|-7\rangle$ spin state using Rabi oscillations is presented. The foundation is the nonlinear AC Stark effect, which couples with different strength to the different dysprosium sublevels. In subsection 8.1 the theoretical basics of the AC Stark effect and the possibility of isolating a two-state system by means of an additional laser are discussed. In these considerations, the polarizability is of crucial importance and is treated in more detail in subsection 8.2. In subsection 8.3, the energy shift, scattering rate and lifetime are derived from the polarizability. With these quantities, the concept of isolation of a two-state system is precisely defined in subsection 8.4. It is shown that such an isolation of the $|-8\rangle$ and $|-7\rangle$ states can occur. Since a perfect polarisation of the Stark shift laser was assumed in the simulations, which cannot be realised in the experiment, the influence of a polarisation perturbation on the isolation of the states is investigated in subsection 8.5.

8.1 AC Stark effect

Considering an atom in an alternating (AC) electric field, an additional term is added in the Hamilton operator. In a first order perturbative treatment, this term is given as[7]

$$H_{\mathsf{El}} = \vec{p} \cdot \vec{E} = \alpha \, \vec{E}^2. \tag{8.73}$$

with the induced electric dipole moment $\vec{p} = \alpha \vec{E}$ and the electric field vector $\vec{E}$. Here α is the complex polarizability of the atoms, governing the interaction strength between the atoms and the external electric field. Since light is an electromagnetic alternating field, laser radiation is also expected

[7] If one accounts for the complex atomic structure there are some subtleties, which will not be mentioned here. For further reading it is referred e.g. to [DK99].

to shift the atomic energy levels. If the frequency of the light approaches the energy difference of an atomic transition, a resonance phenomenon can occur, which is from crucial importance here [DK99].

In a non-vanishing magnetic field the dysprosium ground state splits into 17 energetically equidistant sublevels (see subsection 3.1). However, the AC Stark effect is a non-linear effect that couples with different strength to different sublevels. In theory, this opens the possibility of isolating two sublevels in such a way that RF frequencies drive transitions between these two states just like in a two level system[8] that has been discussed in subsection 3.3.

8.2 Polarizability of Dysprosium

In equation (8.73) it is shown that the energy shift depends on the polarizability of dysprosium, which will be considered in more detail below. In general the polarizability depends on the exact state configuration of the atoms and on the alternating electric field frequency. The total polarizability α can be split into a scalar, a vector and a tensor polarizability that are given as [Li+17]

$$\begin{aligned}
\alpha_{\text{scal}}(\omega) &= -\alpha_0(\omega)\,\frac{1}{\sqrt{3\,(2J+1)}} \\
\alpha_{\text{vec}}(\omega) &= \alpha_1(\omega)\,\sqrt{\frac{2J}{(J+1)\,(2J+1)}} \\
\alpha_{\text{tens}}(\omega) &= \alpha_2(\omega)\,\sqrt{\frac{2J\,(2J-1)}{3\,(J+1)\,(2J+1)\,(2J+3)}}.
\end{aligned} \tag{8.74}$$

If one defines the index $k = 0, 1, 2$ to represent the scalar, vector or tensor part of the polarizability, the real and imaginary part of the variable α_k can be calculated as [Li+17]

$$\begin{aligned}
\text{Re}[\alpha_k(\omega)] = \sum_{n_2'' \, l_2''} & \frac{\omega_{n_2'' \, l_2''} \delta_{(-1)^k,1} - \omega\,\delta_{(-1)^k,-1}}{\omega^2_{n_2'' \, l_2''} - \omega^2}\;\frac{2\,\sqrt{2k+1}}{\hbar}\;(1+\delta_{n_1\,n_2}\delta_{l_1\,l_2})\;(1+\delta_{n_1\,n_2''}\delta_{l_1\,l_2''}) \\
& \cdot (-1)^{J+J_c-S_\nu+l_1+l_2''+k}\,(2J+1)\,(2J_\nu+1)\,(2L_\nu+1)\,(2l_2+1)\,(2l_2''+1) \\
& \cdot \begin{Bmatrix} J_\nu & J_c & J \\ J & k & J_\nu \end{Bmatrix} \begin{Bmatrix} L_\nu & S_\nu & J_\nu \\ J_\nu & k & L_\nu \end{Bmatrix} \begin{Bmatrix} l_2 & l_1 & L_\nu \\ L_\nu & k & l_2 \end{Bmatrix} \begin{Bmatrix} 1 & 1 & k \\ l_2 & l_2 & l_2'' \end{Bmatrix} \\
& \cdot \begin{pmatrix} l_2'' & 1 & l_2 \\ 0 & 0 & 0 \end{pmatrix}^2 e^2 r^2_{n_2 l_2, n_2'' l_2''}
\end{aligned} \tag{8.75}$$

[8] In fermionic atoms the energy splitting gets nonlinear for strong magnetic fields. For each pair of $|m_F\rangle$ states of a given total angular momentum quantum number $|\vec{F}| = |\vec{J} + \vec{I}|$ different energy spacings are obtained. Therefore a two state system can be isolated using strong magnetic fields. Excitation with the energy resonance frequency and using the time evolution of a two state system, described in subsection 3.3 allows to prepare specific spin states.

$$
\begin{aligned}
\mathrm{Im}[\alpha_k(\omega)] = \sum_{n_2'' \, l_2''} & \frac{\left(\omega_{n_2'' \, l_2''}^2 + \omega^2\right) \, \delta_{(-1)^k,1} - 2\omega \, \omega_{n_2'' \, l_2''} \, \delta_{(-1)^k,-1}}{\left(\omega_{n_2'' \, l_2''}^2 - \omega^2\right)^2} \\
& \cdot \frac{\omega_{n_2'' \, l_2''}^3 \sqrt{2k+1}}{3\pi\epsilon_0\hbar^2c^3} \left(1 + \delta_{n_1 \, n_2}\delta_{l_1 \, l_2}\right)^2 \left(1 + \delta_{n_1 \, n_2''}\delta_{l_1 \, l_2''}\right)^2 \\
& \cdot (-1)^{J+J_c-S_\nu+l_1+l_2''+k} \left(2J+1\right)\left(2J_\nu+1\right)\left(2L_\nu+1\right)\left(2l_2+1\right)^2\left(2l_2''+1\right) \\
& \cdot \begin{Bmatrix} J_\nu & J_c & J \\ J & k & J_\nu \end{Bmatrix} \begin{Bmatrix} L_\nu & S_\nu & J_\nu \\ J_\nu & k & L_\nu \end{Bmatrix} \begin{Bmatrix} l_2 & l_1 & L_\nu \\ L_\nu & k & l_2 \end{Bmatrix} \begin{Bmatrix} 1 & 1 & k \\ l_2 & l_2 & l_2'' \end{Bmatrix} \\
& \cdot \begin{pmatrix} l_2'' & 1 & l_2 \\ 0 & 0 & 0 \end{pmatrix}^4 e^4 r_{n_2 l_2, n_2'' l_2''}^4
\end{aligned}
\tag{8.76}
$$

with $(:::)$ being the Wigner 3-j symbol and $\{:::\}$ being the Wigner 6-j symbol. These are defined as [VMK88]

$$
\begin{pmatrix} l_1 & l_2 & l_3 \\ m_1 & m_2 & m_3 \end{pmatrix} = \frac{(-1)^{l_1-l_2-m_3}}{\sqrt{2l_3+1}} \left\langle l_1 \, m_1 \, l_2 \, m_2 | l_3 \, (-m_3) \right\rangle
$$

$$
\begin{aligned}
\begin{Bmatrix} l_1 & l_2 & l_3 \\ l_4 & l_5 & l_6 \end{Bmatrix} = \sum_{m_1,\ldots,m_6} & (-1)^{\sum_{k=1}^6} \begin{pmatrix} l_1 & l_2 & l_3 \\ -m_1 & -m_2 & -m_3 \end{pmatrix} \begin{pmatrix} l_1 & l_5 & l_6 \\ m_1 & -m_5 & m_6 \end{pmatrix} \\
& \cdot \begin{pmatrix} l_4 & l_2 & l_6 \\ m_4 & m_2 & -m_6 \end{pmatrix} \begin{pmatrix} l_4 & l_5 & l_3 \\ -m_4 & m_5 & m_3 \end{pmatrix}.
\end{aligned}
\tag{8.77}
$$

Considering a magnetic field (which sets the quantisation axis of the atoms) and a specific magnetic quantum number, the total polarizability can be calculated from the scalar, vector and tensor polarizability as [Pat+21]

$$
\alpha = \alpha_{\mathrm{scal}} + \alpha_{\mathrm{vec}} \, v_{m_J} \, v_{\theta_B} + \alpha_{\mathrm{tens}} \, t_{m_J} \, t_{\theta_B}. \tag{8.78}
$$

In this formula v_{θ_B} and t_{θ_B} take into account the orientation of the $\vec{B}$-field relative to the z axis and a custom polarisation $\vec{P}$ of the external light source. They are defined as

$$
v_{\theta_B} = \mathrm{Re}\left(i \, \frac{\vec{B}}{|\vec{B}|} \cdot (\vec{P} \times \vec{P}^*)\right) \qquad \text{and} \qquad t_{\theta_B} = \frac{3}{2}\left(\frac{\vec{B}}{|\vec{B}|} \cdot \vec{P}\right)^2 - \frac{1}{2}. \tag{8.79}
$$

The prefactors v_{m_J} and t_{m_J} take into account the m_J state, for which the polarizability shall be calculated and can be determined as

$$
v_{m_J} = \frac{m_J}{2J} \qquad \text{and} \qquad t_{m_J} = \frac{3\,m_J^2 - J\,(J+1)}{J\,(2J-1)}. \tag{8.80}
$$

In general the polarizability α is a complex quantity with its real part describing the in-phase component of the dipole oscillation being responsible for the dispersive properties of the interaction while

the imaginary part describes the out-of-phase oscillation component [GWO00]. The real part allows to calculate the energy shift of the different sublevels while the imaginary part is related to the photon scattering rate [Li+16]. In figure 28 the real and imaginary values of the scalar, vector and tensor polarizability of the $|-8\rangle$ state are plotted. A C++ code which calculates the polarizabilities of dysprosium from spectroscopic data, namely the transition frequencies, the linewidth and the total angular momentum of the states, is given in the appendix in subsection A.3.4. The data for a predefined wavelength range is saved it in a text file.

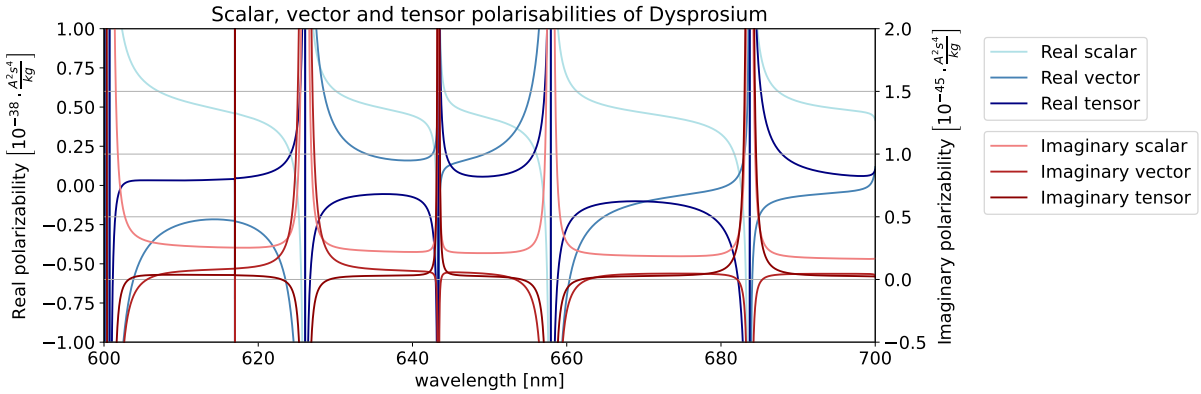

Figure 28: Real and imaginary part of the scalar, vector and tensor polarizability of the dysprosium $|-8\rangle$ state for the wavelength range $\lambda \in [600, 700]$ nm. The left y axis describes the real part while the right one describes the imaginary part.

In the regime close to atomic resonances, the polarizabilities approach plus or minus infinity asymptotically and mark exactly the frequencies where the photon energy matches the energetic spacing of the sublevels. In table 4 an overview of three relevant resonances within the $\lambda \in [600, 700]$ nm interval is provided (see [MC61] [Gus+79] [LYL11] [Sch+13]).

Wavelength [nm]	Frequency [THz]	Linewidth $[10^3\,\mathrm{cm}^{-1}]$	Quantum number $(J \to J')$
626.082	478.839	136	$8 \to 9$
657.937	455.655	123	$8 \to 7$
683.731	438.466	95	$8 \to 8$

Table 4: Spectroscopic data of the three most important resonances for $\lambda \in [600, 700]$ nm. Given are the wavelengths, frequencies, line widths and the change in the total angular momentum quantum number.

For a B-field angle $\theta = 0°$ the total polarizabilities are shown in figure 30 for different polarisations of the external light source and all different Zeeman sublevels. It is evident that the surroundings of the resonance areas are more influenced by circular polarized external light than for linear polarized light. The polarisation axis of the linear polarisation only contributes to the tensorial part of the polarizability. Therefore the differences between a vertical, horizontal and diagonal polarisation is small in comparison to a σ_+ and σ_- polarisation. Furthermore in the circular case, the order of the individual Zeeman sublevels is inverted when the polarisation direction is changed.

8.3 Energy shift, scattering rate and lifetime

Based on the polarizabilities, one can calculate the energy shifts of the individual Zeeman sublevels, depending on the excitation frequency and the polarisation of the external light source. The potential energy can be calculated as [Li+16]

$$U = -\frac{I}{2\epsilon_0 c}\,\mathrm{Re}(\alpha). \tag{8.81}$$

In a similar way it is possible to calculate the scattering rate from the polarizability as

$$\Gamma = \frac{I}{\hbar\epsilon_0 c}\,\mathrm{Im}(\alpha). \tag{8.82}$$

Since the inverse of the scattering rate corresponds to the lifetime of the atoms it can be expressed in terms of the energy shift in equation (8.81) and the polarizability which leads to

$$\tau = \frac{1}{\Gamma} = -\frac{\hbar}{2U}\,\frac{\mathrm{Re}(\alpha)}{\mathrm{Im}(\alpha)}. \tag{8.83}$$

Figure 29 shows the potential energy U and the lifetime τ for the polarizabilities calculated in figure 30. The three polarisation directions horizontal, vertical and diagonal can be combined to linear polarisation, as they lead to similar polarizabilities. In the vicinity of the resonances, the potential energies asymptotically tend towards infinity. At the same time, dips occur in the lifetime that mostly reach below the microsecond regime. Interestingly, for some resonances in the case of circular polarisation, no dips in the lifetime occur. In particular, the $\lambda = 657.937\,\mathrm{nm}$ resonance stands out, which shows no influence on the energy or the lifetime in the resonance regime for $m_J = \pm 8$ as well as for $m_J = \pm 7$ in case of $\sigma_\pm$ polarized light.

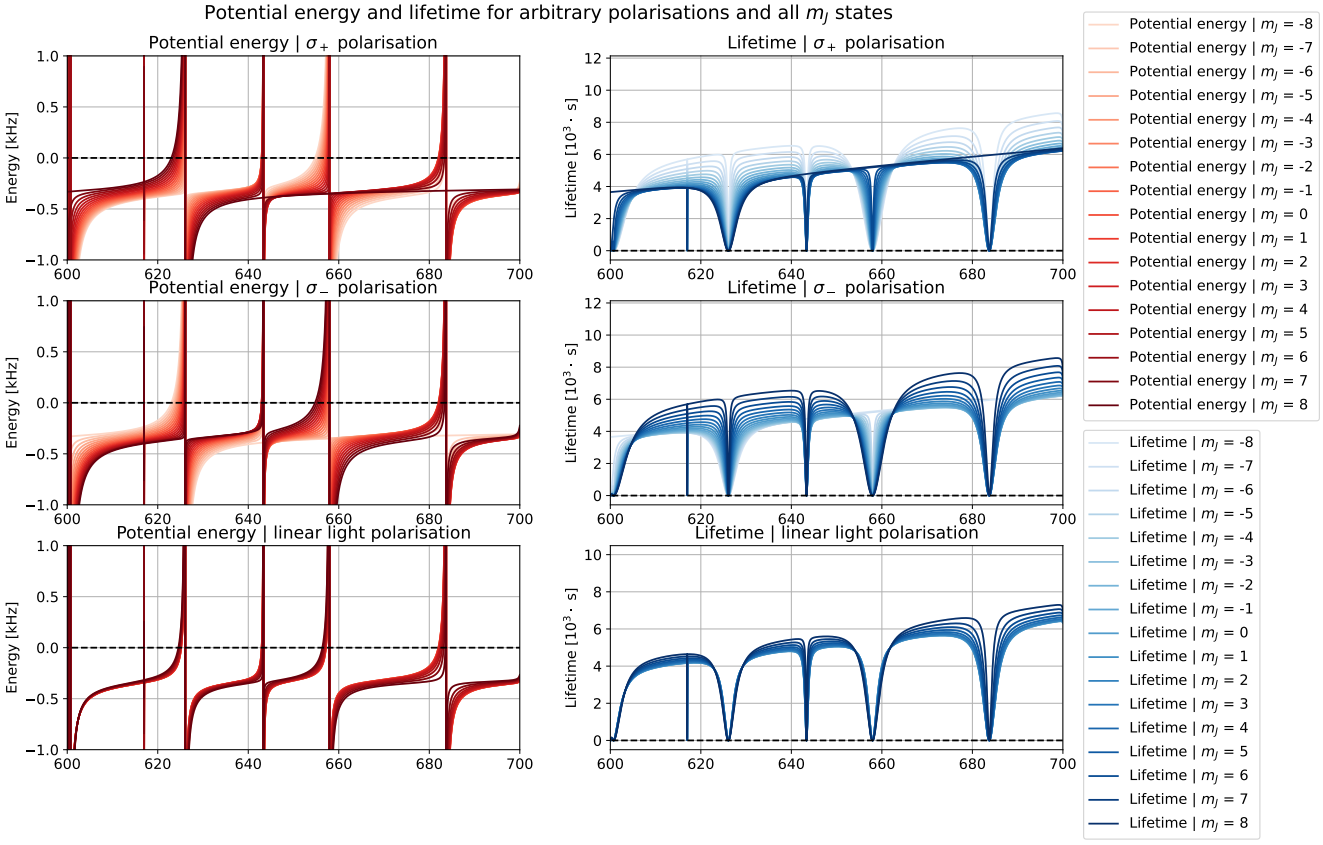

Figure 29: Energy shift and lifetime of the 17 dysprosium sublevels in the ground state for wavelengths $\lambda \in [600, 700]\,\mathrm{nm}$. Since it was shown in figure 30 that the polarisation axis of the external light only has a small influence on the polarizabilities in dysprosium, only a horizontal polarisation is shown exemplary for a linear polarisation.

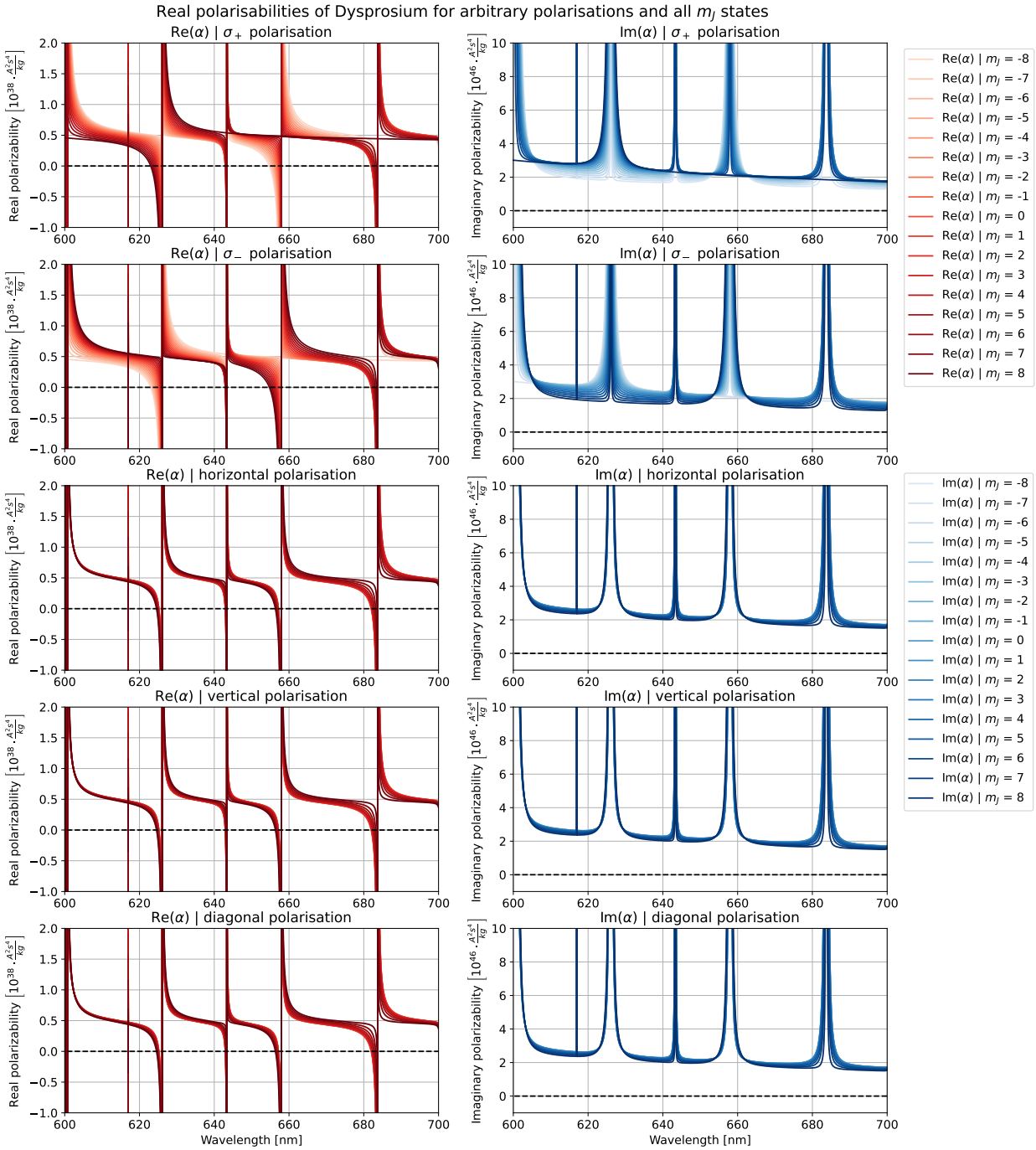

Figure 30: Real and imaginary polarisation of the 17 dysprosium sublevels for wavelengths $\lambda \in [600, 700]\,\mathrm{nm}$. Five different polarisations of the light source are shown, namely σ_+, σ_-, horizontal, vertical and diagonal polarisation.

8.4 Defining conditions to isolate a two level system

Now that the theoretical basics have been covered, a two-state system is to be isolated. Since the actual number of 17 sublevels will not change, it will first be defined what is considered a two-state system here. For a two state system, two criteria are defined: First, the differences between the two energy levels must differ from the energy difference of the other neighbouring Zeeman sublevels by

$\Delta E \geq h \cdot 30\,\text{kHz}$. Second, the system should be reasonably stable with a lifetime of $\tau \geq 1\,\text{s}$ for the two sublevels of interest, so measurements can be performed.

Since the dysprosium atoms are initially in the $m_J = -8$ state, it would be ideal to isolate the $m_J = -8$ and $m_J = -7$ level so no state preparation is necessary in advance. The resonance at $657.937\,\text{nm}$ for a σ_- polarisation of the external light source, has proven to fulfil both criteria, as it can already be seen in figure 29 that the lifetime of $m_J = -8$ and $m_J = -7$ near the resonance is not affected. This behaviour is related to the quantum number J of the states involved. For an atomic transition $\Delta J = 1$ (so in case of dipole radiation) the change of the magnetic quantum number is immediately restricted to the values $\Delta m = 0, \pm 1$. In case of absorbing or emitting light, the magnetic quantum number determines the polarisation, with $\Delta m = 0$ corresponding to a π transition, which is linearly polarised, and the cases $\Delta m = +1$ and $\Delta m = -1$ corresponding to σ_+ and σ_- transitions, which are circularly polarised.

This atomic transition behaviour explains why one does not obtain resonance phenomena for $m_J = -8$ and $m_J = -7$ in the case of σ_- polarisation. For the $657.937\,\text{nm}$ resonance an atomic transition from the ground state $J = 8$ to the first excited energy level $J = 7$ takes place (see table 4). The first excited state of dysprosium, namely $J = 7$ has 15 sublevels with $m_J \in \{-7, \ldots, 0, \ldots, 7\}$. Accordingly, a transition from the ground state for $|J = 8, m_J = -8\rangle$ and $|J = 8, m_J = -7\rangle$ is incompatible with the condition $\Delta m_J = -1$ from the σ_- polarised light, since the states $|J = 7, m_J = -9\rangle$ and $|J = 7, m_J = -8\rangle$ do not exist. Consequently, no resonance phenomena are measurable for these specific states.

In order to finally isolate the two-state system, the energy difference between neighbouring sublevels and the lifetime of the sublevels are shown in figure 31 for a small frequency interval around the resonance at $\lambda = 657.937\,\text{nm}$.

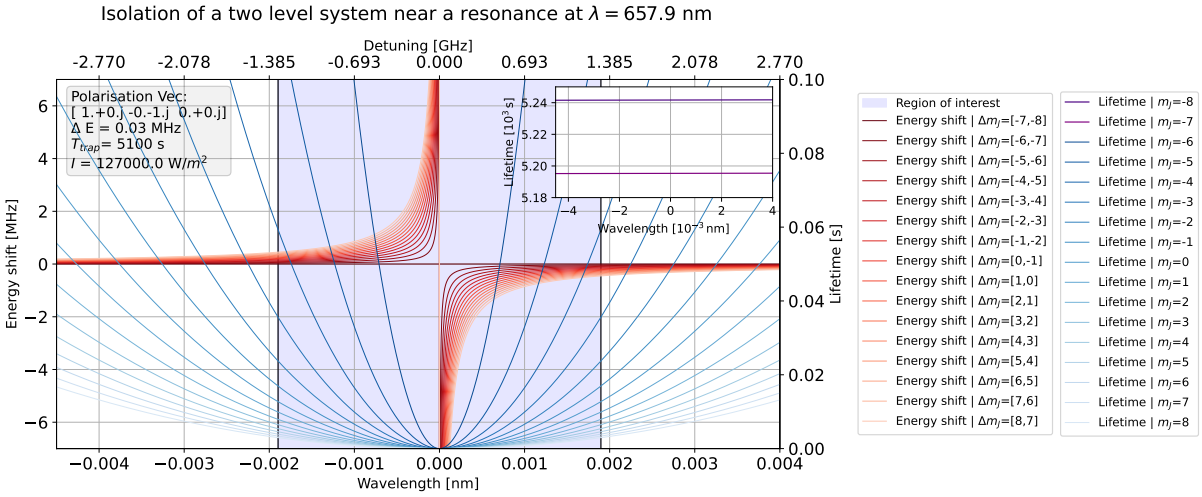

Figure 31: Energy difference of neighbouring states (left y axis) and lifetimes (right y axis) for each state in the region of the $657.937\,\text{nm}$ resonance in Dysprosium. The lifetimes of the $m_J = -8$ and $m_J = -7$ state have been specially colored violet and purple. Since they are not affected by resonance, their scale is about 4 orders of magnitude larger than that of the other lifetimes. Therefore, these are presented in a separate small plot in the top right-hand corner. The region with an energy spacing of $\Delta E > 30\,\text{kHz}$ and a lifetime of $\tau > 1\,\text{s}$ is marked with a blue box. In this region a two level system consisting of the energy levels $m_J = -8$ and $m_J = -7$ has been isolated. For this and all past calculations in this chapter, a light intensity of $I \approx 127000\,\text{W m}^{-2}$ was assumed. This corresponds to a laser beam of diameter $d = 1\,\text{mm}$ with radially constant intensity and a total output power of $P = 1\,\text{mW}$.

Here it is even more clear that the $m_J = -8$ and $m_J = -7$ states are not influenced by the atomic transition of the resonance while all other Zeeman sublevels experience an energy shift. This results in the isolation of $m_J = -8$ and $m_J = -7$, indicated by the blue box where both isolation conditions are fulfilled[9].

8.5 Robustness of the two level system

In the Jones vector notation, the polarisation of the incoming light with σ_- polarisation can be described as $\vec{P} = (1, -i, 0)^\mathsf{T}$, see e.g. [Col05]. Although it is evident that an isolated two-state system can be realised with this polarisation, real light sources never have an absolute polarisation purity. Consequently, the question of the two-state system sensitivity with regard to fluctuations in the polarisation arises. In order to investigate this, the polarisation vector is defined to depend on a dimensionless variable x, that can be interpreted as polarisation imperfection

$$\vec{P}(x) = \frac{1}{\sqrt{(1-x)^2 + (1+x)^2}} \begin{pmatrix} 1-x \\ -(1+x)\, i \\ 0 \end{pmatrix}. \tag{8.84}$$

Figure 32 shows the linear relation between the size s of the relevant regime and the imperfection of the polarisation x. A fit has been used to determine a functional dependence as $s(x) = -(34.7919 \pm 0.0013)\,\mathrm{pm/x}$. This plot also allows to calculate that for $x \geq (5.44842 \pm 0.00023)\,\%$ the two state system criteria are violated regardless of the wavelength.

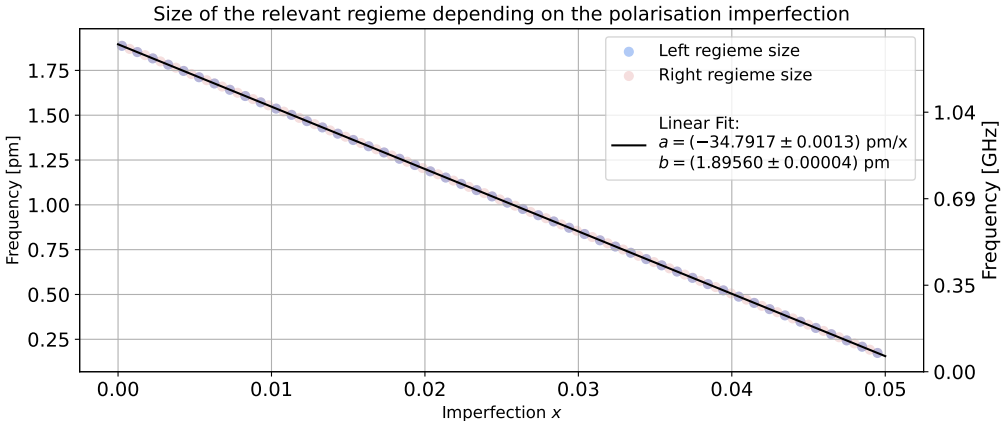

Figure 32: Size of the relevant regime of a two-state system consisting of the energy levels $m_J = -8$ and $m_J = -7$ for σ_- circularly polarised external laser radiation depending on the polarisation imperfection x. The right and left regime have been color coded in the plot and both used for a linear fit.

Conclusion

In this section a method of driving oscillations in an isolated two state system in the dysprosium 17 state system was discussed. This can be achieved using the nonlinear AC Stark effect. Three different resonances are investigated for which energy splitting and lifetime are calculated from the polarizabilities of dysprosium. It turns out that the resonance at $657.937\,\mathrm{nm}$ for a σ_- polarised laser

[9] Since the lifetime of the states of interest is not affected by the resonance, the size of the blue box only depends on the energy splitting.

offers optimal isolation properties. However, since perfect polarisation is not possible, the influence of imperfect polarisation is discussed, where it is found that isolation is possible up to an imperfection of $\sim 5\%$.

In particular, the Rabi oscillations in the isolated two level system allow a preparation of the system in the pure spin state $|-7\rangle$ or spin mixtures between the states $|-7\rangle$ and $|-8\rangle$. With respect to section 7, it must be noted that dipolar relaxation is not directly suppressed by the chosen isolation method of a two-state system. Rather, the loss rate can be influenced by means of energy tuning, whereby a reduction of the Rabi time, for example by impedance matching, may still be necessary to prevent a high atom loss. The investigation of dipolar relaxation in the isolated two-state system goes beyond the scope of this thesis, but offers an interesting point of continuing this work.

Elaboration of this method and repeated application to different pairs of substates would allow the preparation of specific pure spin states. However, it must be noted that for other substates, in addition to the selected $|-8\rangle$ and $|-7\rangle$ states, the lifetime at the resonances will also collapse, which is why two relevant regimes to the right and left of the resonance frequency result, so the AC Stark shift laser must be frequency-locked much more precisely.

Stability of the two state system

The adjacent QR code provides animations of the relevant regime of the two-state system depending on the polarisation imperfection parameter up to an imperfection of about 5%. In addition, there are also animations of the potential energy and lifetime up to an imperfection of 50%.

For a better experience, viewing on a computer is recommended. To do this, simply click on the QR code or alternatively enter the following link into a browser: `https://www.maurice-rieger.de/two-level-system`

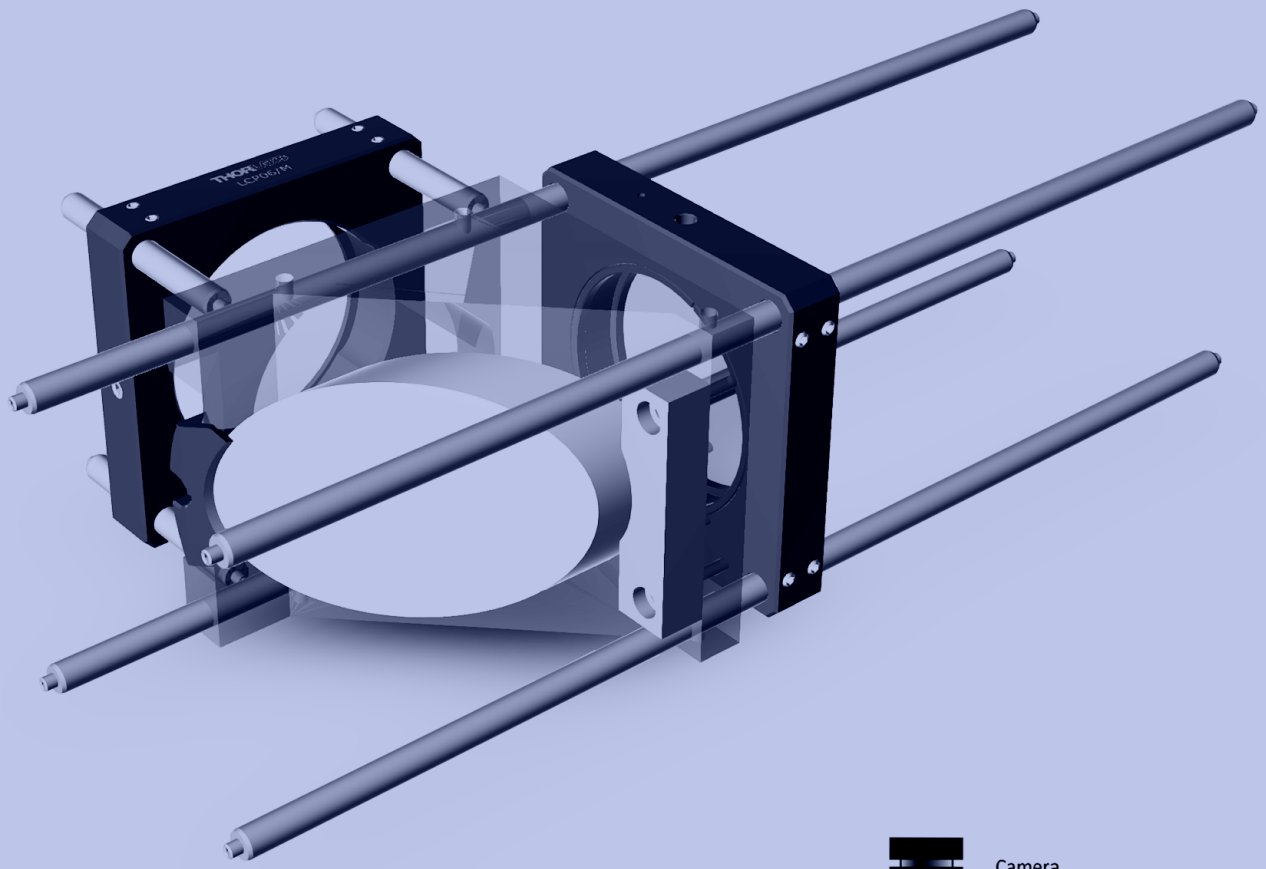

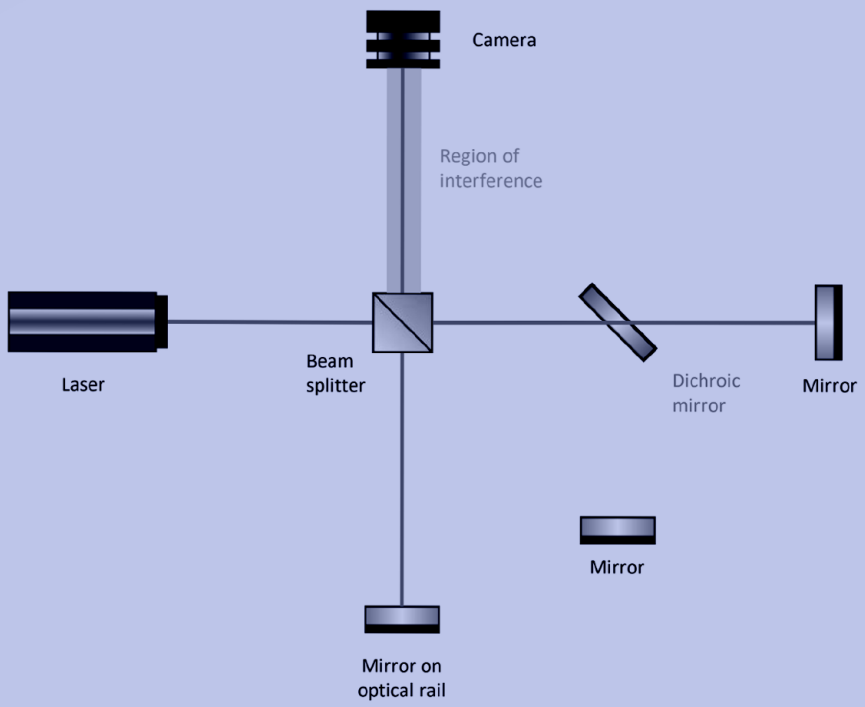

C

Characterising the wavefront distortion in dichroic mirrors

9 Theory of dichroic mirrors

Introduction

After the possibility of isolating a two-state system in dysprosium was shown in subsection 8.4, questions of an implementation in the experiment naturally arise. It is advisable to superimpose the additional Stark shift laser with another laser, since there is only limited optical access to the atomic cloud. For this purpose, dichroic mirrors can be used, which are explained in subsection 9.1. The principle of these mirrors is based on a surface coating, which can, however, be deformed by external factors like the mirror holder. This deformation can affect the wavefront of the laser light, which is explained in subsection 9.2. To minimise the influence of external stress on the dichroic mirror, a holder is designed in subsection 9.3 which has as few contact points with the mirror surface as possible. In addition, the influence of the self-weight of two dichroic mirrors of different thicknesses in the holder is investigated in simulations with regard to stress and deformation. Finally, an optical setup which allows the distortion from the wavefront to be quantified is presented in subsection 9.4.

9.1 Structure and physical principle

Dichroic mirrors have significantly different reflection and transmission properties in two different wavelength regimes. The experimentally relevant wavelengths of these regimes will be defined as λ_T for the transmitted one and λ_R for the reflected one. Dichroic mirrors can have a broad or narrow wavelength regime, with a broad band being used for example to reflect thermal infrared waves, while letting visual light pass and a narrow band being mostly used for laser applications, see e.g. [SSJ82].

In the experiment, dichroic mirrors are used to merge two different laser beams. This allows for example to inject an additional laser causing an AC Stark shift superimposed to the vertical imaging beam. In comparison to electronics, where high- and low-pass filters exist, in optics short- and long-pass mirrors are defined, with the terms short and long referring to the light frequency. A short-pass

mirror has a high transmittance at short wavelengths and a high reflectivity for long wavelengths while for a long-pass mirror this relation is reversed.

In general the operational principle of a dichroic mirror is given by a multi-layer interference coating. For the coating itself semiconductor or mono-crystalline materials are used. Depending on the coating materials the mirrors are characterised to be a dielectric or crystalline mirror, with dielectric mirrors being more common[10].

For the transmitting wavelength possible reflections from the mirror back-side have to be taken into consideration which are reduced by additional back side coating.

9.2 Wavefront distortion

Since optics can not be polished perfectly flat and also coatings can not be applied with a perfect accuracy, the surface of optics can distort a wavefront. Dichroic mirrors are usually manufactured by layer deposition onto a substrate. Internal and external stress onto this surface can deform the mirror coating and cause such distortions.

The two most common methods to quantify the flatness of a surface are the root mean square (RMS) of the surface and the Peak to Valley (PV) value. When choosing a method one has to consider if the surface imperfections are of a global or a local nature. The RMS is a good measurement if local imperfections dominate, however in the case of dichroic mirrors, a spherical curvature tends to dominate the distortion. In order to obtain a reliable picture of the surface topology, both the RMS value and the radius of curvature of the dichroic mirror will be presented below. The radius of curvature R is related to the PV value δ of the beam cross section on the mirror by [LLC18]

$$\delta = \frac{D^2}{8R} \tag{9.85}$$

with the optical beam diameter D. For a small beam diameter, the global curvature of the mirror can be neglected and local, structural artefacts tend to dominate. In the experimental setup two different dichroic mirrors will be used with a material thickness of $5\,\mathrm{mm}$ and $12\,\mathrm{mm}$. The same mounting of the mirrors is used, so similar external stress is applied to both mirror types. However it is expected that the thin mirror distorts the wavefront more than the thick one since it has less support material.

When reflecting a planar wave from a curved mirror, the wavefront will also obtain a curvature and a focal length of the mirror can be defined. To quantify the distortion of the wavefront due to a curvature of the mirror the Reflected Wavefront Error (RWE) can be defined as [LLC18]

$$E_{\mathsf{RWE}} = 2\delta\,\cos(\theta) \tag{9.86}$$

with a flatness δ and a reflection angle θ of the incoming light from the orthogonal surface vector in the center of the mirror. When implementing a dichroic into other optics, this error can influence the positions and shapes of focal points. Therefore it is crucial to minimise these effects and characterize the dichroic mirrors within their mount.

[10] These are fabricated by electron beam deposition, ion beam sputtering or ion-assisted deposition [Bau04]. For the calculation of the required layers, often does not exist an analytical approach and numerical Monte Carlo simulations are commonly used.

9.3 Dichroic holder and distortion simulation

As mentioned in the previous subsection, external stress on the mirror coating can cause a deformation in the reflected wavefront. To reduce this stress, a special mounting has been designed by Dr. Shuwei Jin from my working group. In the mount the dichroic lies on a flat surface with a elliptical cutout. The position is fixed by four contact points, where only two touch the mirror surface.

The mount is shown in figure 33. It is able to fixate mirrors with varying thicknesses from a few millimeters up to 12 mm. The only part that changes is the top clamp [I]. The bottom connector, labeled as [III] has two contact points with the side of the mirror and prevents the mirror from shifting on the contact surface with the main holder, labeled as [II].

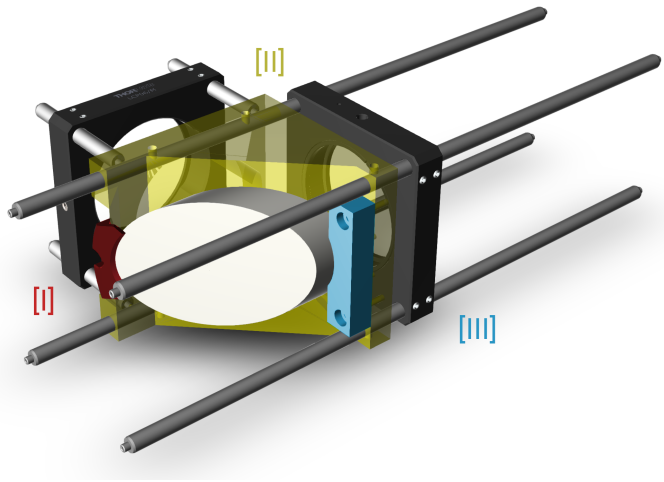

Figure 33: Three-part construction of the holder for the dichroic mirror. [II] represents the main piece on which the dichroic mirror is mounted, [III] fixes the mirror at two side points and [I] provides the only contact to the mirror surface.

A curvature of the mirror coating can be caused by gravitation, the mounting or by imperfection in the manufacturing process. To quantify the gravitational deformation of the mirror, an analysis of the stress and deformation of the materials was carried out in Autodesk Inventor. The material of the holder is aluminium due to its low weight and high material strength. The clamping piece [I], is 3D printed due to its high complexity and thus consists of polylactides (PLA). For the simulations, a density of $\rho = 2.7 \cdot 10^{-6}\text{kg mm}^{-3}$ and a Young's Modulus of $E = 68.9\,\text{GPa}$ was used for aluminium, a density of $\rho = 1.541 \cdot 10^{-6}\text{kg mm}^{-3}$ and a Young's Modulus of $E = 2.758\,\text{GPa}$ for PLA and finally a density of $\rho = 2.18 \cdot 10^{-6}\text{kg mm}^{-3}$ and a Young's Modulus of $E = 68\,\text{GPa}$ for the dichroic mirror. These are standard literature values for aluminium, polyethylene terephthalate (PET) and glass, whereby PET and glass are assumed to sufficiently approximate the actual material properties of PLA and the dichroic mirror for an initial estimate of the deformation. The result of the simulation for the $12\,\text{mm}$ thick mirror is shown in figure 34 and the result for the $5\,\text{mm}$ thick mirror is shown in figure 35.

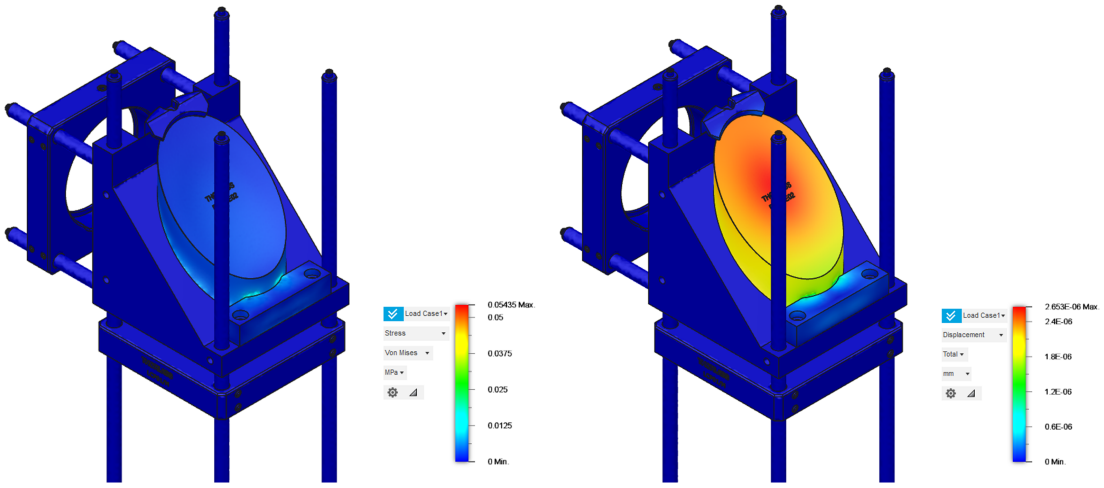

Figure 34: Stress analysis (left) and displacement analysis (right) of the $12\,\mathrm{mm}$ thick dichroic mirror. For this analysis, the position of the mount itself was fixed while a gravitational force ($F = 0.76\,\mathrm{N}$) was applied to the mirror itself. The stress is given in units of MPa (linear scale from $0\,\mathrm{MPa}$ to the maximal value of $0.05435\,\mathrm{MPa}$) and the displacement is given in units of mm (linear scale from $0\,\mathrm{mm}$ to the maximal value of $2.653 \cdot 10^{-6}\,\mathrm{mm}$). The spatially distributed values of stress and displacement are colour coded.

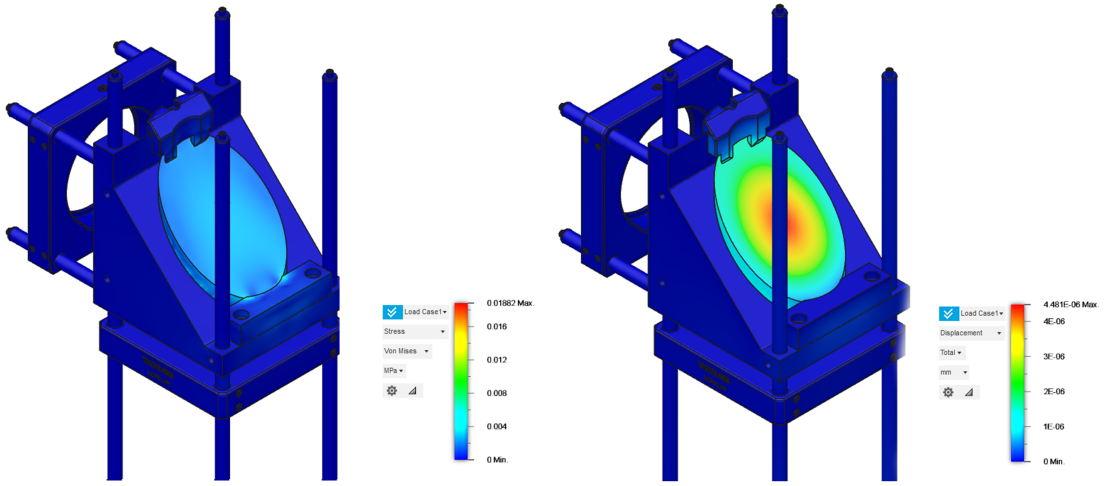

Figure 35: Stress analysis (left) and displacement analysis (right) of the $5\,\mathrm{mm}$ thick dichroic mirror. For this analysis, the position of the mount itself was fixed while a gravitational force ($F = 0.33\,\mathrm{N}$) was applied to the mirror itself. The stress is given in units of MPa (linear scale from $0\,\mathrm{MPa}$ to the maximal value of $0.01882\,\mathrm{MPa}$) and the displacement is given in units of mm (linear scale from $0\,\mathrm{mm}$ to the maximal value of $4.481 \cdot 10^{-6}\,\mathrm{mm}$). The spatially distributed values of stress and displacement are colour coded.

For the $12\,\mathrm{mm}$ thick dichroic, the maximal stress is given as $\sim 0.054\,\mathrm{MPa}$ and the maximal displacement is given as $\sim 2.65\,\mathrm{nm}$. In contrast the $5\,\mathrm{mm}$ thick dichroic has a lower maximal stress of $\sim 0.018\,\mathrm{MPa}$ while bending more with a maximal distortion of $\sim 4.48\,\mathrm{nm}$. In the simulations, only the weight of the mirrors was taken into account and not the contact pressure of the mount. The distortions are in the range of a few nm, while the wavelengths relevant for the experiment are in the $\lambda \sim 100\,\mathrm{nm}$ regime. Therefore their influence on the wavefront can be neglected, as for an

interference pattern, a wavelength shift of at least $\sim \lambda/2$ is necessary. It remains to investigate the influence of the mount or manufacturing issues on the dichroic mirror coating.

9.4 Development of an optical measurement setup for the wavefront distortion of dichroic mirrors

To characterise the wavefront, interferometric measurements have proven to be a valid approach [Wal20]. Despite a lot of various interferometer types, the basic principle is always the same. The core element is a beam splitter (BS), which splits an incoming wave into two spatial directions of equal intensity. Both beams are reflected and recombine again after the BS which causes interference. In the plane wave approximation, the two interfering waves can be represented as rotation in the complex plane:

$$\begin{aligned} \psi_1(z) &= \sqrt{I_0}\ \exp(-ikz) \\ \psi_2(z,d) &= \sqrt{I_0}\ \exp(-ik\,(z-d)) \end{aligned} \tag{9.87}$$

Here I_0 is the intensity of the light after the BS, $k = \frac{2\pi}{\lambda}$ is the wave vector, z is the propagation axis along the optical path after the BS and d is the optical path length difference of the interferometer. The intensity distribution as a function of the path length difference is

$$\begin{aligned} I(d) &= |\psi_1(z) + \psi_2(z,d)|^2 \\ &= I_0\ |1 + \exp(ikd)|^2 \\ &= 2I_0\ \left(1 + \cos\left(\frac{2\pi d}{\lambda}\right)\right). \end{aligned} \tag{9.88}$$

Thus, the intensity $I(d)$ has exactly the periodicity of the wavelength. Since this is usually in the nanometer range, interferometric setups are very sensitive to environmental vibrations. For the measurements the interferometer is set up on an optical table and data acquisition is carried out at nighttime. For the wavefront characterisation of the dichroic mirror, a Michelson interferometer was chosen because of its simple construction. The dichroic mirror is to be characterised for two different wavelengths and therefore two different beam paths are present in the interferometer. The exact optical setup using a non polarising beam splitter (NPBS) is shown in figure 36.

The present measurement setup allows to measure the influence of a wavefront distortion for both wavelengths without any modification of the setup. Two lasers with wavelengths $\lambda = 405\,\mathrm{nm}$ and $\lambda = 635\,\mathrm{nm}$ act as light source, as these are expected to sufficiently approximate the properties of the lasers used in the experiment. For the measurements, additional beam preparation was necessary, that is not shown in figure 37

To increase the beam diameter, a telescope consisting of two concave lenses with a focal length $f = -60\,\mathrm{mm}$ and a convex lens with a focal length of $f = 300\,\mathrm{mm}$ were used. With the program GaussianBeam [Gau08], an optimal configuration of the lenses was determined, which provided a parallel beam whose size fills the entire 1” beam splitter. The final telescope configuration is shown in figure 37.

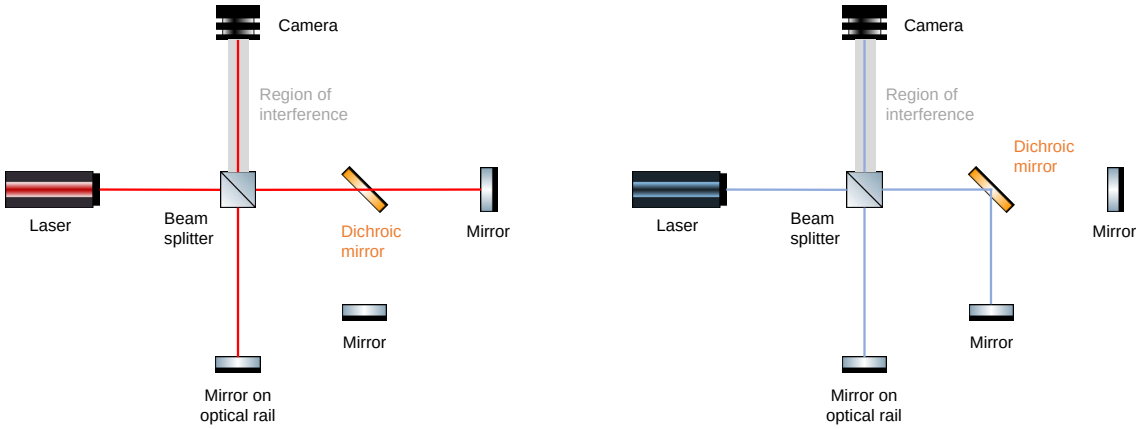

Figure 36: Setup of the Michelson interferometer to characterise the wavefront of the dichroic mirrors. On the left the optical path of a laser with wavelength $\lambda = 626\,\mathrm{nm}$ is shown, which can pass the dichroic mirror. On the right the optical path of a laser with wavelength $\lambda = 421\,\mathrm{nm}$ is shown, which is reflected by the dichroic mirror. This plot was made with an optics component library [Fra09].

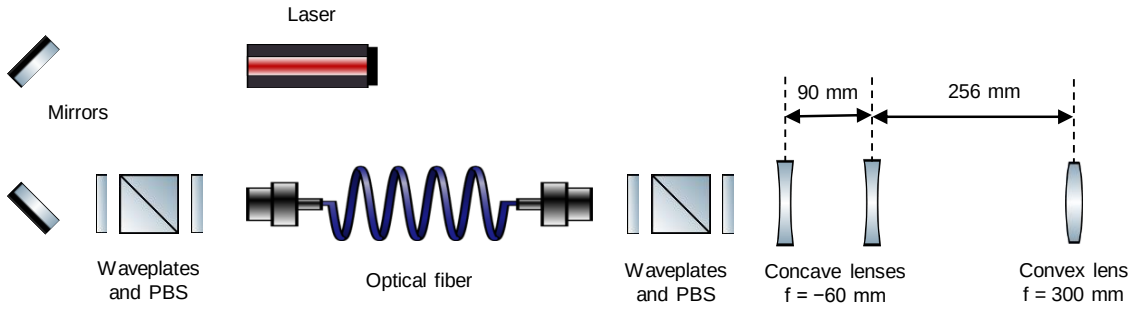

Figure 37: Optical telescope for polarisation cleaning of the laser light and enlargement of the beam diameter. The beam was magnified by two concave lenses with a focal length of $f = -60\,\mathrm{mm}$ and one convex lens with a focal length of $f = 300\,\mathrm{mm}$.

The lasers were polarised before the coupling into a polarisation maintaining fiber, using a polarising beam splitter (PBS) and two $\lambda/2$ wave plates. Following the fiber, the polarisation was cleaned again. This type of coupling increased the fiber coupling efficiency and minimised intensity fluctuations caused by the fiber. For imaging, a second convex lens with $f = 100\,\mathrm{mm}$ was used, to map the interference pattern onto the camera sensor. Care was taken to ensure that the interference image completely filled the vertical extent of the sensor.

Conclusion

To integrate an AC Stark laser into the experimental setup, it is advisable to superimpose it with another laser using dichroic mirrors. For some applications in the experiment, the preservation of the wavefront is of particular interest, which is why in this subsection, after a brief explanation of the functional principle, a mount for the mirrors is presented which minimises the contact points with the mirror coating in order to prevent possible bending. An optical setup was developed whose basic principle is based on the Michelson interferometer and that is capable of quantifying the wavefront distortion.

In the next subsection, measurements are made of two dichroic mirrors of different thicknesses and their respective reflecting and transmitting wavelengths. The interference pattern can be used to determine the maximal laser beam size that is not affected by the dichroic mirrors.

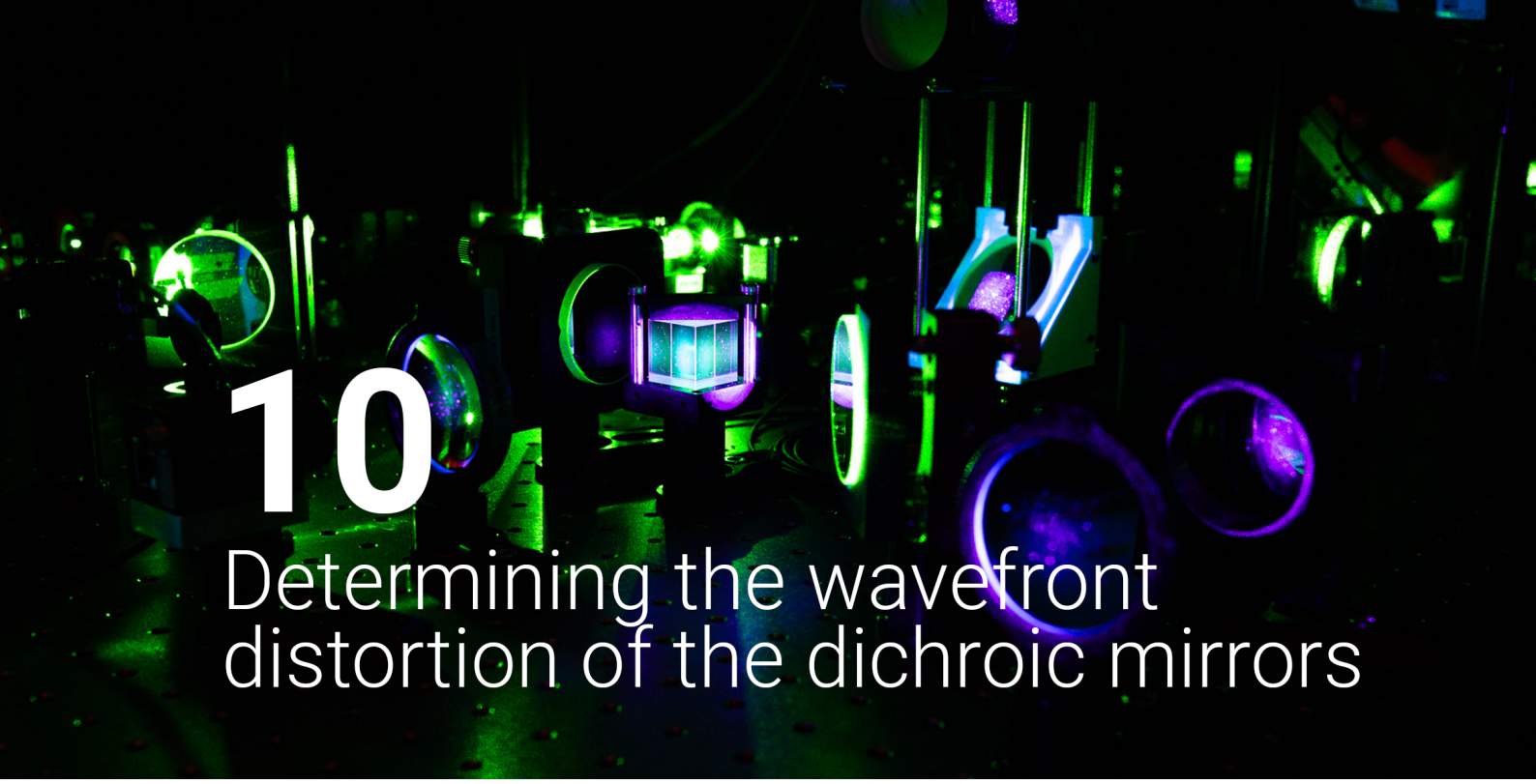

10 Determining the wavefront distortion of the dichroic mirrors

Introduction

In this section, two different dichroic mirrors are examined for their reflecting and transmitting wavelengths respectively. In subsection 10.1, the imaging procedure and the analysis method are first presented which is exemplary shown for the $5\,\mathrm{mm}$ thick dichroic mirror and its reflecting wavelength at $\lambda = 405\,\mathrm{nm}$ in subsection 10.2. For this special case it is possible to generate a phase map by means of a fit function, which shows the effective curvature of the mirror. The following subsections 10.3, 10.4 and 10.5 cover the remaining mirror wavelength combinations, where the size of the central interference peak is used as a measure of the quality of the wavefront.

10.1 Image analysis and fit function

Since fluctuations on a $\sim 100\,\mathrm{nm}$ scale can strongly influence the measurements, the experimental setup is very sensitive to vibration. Although the setup was build on an optical table and measurements have been recorded at nighttime, the fluctuations remained being visible, and the interference pattern of the dichroic shifted periodically. Since the interference center peak fills a large amount of the sensor, this phase shift caused fluctuations in the averaged intensity. This phenomenon is exemplary plotted in figure 38 for the $\lambda = 405\,\mathrm{nm}$ laser.

In order to obtain meaningful results, an image processing procedure was developed. For this an image series of the interferometer without any dichroic was taken, besides the image series with dichroic[11]. Both image series consisted of 250 images with an exposure time of $50\,\mu\mathrm{s}$ and were averaged to one final image each[12]. The image without dichroic is shown in figure 39 and will be

[11] To take care of damaged pixels on the camera sensor, an image series of 250 dark images has been recorded and averaged. This averaged master dark image was then subtracted from all images.

[12] Due to the vibrational phase shift in the interference pattern, only the images with constructive center interference have been averaged in the image series of the setup configuration with dichroic.

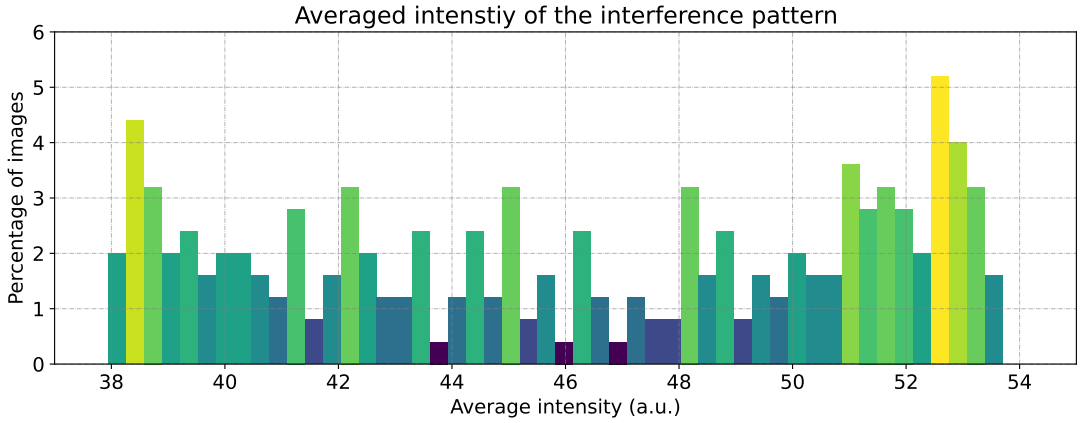

Figure 38: Histogram of the average intensities of the interference image. On the x axis, the intensities are plotted in arbitrary units with $I \in [0, 256]$. The y axis indicates the percentage with which the corresponding image intensity occurred in a data set of 250 images. The intensity fluctuations are in a range of $\delta I = 15$.

referred to as „correction image“ in the following.

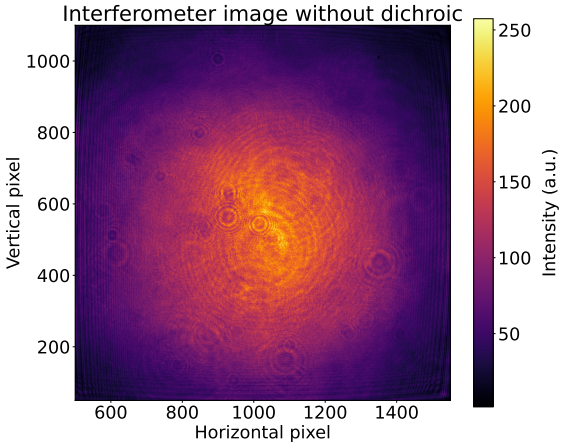

Figure 39: Image of the Michelson interferometer without any dichroic. On the x and y axis the pixels of the camera sensor are shown. Here only the relevant part of the camera sensor is displayed since the beam splitter limits the size of the interference pattern to exactly 1” in both directions. The intensity I is colour-coded in a.u. with $I \in [0, 256]$.

This image only considers the influence of the optical setup components and does not show any interference. Therefore it proves that an eventually detected interference in the measurements is caused by the dichroic and not by other optical components. This correction image will be used to correct the Gaussian intensity profile of the laser beam in the interference pattern (which is still preserved after the magnification using the telescope in figure 37). For this the averaged interference image was divided by the correction image[13] and the intensity is normalised to $I \in [-1, 1]$. The obtained image will be referred to as „corrected interference image“ in the following, while the interference image before division and normalisation will be referred to as „averaged interference image“. This procedure of image processing is of crucial importance, especially to analyse the low-intensity higher diffraction orders.

[13]Division showed significantly better results than subtraction, which was also investigated as a method for image processing.

To examine the interference pattern more closely, a two-dimensional fit function $I(x, y)$ is defined as

$$I(x, y) = N \cos\left(D\,(x^2 + \epsilon^2 y^2)^2 - \phi\right) \qquad \text{with } [N, D, \epsilon, \phi] \text{ as fit parameter.} \tag{10.89}$$

where N gives the amplitude of the intensity, D can be interpreted as curvature parameter, ϕ is an offset phase of the interference pattern, and ϵ describes the elongation of the interference pattern in one spatial direction. The case of $\epsilon = 1$ represents the interference pattern that occurs in a plane away from the focal point when parallel light is focused through a lens. As mentioned in subsection 9.2, a focal length can also be defined for a dichroic mirror if the coating bends to the shape of a curved mirror. Also here the interference pattern is recorded off the focal point in the experiment. The associated phase function $P(x, y)$ is given as the argument of the cosine as

$$P(x, y) = D\,(x^2 + \epsilon^2 y^2)^2 - \phi. \tag{10.90}$$

10.2 5 mm mirror characterisation with a 405 nm laser

First, the $5\,\mathrm{mm}$ thick dichroic mirror is investigated for a wavelength of $\lambda = 405\,\mathrm{nm}$. The image acquisition is carried out as described in subsection 10.1. For comparison, the averaged interference image before the correction is shown in figure 40 on the left.

At this point, an elongated diffraction pattern is already recognisable, with at least 3 diffraction orders next to the central maximum. Now the interference image in figure 40 on the left is processed as described in subsection 10.1. The result is shown in figure 40 on the right.

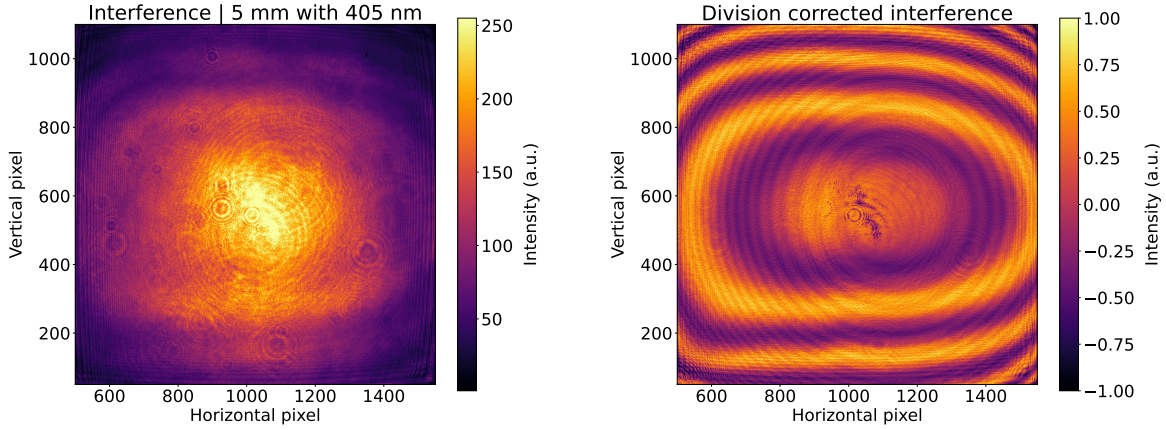

Figure 40: Averaged interference image (left) and division corrected and normalised interference image (right) of the $5\,\mathrm{mm}$ thick dichroic for a $405\,\mathrm{nm}$ laser. Here only the relevant part of the camera sensor is shown since the beam splitter limits the size of the interference pattern to exactly 1”. The intensity I is colour-coded and given in arbitrary units.

Due to the correction by the Gaussian intensity profile, the higher order interference rings become normalised to the same intensity as the center interference peak. When looking at the 3D plot and the two cross-sections in horizontal and vertical direction in figure 41, one notices that the interference pattern is very noisy.

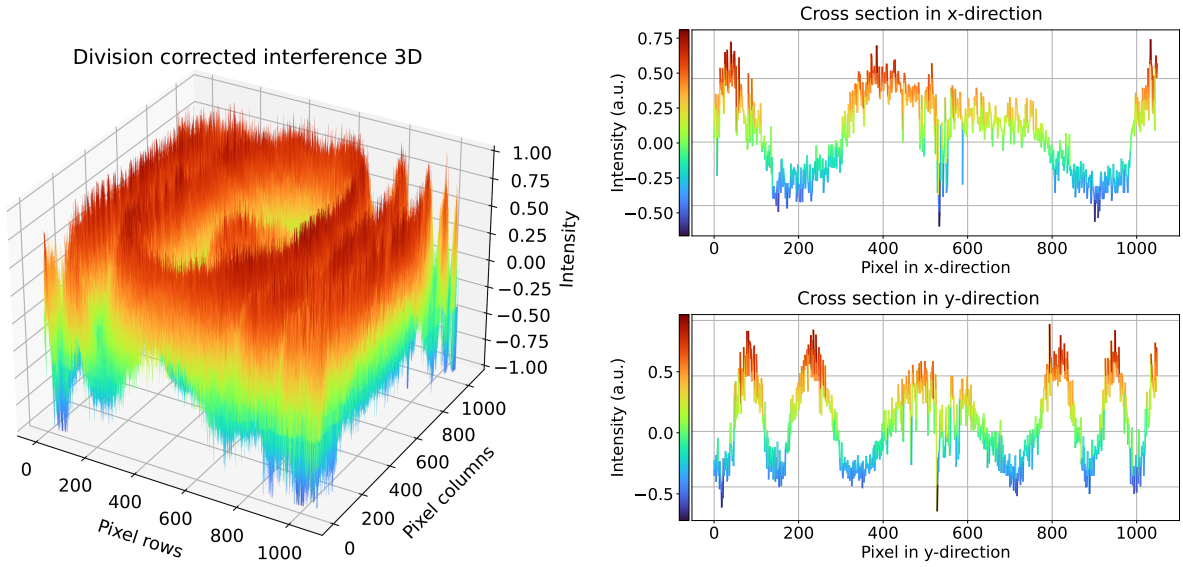

Figure 41: A three-dimensional plot of the division corrected interference of the $\lambda = 405\,\mathrm{nm}$ laser and the $5\,\mathrm{mm}$ thick dichroic is shown on the left. The normalised intensity is plotted on the z-axis and additionally colour-coded. The x and y axes again represent the position on the camera sensor. The cross-sections in both axes of the camera sensor are shown on the right. On the x axis the pixels are plotted in the respective spatial direction of the camera sensor, whereas on the y axis the intensities are plotted. In analogy to the 3D plot on the left, the graphs are also colour-coded.

To analyse the interference pattern, a two-dimensional fit is made to the data in figure 42. The fit function defined in equation (10.89) is used, whereby the first estimates for suitable fit parameters can be taken from figure 40.

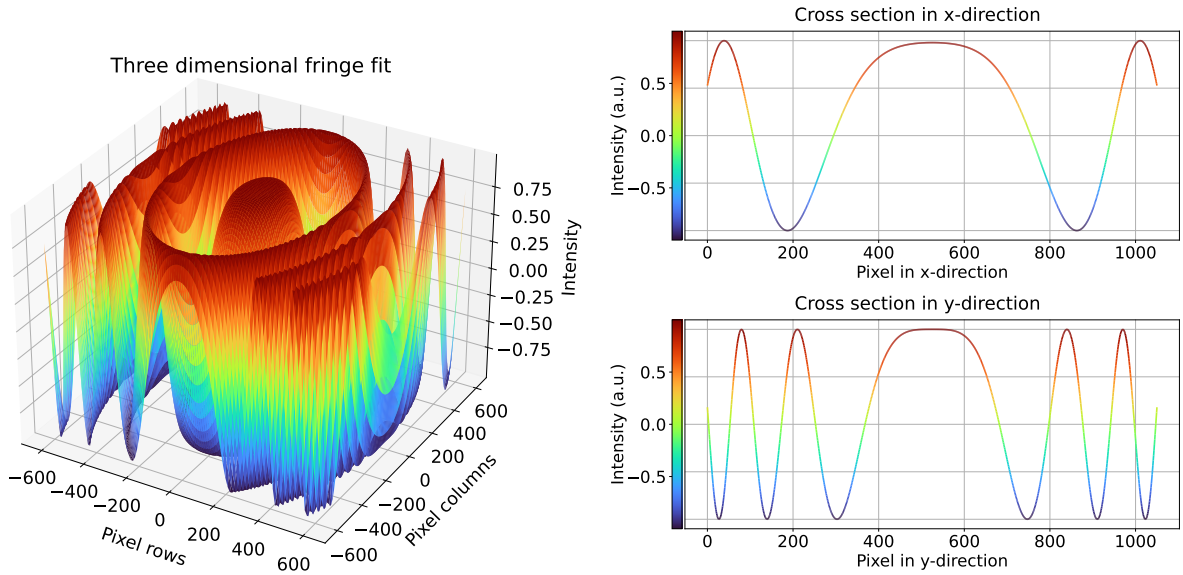

Figure 42: A three-dimensional fit using equation (10.89) as fit function is shown on the left. As in figure 41, which was used as fit data, the relative intensity is colour-coded while x and y represent position on the sensor. The corresponding cross sections in the x and y direction are shown on the right.

From the fit, an elongation of $\epsilon = 0.6377 \pm 0.00014$ can be obtained. Intuitively, this would speak for an elliptical curvature of the mirror coating. It can be seen that in the vertical y direction, several

diffraction patterns can be recognised, so the curvature appears to be stronger here. However, it must be taken into account that the light hits the dichroic at an angle of $45°$. Accordingly, a larger range by a factor of $\sqrt{2}$ is covered in the vertical direction. With a perfectly circular curvature, an elongated interference pattern with the same orientation as in figure 40 can therefore be expected in the measurements, with an elongation of $\epsilon \approx 0.7071$. Since the dichroic mirror is fixed in the vertical direction and more stress acts in this direction, as shown in figure 35, an increased curvature in the vertical direction cannot be excluded but if this effect is present, it only accounts for a small part of the elongation. The size of the recorded interference pattern is limited by the size of the 1" NPBS, so the side length is $2.54\,\mathrm{cm}$. The constriction of the central peak can be estimated with a diameter of $d \approx 5\,\mathrm{mm}$. In this region, the laser does not experience a relevant distortion of the wavefront, so in general small laser beam waists that are aligned to the center of the dichroic should not be affected. The fringe fit parameters can be used in equation (10.90) to obtain an effective phase map of the mirror, which is shown in figure 43.

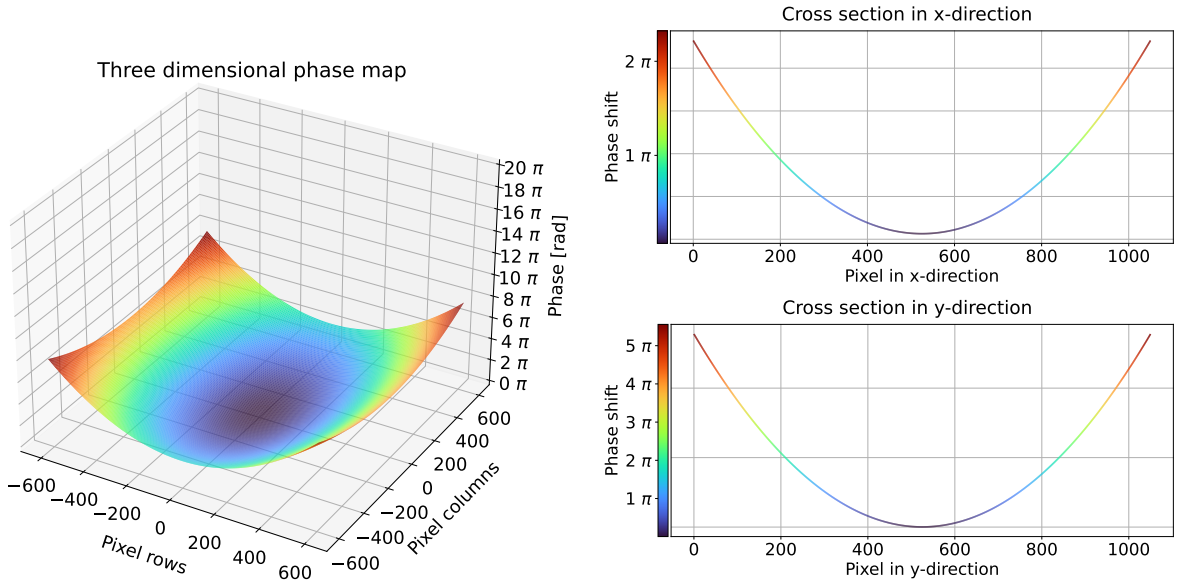

Figure 43: Phase map showing the effective curvature of the dichroic mirror coating (left) with the corresponding cross sections. Here the phase in radiant is plotted against the position on the sensor. It must be noted that the beam is radiated in an angle onto the mirror. This accounts to most of the ellipticity of the phase map.

The curvature parameter D in the fringe and phase fit functions in equation (10.89) and equation (10.90) is given as $D = (1.502 \pm 0.005) \cdot 10^{-5}\,\mathrm{px}^{-4} \approx (12,74 \pm 0.04) \cdot 10^{3}\,\mathrm{mm}^{-4}$. In the last equation it was used that the side length of one camera pixel is given as $1\,\mathrm{px} = 5.86\,\mu\mathrm{m}$ [All23] [Son15]. Since the intensity was normalised, the fit parameter N is expected to be 1. However, since for the normalisation the maximal and minimal intensity have been used, the amplitude is a little bit lower and given as $N = (0.9002 \pm 0.0009)$. The phase offset ϕ is also expected to be low, since the images used for the averaged interference image were selected to have a constructive interference center peak. From the fit the phase offset was determined as $\phi = (2.4446 \pm 0.0003) \cdot 10^{-5}$, which is very close to the expectation, however a small phase offset is still possible due to an imperfection in the selection method of the images.

10.3 5 mm mirror characterisation with a 635 nm laser

Now the $5\,\mathrm{mm}$ dichroic is examined for its transmitted wavelength with a $\lambda = 635\,\mathrm{nm}$ laser. The recording and analysis of the interference images is identical to subsection 10.2. The division corrected interference image is shown as a 2D plot in figure 44 together with two cross sections in the x and y direction.

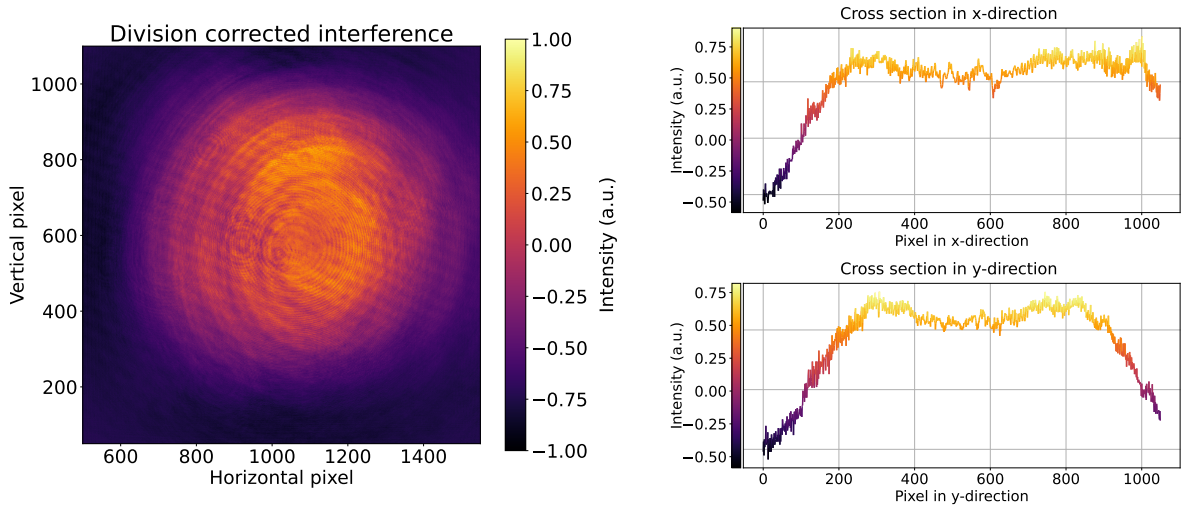

Figure 44: Two-dimensional plot of the division corrected interference of the $\lambda = 635\,\mathrm{nm}$ laser and the $5\,\mathrm{mm}$ thick dichroic on the left. The normalised intensity is colour-coded while the x and y axes represent the position on the camera sensor. Cross-sections in both axes of the camera sensor are plotted on the right. The x axis represents the respective spatial direction of the camera sensor whereas the y axis represents the normalised intensity. In analogy to the 2D plot on the left, the graphs are colour-coded.

In this case only the central interference peak is visible. The plots of the cross sections show that destructive interference already has a small influence in the center due to slight dips. This indicates an additional phase shift $\phi \neq 0$ in equation (10.89). If ϕ were set to zero, the dip would disappear and the extent of the central peak would be slightly reduced. Nevertheless, it can already be deduced from figure 44 that the wave front for the wavelength $\lambda = 635\,\mathrm{nm}$ is obtained on a significantly larger area than was the case for $\lambda = 405\,\mathrm{nm}$. This can be explained by the fact that in this case the laser light is not reflected but transmitted. If there is a curvature of the coating, this only influences the refraction of the laser light at the transition between the media air and glass and the coating relief is not directly transferred to the wavefront. In this configuration a complete wavefront conservation can be expected for a beam diameter of $d \approx 14.8\,\mathrm{mm}$. Since in this case only the central peak is visible and none of the interference rings was visible, a meaningful fit is not possible in this case and the curvature parameter cannot be determined reasonably with this method.

10.4 12 mm mirror characterisation with a 405 nm laser

Now the $12\,\mathrm{mm}$ dichroic for the wavelength $\lambda = 405\,\mathrm{nm}$ is examined. In the investigated area, which is limited by the 1” cube, no clear interference pattern results, which is shown in figure 45.

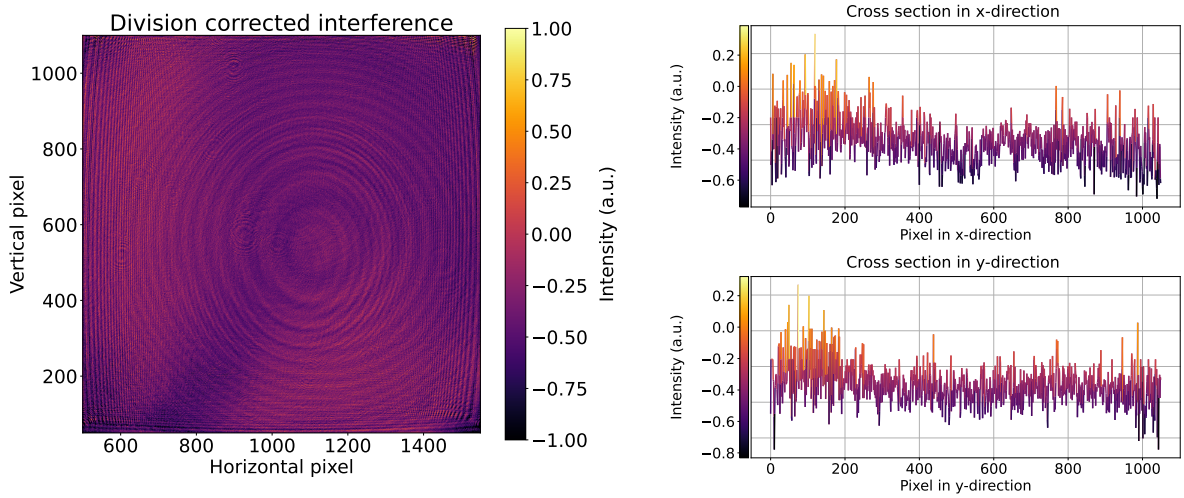

Figure 45: Two-dimensional plot of the division corrected interference of the $\lambda = 405\,\mathrm{nm}$ laser and the $12\,\mathrm{mm}$ thick dichroic on the left. The normalised intensity is colour-coded and plotted over the area of the x and y axes that represent the position on the camera sensor. The corresponding cross-sections in both axes of the camera sensor are plotted on the right. The x axis represents the respective spatial direction of the camera sensor whereas the y axis represents the normalised intensity. In analogy to the 2D plot on the left, the graphs are colour-coded.

This behaviour indicates that the central peak of constructive interference fills the entire sensor area. Thus, the $12\,\mathrm{mm}$ dichroic would preserve the wavefront of beams with a waist of $25.4\,\mathrm{mm}$, i.e. a beam diameter about 5 times larger than the $5\,\mathrm{mm}$ dichroic. One explanation is that the surface coating bending is expected to be significantly lower due to the presence of more support material.

10.5 12 mm mirror characterisation with a 635 nm laser

Finally, the $12\,\mathrm{mm}$ dichroic for the wavelength $\lambda = 635\,\mathrm{nm}$ is investigated. In this case an interference pattern is visible, which is shown in figure 46.

In comparison to all other measurements, the obtained interference image is asymmetric. An intrinsically asymmetric interference behaviour caused by the mount can be excluded due to the symmetry of the mirror and the mount in the horizontal direction. However, possible causes can be an asymmetric error in the manufacturing process or imperfect alignment of the optical setup.

Since a higher flatness of the mirror coating was proven in subsection 10.4 for the $12\,\mathrm{mm}$ dichroic, it is assumed that the cause of the interference could be different than surface bending. In particular, it is noticeable that compared to the $5\,\mathrm{mm}$ dichroic, a first additional interference ring is seen, so that the wavefront distortion increases despite more support material. A possible explanation here is the refraction of light and interference between the two mirror surfaces, which could have a greater influence in the case of the $12\,\mathrm{mm}$ dichroic. Using this dichroic a complete wavefront conservation can be expected for a beam diameter of $d \approx 10.6\,\mathrm{mm}$. This is 0.72 times the preserved beam diameter of the $5\,\mathrm{mm}$ dichroic. Therefore regarding wavefront conservation, one gets much smaller differences in the transmitting case than in the reflecting case between both dichroic thicknesses.

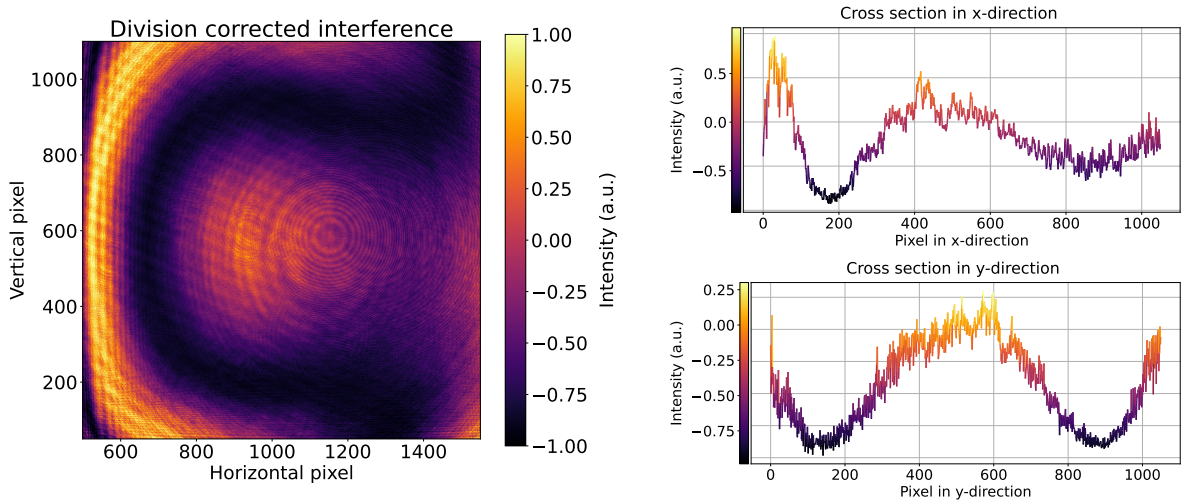

Figure 46: Two-dimensional plot of the division corrected interference of the $\lambda = 635\,\text{nm}$ laser and the $12\,\text{mm}$ thick dichroic on the left. The normalised intensity is colour-coded and plotted over the relevant sensor area. The x and y axes represent the position on the camera sensor. Cross-sections in both axes of the camera sensor are shown on the right side. The x axis represents the respective spatial direction of the camera sensor whereas the y axis represents the normalised intensity. In analogy to the 2D plot on the left, the graphs are colour-coded.

Conclusion

After the development of the measurement setup, this subsection now concentrates on the methods of image acquisition and analysis. Two different dichroic mirrors with thicknesses of $5\,\text{mm}$ and $12\,\text{mm}$ are examined for their transmitted ($\lambda = 635\,\text{nm}$) and reflected ($\lambda = 405\,\text{nm}$) wavelengths. In the case of reflection, the thin dichroic mirror has a stronger coating bending, since three interference rings were measured in addition to the central peak. In comparison, the central interference peak of the thick dichroic mirror occupied the entire sensor surface, so the coherent wavefront could be maintained over a significantly larger area.

In the case of transmission, the thin dichroic proved to have better properties, as only the central interference peak is visible here, instead of an additional interference ring as in the case of the thick dichroic. Through the reflection measurements and the physical consideration that a greater thickness also means more support material that can prevent bending, it has been proven that the thin dichroic has a greater curvature. Therefore, the cause of the interference is localised primarily within the mirror, since both mirror surfaces are passed during transmission, and an interference area can occur between them.

Compared to the transmission measurements, an elongation of the interference pattern occurred in the reflection measurements. This could be determined by a fringe fit to be $\epsilon = 0.6377 \pm 0.00014$. By estimation, it was concluded that this elongation occurs in particular due to the angle of $45°$ between the laser beam and the dichroic, however, a small part could be caused by the clamping in the mount itself.

Overall, it was found that the beam diameters with full wavefront conservation range from $\sim 5\,\text{mm}$ (for the $5\,\text{mm}$ dichroic and $\lambda = 405\,\text{nm}$) to $> 25.4\,\text{mm}$ (for the $12\,\text{mm}$ dichroic and $\lambda = 405\,\text{nm}$).

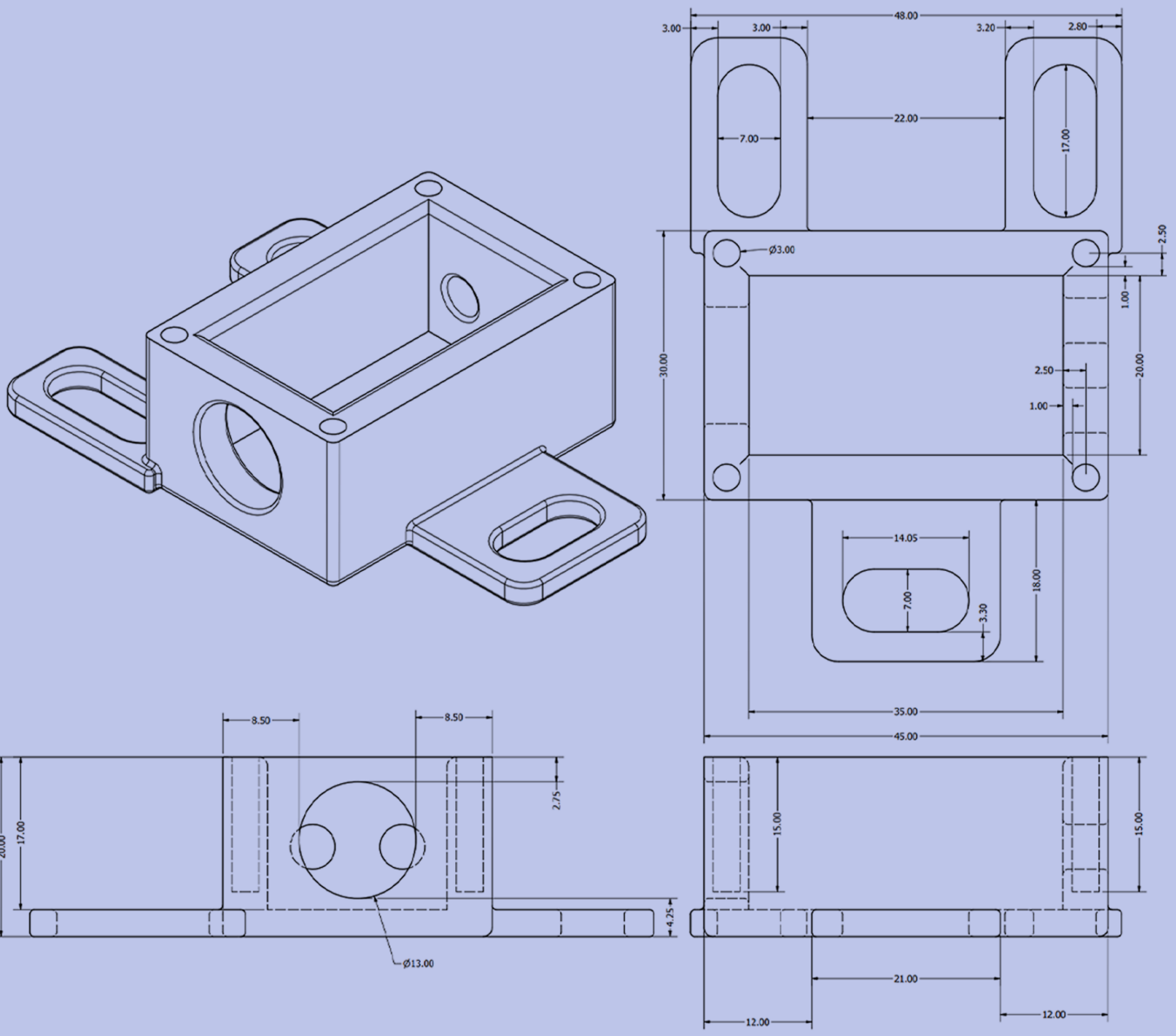

D

Outlook and Appendix

11 Conclusion and Outlook

11.1 Radio frequency spectroscopy and magnetic field characterisation

The main objective of part A was to develop a radio frequency setup and implement it into the experiment to characterise the magnetic field coils of the experimental chamber. For this purpose, the theoretical basics of radio frequency spectroscopy were dealt with. A general Hamiltonian was derived, which is able to describe n state systems. Using this, the occupation probabilities of the sublevels in the dysprosium 17 state system were simulated, which allowed to determine the Rabi frequency of the system. Subsequently, the optimal geometry of an RF coil was derived on the basis of the geometric constraints of the experiment and considerations from high-frequency electronics. The RF coil was implemented in modular form in the experiment and its magnetic field strength could be estimated. This allowed to calibrate the magnetic field coils in all spatial directions and opened the possibility to perform transformations of the magnetic field.

In summary RF spectroscopy offers a simple method of determining the strength of the magnetic field at the position of the atoms without having to break the vacuum of the experimental chamber or interfere with the experiment in any other way. The work of this thesis could be taken further insofar as different non-circular coil geometries and the influence of the coil material on the Rabi oscillations could be investigated. Furthermore, simulations regarding the radiation behaviour of the RF coil and the influence of the metallic surroundings on the magnetic field strength could be carried out.

11.2 Spin preparation in dysprosium using Rabi oscillations

Part B aimed to drive measurable Rabi oscillations in dysprosium which have been covered in the theory of part A to prepare specific spin states. The cause of the lack of measurability, the dipolar relaxation, was treated theoretically and an analytical solution for atom number and temperature was obtained. From this, the time scale of this loss process could be determined and compared with the Rabi time. It turned out that the atomic number was significantly reduced before the first

revival, so during the measurements the signal was lost in the background noise. Subsequently, two approaches were presented to drive Rabi oscillations. The first is to increase the RF field strength and thus reduce the Rabi time by means of an impedance matching circuit of the RF coil. The second is to isolate a two-state system of $|-8\rangle$ and $|-7\rangle$ using the nonlinear AC Stark effect of σ_- polarised light with a wavelength of $\lambda = 657.937\,\mathrm{nm}$. From theoretical considerations, both methods have proven to be valid approaches to prepare specific spin states in the experiment.

At this point, the implementations into the experiment are still lacking for both methods and the work can be continued for example by further heating and magnetic field strength measurements of the impedance matched coil for duty cycles $< 1\%$ or by implementing a $657.937\,\mathrm{nm}$ Laser into the experiment for which dichroic mirrors would need to be used. Also, the amplifications of the magnetic field due to the impedance matching circuit only occur at a certain frequency. By using a tunable capacitor, however, the power peak could be shifted in frequency. With impedance matching, it is possible to prepare the pure $|+8\rangle$ spin state, while the spin state $|-7\rangle$ can be prepared with the isolation of a two-state system. By further investigating the energy splitting by the AC Stark effect, more two-state systems between other sublevel pairs could theoretically be isolated and a sequence for the preparation of further pure spin states could be derived.

11.3 Characterisation of the wavefront distortion in dichroic mirrors

Part C of this thesis dealt with characterising the wavefront distortion caused by dichroic mirrors, as these can be used to experimentally implement the isolation of a two-state system. This phenomenon was investigated using a Michelson interferometer setup. It was found that the $12\,\mathrm{mm}$ dichroic preserves the wavefront of reflected $405\,\mathrm{nm}$ light significantly better than the $5\,\mathrm{mm}$ dichroic, whereas the opposite was shown for transmitted $635\,\mathrm{nm}$ light. In the last case, however, the differences were much less pronounced. In the case of the $5\,\mathrm{mm}$ dichroic and a wavelength $\lambda = 405\,\mathrm{nm}$, the effective curvature of the dichroic could be determined using a fringe fit and the corresponding phase map function. The beam diameter whose wavefront is fully conserved after reflection range from $\sim 5\,\mathrm{mm}$ (for the $5\,\mathrm{mm}$ dichroic and $\lambda = 405\,\mathrm{nm}$) to $> 25.4\,\mathrm{mm}$ (for the $12\,\mathrm{mm}$ dichroic and $\lambda = 405\,\mathrm{nm}$).

The use of a Michelson interferometer proved to be a valid method to characterise the wavefront distortion. However, since the size of the investigated area on the dichroic was limited by the NPBS in the interferometer setup, a further step is to investigate the behaviour in the peripheral mirror areas using a 2” NPBS. Further investigations can also be carried out to quantitatively relate the influence of the mirror mount to the wavefront distortion in comparison to the influence of possible manufacturing or polishing imperfections. For this it is advisable to reduce the vibrational influence on the measurements and develop a more robust interferometric setup, which is sensitive enough to provide a clear interference pattern.

A Appendix

A.1 Calculations

A.1.1 Unitary transformation of the Hamiltonian in the Rotating Wave Approximation

For a transformation of the states $|\tilde{\psi}\rangle = U\ |\psi\rangle$ with a unitary transformation U, the Hamiltonian transforms in general by [Ste07]

$$\tilde{H} = UHU^\dagger + i\hbar(\partial_t U)U^\dagger. \tag{13.91}$$

The considered unitary transformation U is given as

$$U = \exp(i\omega t J_z) = \sum_{m_J=-J}^{J} \exp(i m_J \omega t)\ |m_J\rangle\langle m_J|. \tag{13.92}$$

In the following both terms are evaluated separately. The first term leads to

$$\begin{aligned} i\hbar(\partial_t U)U^\dagger &= i\hbar\left(\partial_t \sum_{m_J=-J}^{J} \exp(i m_J \omega t)\ |m_J\rangle\langle m_J|\right) \sum_{m_J=-J}^{J} \exp(-i m_J \omega t)\ \left(|m_J\rangle\langle m_J|\right)^\dagger \\ &= -\hbar m_J \omega \sum_{m_J=-J}^{J} \exp(i m_J \omega t)\exp(-i m_J \omega t)\ |m_J\rangle\langle m_J| \\ &= -\hbar m_J \omega \sum_{m_J=-J}^{J} |m_J\rangle\langle m_J| = -\omega J_z. \end{aligned} \tag{13.93}$$

The second part is slightly more complicated and leads to

$$
\begin{aligned}
UHU^\dagger &= \sum_{m_J=-J}^{J} e^{im_J\omega t}\,|m_J\rangle\langle m_J|\left(\omega_0 J_z + \frac{\Omega}{4}\,\left(e^{i\omega t}+e^{-i\omega t}\right)\,(J_+ + J_-)\right)(e^{-im_J\omega t}\,|m_J\rangle\langle m_J| \\
&= \sum_{m_J=-J}^{J} \hbar m_J\omega_0 |m_J\rangle\langle m_J| \\
&\quad + \frac{\Omega}{4}\left(e^{i\omega t}+e^{-i\omega t}\right)\left(\sum_{m_J=-J}^{J} e^{im_J\omega t}\,|m_J\rangle\langle m_J|\right) J_+ \left(\sum_{m_J=-J}^{J} e^{-im_J\omega t}\,|m_J\rangle\langle m_J|\right) \\
&\quad + \frac{\Omega}{4}\left(e^{i\omega t}+e^{-i\omega t}\right)\left(\sum_{m_J=-J}^{J} e^{im_J\omega t}\,|m_J\rangle\langle m_J|\right) J_- \left(\sum_{m_J=-J}^{J} e^{-im_J\omega t}\,|m_J\rangle\langle m_J|\right) \\
&= \sum_{m_J=-J}^{J} \hbar m_J\omega_0 |m_J\rangle\langle m_J| + \frac{\Omega}{4}\left(e^{i\omega t}+e^{-i\omega t}\right)\sum_{m_J=-J}^{J}\Big(J_+^{(J,m_J)} e^{-im_J\omega t}|m_J\rangle\langle m_J-1|e^{-i(m_J-1)\omega t} \\
&\quad + J_-^{(J,m_J)} e^{-im_J\omega t}|m_J\rangle\langle m_J+1|e^{-i(m_J+1)\omega t}\Big) \\
&= \sum_{m_J=-J}^{J} \hbar m_J\omega_0 |m_J\rangle\langle m_J| + \frac{\Omega}{4}\sum_{m_J=-J}^{J}\Big(J_+^{(J,m_J)}|m_J\rangle\langle m_J-1| + J_+^{(J,m_J)} e^{2i\omega t}|m_J\rangle\langle m_J-1| \\
&\quad + J_-^{(J,m_J)}|m_J\rangle\langle m_J+1| + J_-^{(J,m_J)} e^{-2i\omega t}|m_J\rangle\langle m_J+1|\Big) \\
&\approx \omega_0 J_z + \frac{\Omega}{4}\,(J_+ + J_-)
\end{aligned}
\tag{13.94}
$$

where $J_\pm^{(J,m_J)}$ is defined as prefactor of the transformed state $|m_J \pm 1\rangle$ in equation (3.14). In the last step, the terms with rotation components $\sim 2\omega t$ have been neglected, as their influence averages to zero over time very quickly. This leads to an approximation of the real transformed Hamiltonian and is generally known as the rotating wave approximation (RWA) [Dre17].

A.1.2 Two state Rabi oscillation differential equation

Starting point of this calculation is the matrix representation of the Hamiltonian in equation (3.20). This leads to two differential equation, where the second one is coupled to the first one:

$$
\begin{array}{lll}
\text{(I)} & \dot{\tilde{c}}_0(t) & = -i\Omega^*\,\tilde{c}_1(t) \\
\text{(II)} & \dot{\tilde{c}}_1(t) & = i\delta\,\tilde{c}_1(t) - i\Omega\,\tilde{c}_0(t)
\end{array}
\tag{13.95}
$$

To get rid of the dependence between both DE, one can calculate the derivative of (II), so that (I) can be inserted into (II). This leads to the following homogeneous DE of second order:

$$
\text{(III)} \qquad \ddot{\tilde{c}}_1(t) - i\delta\,\dot{\tilde{c}}_1(t) + |\Omega|^2\,\tilde{c}_1(t) = 0 \tag{13.96}
$$

To solve this equation, an exponential approach of the form $\tilde{c}_1(x) = A\,\exp(\alpha t)$ is suitable. Insertion in (III) leads to an equation for α, which has two solutions and is given by

$$\alpha^2 - i\delta\alpha + |\Omega|^2 = 0 \qquad \Rightarrow \qquad \alpha_{1,2} = \frac{i}{2}\left(\delta \pm \sqrt{\delta^2 + 4\,|\Omega|^2}\right). \tag{13.97}$$

The general solution of the DE in equation (13.96) is given as sum of both partial solutions:

$$\begin{aligned}\tilde{c_1}(t) &= A_1\,\exp(\alpha_1 t) + A_2\,\exp(\alpha_2 t)\\ &= \exp\left(\frac{i\delta}{2}\,t\right)\left(A_1\,\exp\left(\frac{i}{2}\,\sqrt{\delta^2 + 4\,|\Omega|^2}\,t\right) + A_2\,\exp\left(-\frac{i}{2}\,\sqrt{\delta^2 + 4\,|\Omega|^2}\,t\right)\right)\\ &= \exp\left(\frac{i\delta}{2}\,t\right)\left(\tilde{A}_1\,\cos\left(\frac{1}{2}\,\sqrt{\delta^2 + 4\,|\Omega|^2}\,t\right) + \tilde{A}_2\,\sin\left(\frac{1}{2}\,\sqrt{\delta^2 + 4\,|\Omega|^2}\,t\right)\right)\end{aligned} \tag{13.98}$$

In the last equation, the Euler identity $\exp(ix) = \cos(x) + i\,\sin(x)$ was used and the coefficients have been redefined as $\tilde{A_1} = A_1 + A_2$ and $\tilde{A_2} = i\,(A_1 - A_2)$. To determine the coefficients, the boundary conditions are used, which result from the determination of the initial state as well as Born's probability interpretation. Accordingly, it must be

$$|\tilde{c_0}(t_0)|^2 = 1 \qquad \text{and} \qquad |\tilde{c_1}(t_0)|^2 = 0 \qquad \text{for} \qquad t_0 = 0. \tag{13.99}$$

From this it can be directly deduced that $\tilde{A_1}$ = 0 holds. The time evolution for $\tilde{c_0}(t)$ follows by substituting equation (13.98) into (II) which yields to

$$\begin{aligned}\tilde{c_0}(t) &= -\frac{1}{|\Omega|}\,\left(i\dot{\tilde{c_1}}(t) + \delta\tilde{c_1}(t)\right)\\ &= -\frac{\tilde{A_2}}{|\Omega|}\,\exp\left(\frac{i\delta}{2}\,t\right)\left(\frac{i}{2}\,\sqrt{\delta^2 + 4|\Omega|^2}\,\cos\left(\frac{1}{2}\,\sqrt{\delta^2 + 4\,|\Omega|^2}\,t\right)\right.\\ &\quad\left. + \left(1 - \frac{\delta}{2}\right)\,\sin\left(\frac{1}{2}\,\sqrt{\delta^2 + 4\,|\Omega|^2}\,t\right)\right).\end{aligned} \tag{13.100}$$

From the boundary conditions it can be deduced that

$$1 = \frac{|\tilde{A_2}|^2\,\sqrt{\delta^2 + 4|\Omega|^2}}{4|\Omega|^2} \qquad \Rightarrow \qquad \tilde{A_2} = \exp(i\phi)\,\sqrt{\frac{4|\Omega|^2}{\delta^2 + 4|\Omega|^2}} \tag{13.101}$$

with ϕ being an arbitrary global phase. Thus, taking into account the boundary conditions for the coefficient of the state $|1\rangle$, the total results is given as

$$\tilde{c_1}(t) = \exp(i\phi)\,\sqrt{\frac{4|\Omega|^2}{\delta^2 + 4|\Omega|^2}}\,\sin\left(\frac{\sqrt{\delta^2 + 4\,|\Omega|^2}}{2}\,t\right) \tag{13.102}$$

and, accordingly, by forming the absolute square, the probability of finding the system in state $|1\rangle$ follows, which is represented in equation (3.24).

A.1.3 Mean of the trapping potential weighted by the square of the atomic density

To calculate the mean of the trap potential weighted with the quadratic density of the thermal cloud, first two integrals are solved, since their solutions will help at a later stage. The first integral is the integral over the Gaussian distribution

$$\int \exp\left(-\frac{x^2}{\sigma_x^2}\right)\, dx = \sqrt{\pi}\,\sigma_x. \tag{13.103}$$

The second integral is the second moment of the Gaussian distribution

$$\int \exp\left(-\frac{x^2}{\sigma_x^2}\right)\, x^2\, dx = \frac{\sqrt{\pi}}{2}\,\sigma_x^3. \tag{13.104}$$

The density distribution of a thermal cloud is generally given as

$$n(\vec{r}) = n_0\, \exp\left(-\frac{x^2}{2\sigma_x^2} - \frac{y^2}{2\sigma_y^2} - \frac{z^2}{2\sigma_z^2}\right). \tag{13.105}$$

The trapping potential $V(\vec{r})$ can be described by an harmonic oscillator potential

$$V(\vec{r}) = m\,\frac{\omega_x^2 x^2}{2} + m\,\frac{\omega_y^2 y^2}{2} + m\,\frac{\omega_z^2 z^2}{2}. \tag{13.106}$$

With these equations the mean of the trap potential weighted with the quadratic density of the thermal cloud can be calculated as follows:

$$\begin{aligned}
\iiint n^2(r)\, V(r)\, d^3r =& \frac{n_0^2 m}{2} \iiint \exp\left(-\frac{x^2}{\sigma_x^2} - \frac{y^2}{\sigma_y^2} - \frac{z^2}{\sigma_z^2}\right) \left(\omega_x^2 x^2 + \omega_y^2 y^2 + \omega_z^2 z^2\right)\, dx\, dy\, dz \\
=& \frac{n_0^2 m}{2} \left(\iiint \exp\left(-\frac{x^2}{\sigma_x^2} - \frac{y^2}{\sigma_y^2} - \frac{z^2}{\sigma_z^2}\right)\, \omega_x^2 x^2\, dx\, dy\, dz \right. \\
&+ \iiint \exp\left(-\frac{x^2}{\sigma_x^2} - \frac{y^2}{\sigma_y^2} - \frac{z^2}{\sigma_z^2}\right)\, \omega_y^2 y^2\, dx\, dy\, dz \\
&\left. + \iiint \exp\left(-\frac{x^2}{\sigma_x^2} - \frac{y^2}{\sigma_y^2} - \frac{z^2}{\sigma_z^2}\right)\, \omega_z^2 z^2\, dx\, dy\, dz \right) \\
=& \frac{n_0^2 m}{2} \left(\omega_x^2 \int \exp\left(-\frac{x^2}{\sigma_x^2}\right)\, x^2\, dx \int \exp\left(-\frac{y^2}{\sigma_y^2}\right)\, dy \int \exp\left(-\frac{z^2}{\sigma_z^2}\right)\, dz \right. \\
&+ \int \exp\left(-\frac{x^2}{\sigma_x^2}\right)\, dx\, \omega_y^2 \int \exp\left(-\frac{y^2}{\sigma_y^2}\right)\, y^2\, dy \int \exp\left(-\frac{z^2}{\sigma_z^2}\right)\, dz \\
&\left. + \int \exp\left(-\frac{x^2}{\sigma_x^2}\right)\, dx\, \omega_z^2 \int \exp\left(-\frac{y^2}{\sigma_y^2}\right)\, dy \int \exp\left(-\frac{z^2}{\sigma_z^2}\right)\, z^2\, dz \right) \\
=& \frac{m\, n_0^2}{4}\, \pi^{\frac{3}{2}}\, \sigma_x \sigma_y \sigma_z\, \left(\sigma_x^2 \omega_x^2 + \sigma_y^2 \omega_y^2 + \sigma_z^2 \omega_z^2\right)
\end{aligned} \tag{13.107}$$

A.1.4 Proof of an analytical solution for the nonlinear coupled differential equations describing dipolar relaxation

First a general case with one body processes and dipolar relaxation is considered. For this case, the atom number and the temperature in a thermal cloud can be described by

$$\begin{aligned} \dot{N} &= -\alpha N - \gamma \, \frac{N^2}{T^{\frac{3}{2}}} \\ \dot{T} &= \frac{\gamma}{4} \, \frac{N}{T^{\frac{1}{2}}}. \end{aligned} \tag{13.108}$$

With α as decay parameter of the single atom decay and γ being defined as

$$\gamma = \frac{\beta}{2^{\frac{3}{2}}} \, \omega^3 \, \left(\frac{m}{2\pi \, k_B} \right)^{\frac{3}{2}}. \tag{13.109}$$

The assumption to be tested below is that the general solution of equation (13.108) is given by

$$\begin{aligned} N(t) &= N_0 \, \exp(-\alpha t) \, \left(1 + \frac{11 \, \gamma N_0}{8 \, T_0^{\frac{3}{2}} \, \alpha} \, (1 - \exp(-\alpha t)) \right)^{-\frac{8}{11}} \\ T(t) &= T_0 \, \left(1 + \frac{11 \, \gamma N_0}{8 \, T_0^{\frac{3}{2}} \, \alpha} \, (1 - \exp(-\alpha t)) \right)^{\frac{2}{11}}. \end{aligned} \tag{13.110}$$

To prove this, the derivatives are calculated:

$$\begin{aligned} \dot{N}(t) = &- \alpha N_0 \, \exp(-\alpha t) \, \left(1 + \frac{11 \, \gamma N_0}{8 \, T_0^{\frac{3}{2}} \, \alpha} \, (1 - \exp(-\alpha t)) \right)^{-\frac{8}{11}} \\ &+ \frac{N_0^2 \, \gamma}{T_0^{\frac{3}{2}}} \, \exp(-2\alpha t) \, \left(1 + \frac{11 \, \gamma N_0}{8 \, T_0^{\frac{3}{2}} \, \alpha} \, (1 - \exp(-\alpha t)) \right)^{-\frac{19}{11}} \\ \dot{T}(t) = &\frac{N_0 \gamma}{4 T_0^{\frac{1}{2}}} \, \exp(-\alpha t) \, \left(1 + \frac{11 \, \gamma N_0}{8 \, T_0^{\frac{3}{2}} \, \alpha} \, (1 - \exp(-\alpha t)) \right)^{-\frac{9}{11}} \end{aligned} \tag{13.111}$$

Insertion into the DE in equation (13.108) immediately shows that equation (13.110) is a solution of DE. Since the dipolar relaxation process is assumed to dominate the atom loss, the one body processes can be neglected. Therefore the limit $\alpha \to 0$ is applied to the general solution. Using the Taylor series of the exponential function one can obtain

$$\lim_{\alpha \to 0} \left(\frac{1 - \exp(-\alpha t)}{\alpha} \right) = \lim_{\alpha \to 0} \left(\frac{\alpha t + \mathcal{O}(\alpha^2 t^2)}{\alpha} \right) = t. \tag{13.112}$$

This finally results in the general solution of the dipolar relaxation process neglecting one body losses:

$$\begin{aligned} N(t) &= N_0 \left(1 + \frac{11\,\gamma N_0}{8\,T_0^{\frac{3}{2}}}\,t\right)^{-\frac{8}{11}} \\ T(t) &= T_0 \left(1 + \frac{11\,\gamma N_0}{8\,T_0^{\frac{3}{2}}}\,t\right)^{\frac{2}{11}} \end{aligned} \tag{13.113}$$

A.2 Additional explanatory notes

A.2.1 Necessity of network characterisation using power waves

In order to show the relevance of the S parameters, the case of a general electrical network is treated below. An electrical network is a connection of different electrical components and has a number of ports, which indicate possible connections of the network to measurement technology or other electronics. An electrical network with n ports is generally referred to as a n-port network.

In the case of high-frequency alternating currents in electrical networks, reflections from the input power are a problem and a characterisation becomes crucial. In the DC case, to obtain a power measurement, the current I and the voltage U can be measured at the corresponding ports of the circuit. The power can then be calculated with equation (4.35). To obtain a full characterisation, this procedure has to be repeated for each port combination of the network with all other ports being shorted (at these ports the voltage vanishes, so $U = 0\,\mathrm{V}$) and opened (at these ports the current vanishes, so $I = 0\,\mathrm{A}$), depending on the exact parameter that is to be determined.

When moving to higher frequencies however, several problems arise. First of all, it is challenging for many measuring devices to measure the network current and voltage over a wide frequency range at the ports of the network. Much more critical, however, is the fact that the conditions of short or open ports that are necessary for determining the network parameters are difficult to fulfil over a wide frequency range. Finally, many electronic components such as transistors or tunnel diodes can be influenced in their function by a short or open port, which in turn affects the measurement results [Not72]. To avoid this problem, modern network analysers measure the amplitude and phase of travelling power waves instead of voltage and current. Mathematically, these two measurements methods are equivalent and can be converted into each other.

A.2.2 Generalisation of the S parameters to electrical n-port networks

To obtain a full characterisation of an electrical n-port network, the definition of the S_{11} parameter has to be generalised. For this two arbitrary network ports i and j are considered. An incoming wave $E_{\mathrm{l},i}$ is applied at port i and an outgoing wave[14] $E_{\mathrm{O},j}$ detected at port j. The S parameters are now defined as

[14] Here, the term reflected wave E_{R} can no longer be used because the outgoing wave is not reflected in the general case $i \neq j$. Only for the special case $i = j$ both terms coincide.

$$\mathsf{S}_{ji} = \frac{E_{\mathsf{O},j}}{E_{\mathsf{I},i}} \tag{13.114}$$

with all other ports being terminated. The termination avoids the problem of shorting or opening a port over a broad frequency range, by tuning the port impedance to the reference impedance Z_0. Waves that reach a terminated port are thus fully absorbed and do not influence the measurement. In high frequency applications it is common to choose a real reference impedance of $Z_0 = 50\,\Omega$.

If $j \neq i$, the S_{ji} parameter is a measurement of the transmitted wave from port i to port j, normalized to the input wave at port i. In the case $i = j$ however $\mathsf{S}_{ji} = \mathsf{S}_{jj}$ measures the reflection of the wave at port j, normalized to the input wave at port j. Overall for a n-port network, this method provides n^2 parameters which fully characterise the network in form of a set of linear equations. In matrix notation this gives

$$\begin{pmatrix} E_{\mathsf{O},1} \\ \vdots \\ E_{\mathsf{O},n} \end{pmatrix} = \begin{pmatrix} \mathsf{S}_{11} & \cdots & \mathsf{S}_{1n} \\ \vdots & \ddots & \vdots \\ \mathsf{S}_{n1} & \cdots & \mathsf{S}_{nn} \end{pmatrix} \begin{pmatrix} E_{\mathsf{I},1} \\ \vdots \\ E_{\mathsf{I},n} \end{pmatrix}. \tag{13.115}$$

A.2.3 Photon density of the RF coil

After a first estimation of the magnetic field strength has been made, the question now is whether the RF field strength is sufficient to couple the dysprosium sublevels to each other. For this purpose, it is useful to compare the photon density with the particle density of the dysprosium atoms in the experimental chamber. The energy density u of the electromagnetic field can be calculated with E as the electric field, D as the electric displacement field, H as the magnetizing field and B as the magnetic flux density as

$$u = \frac{1}{2}\left(\vec{E}\cdot\vec{D} + \vec{B}\cdot\vec{H}\right) = \frac{\left|\vec{B}\right|^2}{\mu_0}. \tag{13.116}$$

Generally, when dealing with dispersive materials, the permittivity ε and the permeability μ are tensors. In the case considered here, the medium is assumed to be air, which is non dispersive. Therefore it is reasonable to assume $\varepsilon = \varepsilon_0$ and $\mu = \mu_0$ to be scalar as well as to use the relations $\vec{D} = \varepsilon_0\vec{E}$ and $\vec{B} = \mu_0\vec{H}$. Together with the general relations $B = \frac{E}{c}$ and $c = \frac{1}{\sqrt{\varepsilon\mu}}$ the energy density can be expressed depending only on the magnetic field strength $|\vec{B}|$. For a frequency f, the number of photons per cubic meter can be determined with

$$E_{\mathsf{Ph}} = N_{\mathsf{Ph}} h f \tag{13.117}$$

where E_{Ph} is the total energy of a total amount of N_{Ph} photons. By normalising this result to the volume one obtains a general formula for the photon density

$$n_{\mathsf{Ph}} = \frac{\left|\vec{B}(f)\right|^2}{\mu_0 h f}. \tag{13.118}$$

The photon density depends in particular on the frequency of the RF coil. In figure 47 the frequency-dependent photon density is shown, including a reference curve which neglects the skin effect.

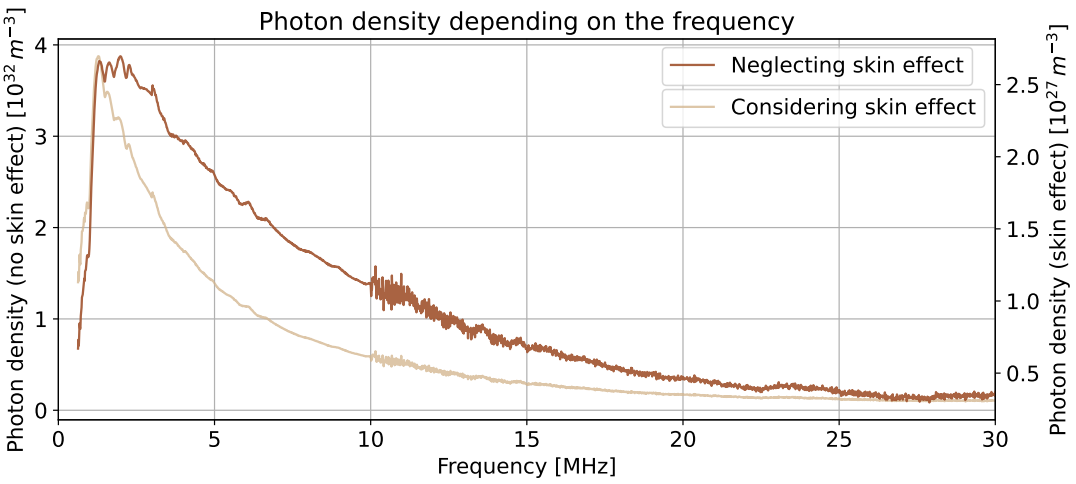

Figure 47: Photon density at the position of the atomic cloud. The simulation assumes the same conditions as the magnetic field simulation in figure 18, since the photon density has been directly calculated from the magnetic field strength with equation (13.118). The calculation has been done considering skin effect, which is the physical right approach but also neglecting the skin effect, as a reference value.

The photon density in the regime relevant for the experiment is of the order $\sim 10^{27}\,\mathrm{m}^{-3}$. In the next step this photon density is compared with the density of the dysprosium atoms in the experimental chamber. Generally the total density $n = n_\mathrm{c} + n_\mathrm{th}$ consists of the condensed atom density n_c and the not condensed atoms, which form a thermal cloud with density n_th. The experimental applications of the RF coil all focus on thermal clouds, so for a calculation of the density of a condensate it is referred to [Dal+99].

The center density $n_{\mathrm{th},0}$ can be calculated according to [Pol17] for a known atomic number N, a known temperature T and known trapping frequencies by

$$n_{\mathrm{th},0} = N\omega^3 \left(\frac{m}{2\pi k_\mathrm{B} T}\right)^{\frac{3}{2}}. \tag{13.119}$$

This formula involves ω being the geometric average of the trapping frequencies $\omega_{x,y,z}$, so

$$\omega = (\omega_x \omega_y \omega_z)^{\frac{1}{3}}. \tag{13.120}$$

For the experimental configuration where the resonance measurements will take place, the trapping frequencies were determined experimentally to be $[\omega_x, \omega_y, \omega_z] = [280.7, 151.6, 319.0]$ Hz. Taking into account gravity influences, one gets trapping frequencies $[\omega_x, \omega_y, \omega_z] = [281.7, 151.7, 314.9]$ Hz, which leads to a geometrical average of $\omega = 237.86$ Hz. The atomic number and temperature of the cloud can also be determined experimentally. The total atom number during the measurement configuration is given as $N = (7.98 \pm 0.22) \cdot 10^5$. The temperature can be determined by the expansion of the cloud. For low temperatures the expansion of the cloud is not necessarily isotropic, which was confirmed by a temperature measurement in the x and y axis. The two temperatures have been determined to be $T_x = (1.117 \pm 0.005)\,\mu$K and $T_y = (1.234 \pm 0.013)\,\mu$K. A significant deviation between both measurements is evident, so for the calculation of the atom density, the average of both temperatures $T = (1.1755 \pm 0.014)\,\mu$K will be used.

With equation (13.119), this leads to $n_{\text{th},0} = (1.48 \pm 0.05)\ 10^{18}\,\text{m}^{-3}$ as the particle density in the center of the peak. Therefore the photon density is 9 magnitudes higher compared to the density of dysprosium atoms and a sufficient saturation is expected, even after possible secondary losses due to the metallic experimental environment. Since $n_{\text{th},0}$ is the center density of the cloud, the photon to atom ratio is even larger at other points in the cloud.

A.2.4 Runge Kutter Method of solving differential equations

Due to the complexity of the coupled and nonlinear DE displayed in equation (6.56) and equation (6.61), it is difficult to derive an analytical solution without a proper ansatz. Therefore, in addition, a numerical solution method is presented here, which is able to solve the DE. Precisely the Runge Kutter method will be presented, which is a numerical one-step solving method for initial value problems (IVP), including coupled nonlinear equations. Strictly speaking, the Runge Kutter method this is not a specific procedure, but rather a general approach and a family of methods. In this thesis, the focus will be on the methods relevant for the solution of dipolar relaxation. Let an initial value problem

$$y'(t) = f(t, y(t)) \qquad \text{where} \qquad y(t_0) = y_0 \qquad \text{for} \qquad y : \mathbb{R} \to \mathbb{R}^d \tag{13.121}$$

be given. First, discrete points t_n are defined for the variable t at which the solution of the IVP is to be approximated. The equidistant spacing of these points, also sometimes called support points, is defined as step-size δt. The s step Runge Kutter method is now defined iterative as

$$y(t_{n+1}) = y(t_n) + \delta t \sum_{j=1}^{s} b_j k_j \tag{13.122}$$

with b_j as weights of the k_j terms, which can be interpreted as slope in the δt interval for different t and y configurations. For $s = 4$ these k_j terms are usually defined as [Pre+07] [SM03]:

$$\begin{aligned}
k_1 &= f(t_n, y(t_n)) && \text{slope at the current iteration step} \\
k_2 &= f\left(t_n + \tfrac{\delta t}{2}, y(t_n) + \delta t\, \tfrac{k_1}{2}\right) && \text{slope at } t_n + \tfrac{\delta t}{2} \text{ with } k_1\text{-linear } y \text{ extrapolation} \\
k_3 &= f\left(t_n + \tfrac{\delta t}{2}, y(t_n) + \delta t\, \tfrac{k_2}{2}\right) && \text{slope at } t_n + \tfrac{\delta t}{2} \text{ with } k_2\text{-linear } y \text{ extrapolation} \\
k_4 &= f\left(t_n + \delta t, y(t_n) + \delta t\, k_3\right) && \text{slope at } t_{n+1} \text{ with } k_3\text{-linear } y \text{ extrapolation}
\end{aligned} \tag{13.123}$$

The case $s = 4$ is the standard Runge Kutter method, which is normally referenced as such in the literature. In the case of dipolar relaxation, the first milliseconds are of particular interest, so a 1-step Runge Kutter method (with $s = 1$ by definition) will prove to be sufficient. At this point it should be noted that the 1 step Runge Kutter method is identical to the Euler method, or in other words, that the Euler method is a special case of the general s-step Runge Kutter method. The solution of the coupled nonlinear DE was performed with a step size of $\delta t = 50\,\text{ns}$ for a total of $N = 100000$ steps in Python. The code for the solution is provided in the appendix in subsection A.3.3. The results obtained by this numerical solution method are presented and evaluated in subsection 6.4 together with an analytical solution.

A.3 Technical drawings

The technical drawings of the holders and adapters produced in the scope of this thesis are presented below. To avoid vibrations and for better cooling of the RF amplifier, an adapter plate was made to attach the RF amplifier to a water-cooled breadboard. The RF amplifier is the LZY-22+, which has a maximum output power of $P_{\text{max}} = 30\,\text{W}$ [Min17b].

The RF holder is suitable for diagonal mounting on a breadboard, close to an experimental chamber. The exact distance of the RF coil to the atoms can be adjusted by winding the coil, as it is completely removable. Anodised aluminium was chosen as the material for the RF holder to ensure thermal and mechanical resistance on the one hand and a low reflection coefficient on the other.

To ensure a fixation of the dichroic mirrors without disturbing or bending the surface coating, a special mount has been designed. The mount consists of several parts from Thorlabs and also three individual, customized parts. The first one is the main holder, where the mirror gets clamped on. The second one is a mirror clamp for the bottom of the mirror, which secures the mirror by two contact points on its tilted side. The third one is a smaller clamp on top of the mount. This clamp presses the mirror against the mount and therefore has two contact spots on the surface of the mirror. The first two customised parts have been manufactured from aluminium, while the third one has a too complicated structure. Therefore the clamp is 3D printed from a PLA filament.

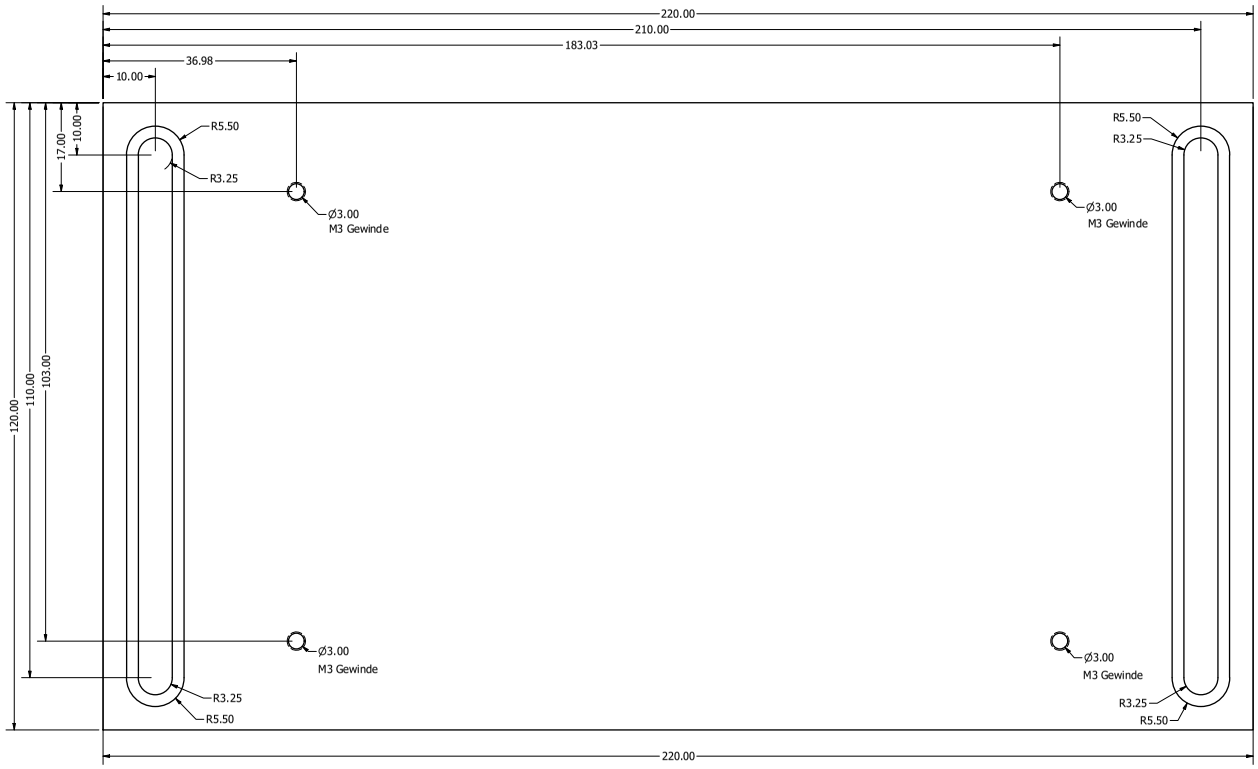

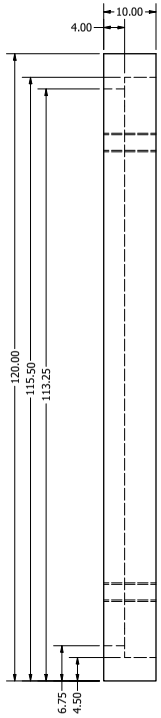

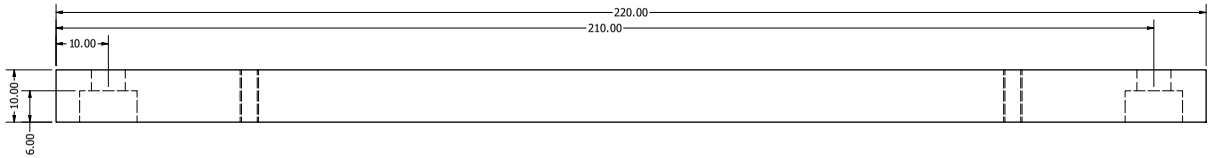

DRAWN QFRie	27/04/2023	
CHECKED		TITLE: Cooling Plate - 30 W RF Amplifier
QA		
MFG		
APPROVED		
		SIZE D / DWG NO Cooling plate - Sketch 3 / REV
		SCALE 2 : 1 / SHEET 1 OF 1

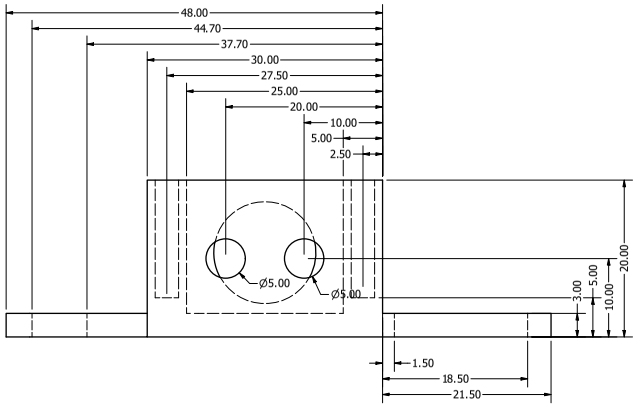

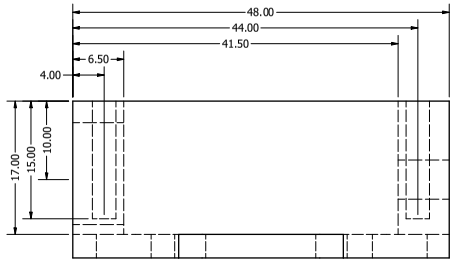

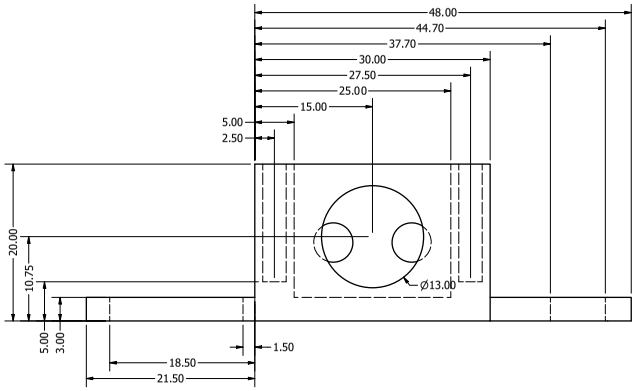

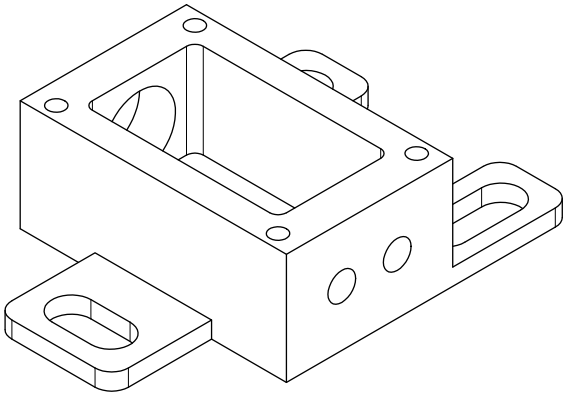

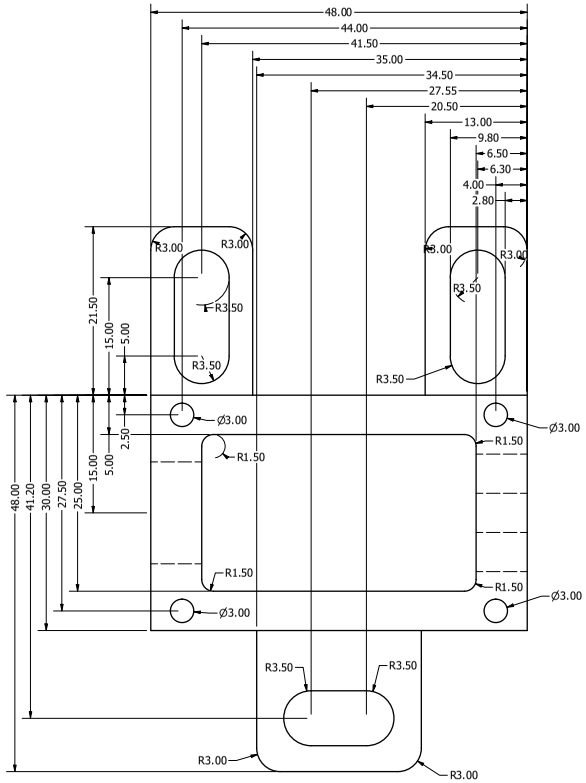

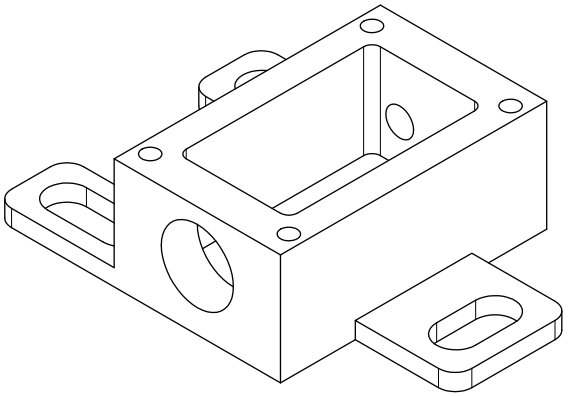

DRAWN QFRie	26/04/2023		
CHECKED		TITLE	
QA			
MFG			
APPROVED		SIZE D	DWG NO RF Holder - Base 2 REV
		SCALE 3 : 1	SHEET 1 OF 1

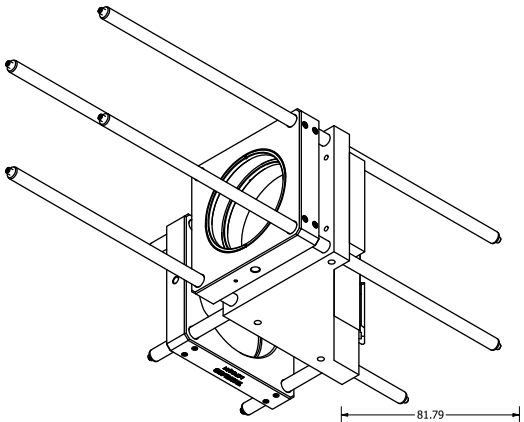

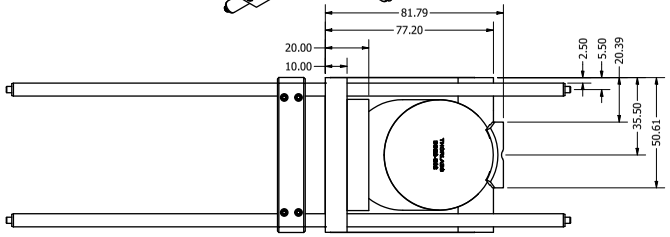

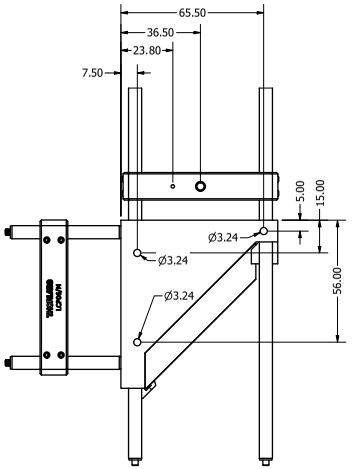

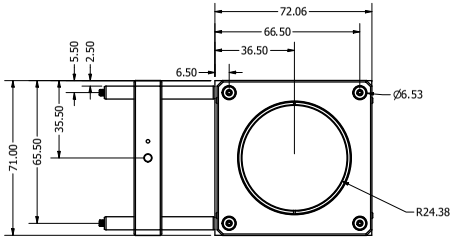

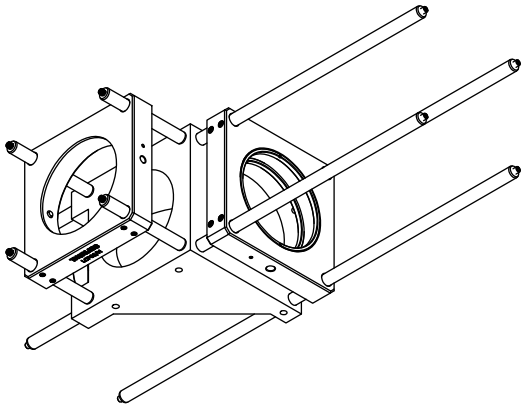

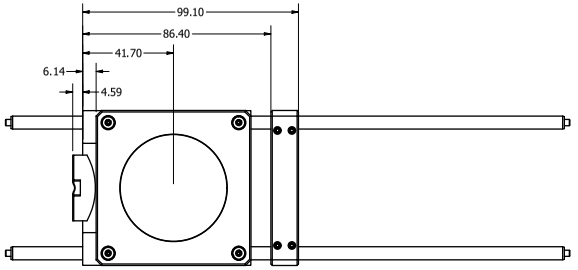

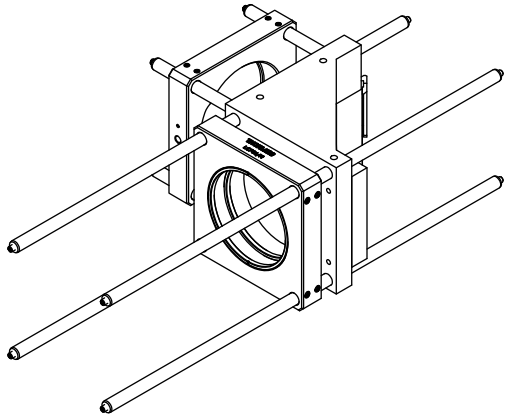

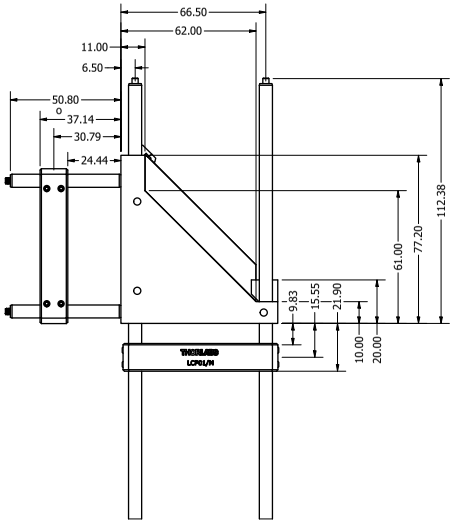

DRAWN QFRie	25/07/2023	
CHECKED		TITLE: Dichroic Mirror Mount
QA		
MFG		
APPROVED		
		SIZE D · DWG NO Assembly_of_dichroic_mirror_V2-1 · REV
		SCALE 1 / 1.2 · SHEET 1 OF 1

A.4 Python and C++ code

A.4.1 Calculating Rabi oscillations in the dysprosium 17 state system in Python

Due to the complexity and length of the calculations performed in Python, the complete code cannot be given here. Instead, the most important key points are given, respectively the calculation of the time evolution via numerical matrix diagonalisation. For this the total angular momentum J, the detuning z and the Rabi frequency Ω_R of the B_{RF} field are considered as given.

```
import numpy as np
from numpy import linalg as LA

# First we define the matrices:

def H_diag_real(J,z):
    Mat =  np.zeros(( int(2*J +1) ,int(2*J +1) ))
    for i in range( 0, int(2*J +1) ):
        mJ = J - i
        Mat[i,i] = - hbar * mJ * z * 1000
    return Mat

def J_l_offdiag_real(J,Omega_1):
    Mat =  np.zeros(( int(2*J+1) ,int(2*J+1) ))
    for i in range( 0, int(2*J) ):
        mJ = J - i
        Mat[i+1,i] = -Omega_1/4 *hbar * np.sqrt( J*(J+1) - mJ*(mJ-1) )
    return Mat

def J_r_offdiag_real(J,Omega_1):
    Mat = np.transpose(J_l_offdiag_real(J,Omega_1))
    return Mat

def H_real(J,z,Omega_1):
    Mat = J_l_offdiag_real(J,Omega_1) + J_r_offdiag_real(J,Omega_1) + H_diag_real(J,z)
    return Mat

# Now we calcualte the eigenvalues and eigenvectors of the Hamiltonian:

evals_real, evecs_real = LA.eigh(H_real(J,z,Omega))

# Now we determine the coefficients of the initial state in the new eigenbasis:

coefficients_real = evecs_real.conj().T @ initial

# Now we calculate the probabilites:

Probabilities_real = np.transpose([np.abs(evecs_real @ (np.exp(-1j*evals_real*t/hbar)*
    coefficients_real))**2 for t in tvals])
```

Listing 1: Calculating the time evolution in Dysprosium in Python via matrix diagonalisation. The output is a matrix with the probabilities to measure a specific state (rows) at a specific time (columns).

A.4.2 Implementing magnetic field transformations in Python via Labscript

The Python code for controlling the magnetic field coils of the experimental chamber is provided below. The transformation that was chosen as example is the second transformation of subsection 5.3. Namely the transformation is a rotation of the B-field vector around a previously defined spatial axis

with additional adjustable angle to this axis. The coils are controlled in Python by using the package Labscript [Sta+13].

```
# Here we define the constants from the coil characterisation (Date of last update: 14.06.2023)

Bx_0 = 0.061
By_0 = 0.334
Bz_0 = 0.447

ax = 9.221
ay = 9.883
az = 10.554

# Here we calculate a function which gives us the current for the different coils:

def x_current_rotation_with_angle(t, B, Theta, Phi, Xi, ang_freq):
    I_x = B*(np.cos(Xi)*np.sin(Theta)*np.cos(Phi) + np.sin(Xi)*np.sin(ang_freq*t)*np.cos(Theta)*np.cos(Phi) - np.sin(Xi)*np.cos(ang_freq*t)*np.sin(Phi))/ax - Bx_0 / ax
    return I_x

def y_current_rotation_with_angle(t, B, Theta, Phi, Xi, ang_freq):
    I_y = B*(np.cos(Xi)*np.sin(Theta)*np.sin(Phi) + np.sin(Xi)*np.sin(ang_freq*t)*np.cos(Theta)*np.sin(Phi) + np.sin(Xi)*np.cos(ang_freq*t)*np.cos(Phi))/ay - By_0 / ay
    return I_y

def z_current_rotation_with_angle(t, B, Theta, Xi, ang_freq):
    I_z = B*(np.cos(Xi)*np.cos(Theta) - np.sin(Xi)*np.sin(ang_freq*t)*np.sin(Theta))/az - Bz_0 / az
    return I_z

# Here we define the function which performs multiple roations

def magnetic_field_transformation(t, duration, B, Theta_deg, Phi_deg, Xi_deg, ang_freq):

    Theta = Theta_deg *2*np.pi/360
    Phi = Phi_deg *2*np.pi/360
    Xi = Xi_deg *2*np.pi/360

    AO_MOT_CompX_Coil_current.customramp(t, duration, x_current_rotation_with_angle , B, Theta, Phi, Xi, ang_freq , units='A')
    AO_MOT_CompY_Coil_current.customramp(t, duration, y_current_rotation_with_angle , B, Theta, Phi, Xi, ang_freq , units='A')
    AO_MOT_CompZ_Coil_current.customramp(t, duration, z_current_rotation_with_angle ,B, Theta, Xi, ang_freq , units='A')

    return t
```

Listing 2: Example code for a magnetic field rotation in Python using the package Labscript. The chosen transformation is a rotation around a spatially fixed axis with an adjustable angle between field vector and rotation axis.

To get a better understanding of the field transformation from above, a code for visualisation is given below. The field vector for given parameters is shown in a 3D plot, while the current values of the different coils are shown in a 2D plot below. This visualisation is output and saved as a .gif file.

```
import numpy as np
import matplotlib.pyplot as plt
from matplotlib.animation import FuncAnimation

B = 1
Theta_deg = 70
```

```
Phi_deg = 30
Xi_deg = 30
Rotation_N = 3

Theta = Theta_deg*2*np.pi/360
Phi = Phi_deg*2*np.pi/360
Xi = Xi_deg*2*np.pi/360

fig = plt.figure()
fig.set_size_inches(12,15)
plt.rc('font', size=10)
ax = fig.add_subplot(3,1,(1,2) , projection='3d')

xx, yy = np.meshgrid(np.linspace(-1,1,10), np.linspace(-1,1,10))
z = 0*xx
ax.plot_surface(xx, yy, z, alpha=0.1, color='blue')

zz, yy = np.meshgrid(np.linspace(-1,1,10), np.linspace(-1,1,10))
x = 0*xx
ax.plot_surface(x, yy, zz, alpha=0.1, color='blue')

xx, zz = np.meshgrid(np.linspace(-1,1,10), np.linspace(-1,1,10))
y = 0*xx
ax.plot_surface(xx, y, zz, alpha=0.1, color='blue')

ax.scatter(0,0,0, c='black', marker='o', s=80)
ax.quiver(0, 0, 0, 1, 0, 0, color='black', arrow_length_ratio=0, linewidth=0.5)
ax.quiver(0, 0, 0, -1, 0, 0, color='black', arrow_length_ratio=0, linewidth=0.5)
ax.quiver(0, 0, 0, 0, 1, 0, color='black', arrow_length_ratio=0, linewidth=0.5)
ax.quiver(0, 0, 0, 0, -1, 0, color='black', arrow_length_ratio=0, linewidth=0.5)
ax.quiver(0, 0, 0, 0, 0, 1, color='black', arrow_length_ratio=0, linewidth=0.5)
ax.quiver(0, 0, 0, 0, 0, -1, color='black', arrow_length_ratio=0, linewidth=0.5)

ax.set_xlabel('x field [G]',fontsize=10)
ax.set_ylabel('y field [G]',fontsize=10)
ax.set_zlabel('z field [G]',fontsize=10)
plt.title('Spatial orientation of the field vector',fontsize=16)

bx = fig.add_subplot(3,1,3)

bx.set_xlabel('Time [rel.]',fontsize=10)
bx.set_ylabel('Current [A]',fontsize=10)
bx.set_title('Current during the rotation and scaling',fontsize=16)

props = dict(boxstyle='square', facecolor='whitesmoke', alpha=0.5)

def get_arrow(par):
    x = 0
    y = 0
    z = 0
    u = B*(np.cos(Xi)*np.sin(Theta)*np.cos(Phi) + np.sin(Xi)*np.sin(2*np.pi*Rotation_N*
    par)*np.cos(Theta)*np.cos(Phi) - np.sin(Xi)*np.cos(2*np.pi*Rotation_N*par)*np.sin(
    Phi))
    v = B*(np.cos(Xi)*np.sin(Theta)*np.sin(Phi) + np.sin(Xi)*np.sin(2*np.pi*Rotation_N*
    par)*np.cos(Theta)*np.sin(Phi) + np.sin(Xi)*np.cos(2*np.pi*Rotation_N*par)*np.cos(
    Phi))
    w = B*(np.cos(Xi)*np.cos(Theta) - np.sin(Xi)*np.sin(2*np.pi*Rotation_N*par)*np.sin(
    Theta))
    return x,y,z,u,v,w

def get_x(par):
    x = 0
    y = 0
    z = 0
```

```
66      u = B*(np.cos(Xi)*np.sin(Theta)*np.cos(Phi) + np.sin(Xi)*np.sin(2*np.pi*Rotation_N*
        par)*np.cos(Theta)*np.cos(Phi) - np.sin(Xi)*np.cos(2*np.pi*Rotation_N*par)*np.sin(
        Phi))
67      v = 0
68      w = 0
69      return x,y,z,u,v,w
70
71  def get_y(par):
72      x = 0
73      y = 0
74      z = 0
75      u = 0
76      v = B*(np.cos(Xi)*np.sin(Theta)*np.sin(Phi) + np.sin(Xi)*np.sin(2*np.pi*Rotation_N*
        par)*np.cos(Theta)*np.sin(Phi) + np.sin(Xi)*np.cos(2*np.pi*Rotation_N*par)*np.cos(
        Phi))
77      w = 0
78      return x,y,z,u,v,w
79
80  def get_z(par):
81      x = 0
82      y = 0
83      z = 0
84      u = 0
85      v = 0
86      w = B*(np.cos(Xi)*np.cos(Theta) - np.sin(Xi)*np.sin(2*np.pi*Rotation_N*par)*np.sin(
        Theta))
87      return x,y,z,u,v,w
88
89  def current(par):
90      Bx_0 = 0.061
91      By_0 = 0.334
92      Bz_0 = 0.447
93
94      ax = 9.221
95      ay = 9.883
96      az = 10.554
97
98      Bx_p = B*(np.cos(Xi)*np.sin(Theta)*np.cos(Phi) + np.sin(Xi)*np.sin(2*np.pi*
        Rotation_N*par)*np.cos(Theta)*np.cos(Phi) - np.sin(Xi)*np.cos(2*np.pi*Rotation_N*par
        )*np.sin(Phi))
99      By_p = B*(np.cos(Xi)*np.sin(Theta)*np.sin(Phi) + np.sin(Xi)*np.sin(2*np.pi*
        Rotation_N*par)*np.cos(Theta)*np.sin(Phi) + np.sin(Xi)*np.cos(2*np.pi*Rotation_N*par
        )*np.cos(Phi))
100     Bz_p = B*(np.cos(Xi)*np.cos(Theta) - np.sin(Xi)*np.sin(2*np.pi*Rotation_N*par)*np.
        sin(Theta))
101
102     Ix = Bx_p /ax - Bx_0 /ax
103     Iy = By_p /ay - By_0 /ay
104     Iz = Bz_p /az - Bz_0 /az
105
106     return par , Ix , Iy , Iz
107
108 def parameter(par):
109     B_val = B
110     Theta_val = (Theta)
111     Phi_val = Phi
112     Xi_val = Xi
113
114     return B_val , Theta_val , Phi_val , par , Xi_val
115
116
117 Textbox = ax.text(16 ,16 , 0,'\n'.join((
118     rf'$B={round(parameter(0)[0],1)}$ G',
119     rf"$\theta={round(parameter(0)[1]*360/(2*np.pi),1)}$ ",
```

```
    rf"$\phi={round(parameter(0)[2]*360/(2*np.pi),1)}$ ",
    rf"$\xi={round(parameter(0)[3]*360/(2*np.pi),1)}$ "))
    , transform=ax.transAxes, fontsize=14,verticalalignment='top', bbox=props)


quiver = ax.quiver(*get_arrow(0), color='darkblue', arrow_length_ratio=0.1, label = "Field vector")

quiver_x = ax.quiver(*get_x(0), color='black', arrow_length_ratio=0.1, label = "x-projection")
quiver_y = ax.quiver(*get_y(0), color='red', arrow_length_ratio=0.1, label = "y-projection")
quiver_z = ax.quiver(*get_z(0), color='goldenrod', arrow_length_ratio=0.1, label = "z-projection")

lx_plot = bx.errorbar(current(0)[0], current(0)[1], color='black', marker = "." , label = r"$I_x$ current")
ly_plot = bx.errorbar(current(0)[0], current(0)[2], color='red', marker = "." , label = r"$I_y$ current")
lz_plot = bx.errorbar(current(0)[0], current(0)[3], color='goldenrod', marker = "." , label = r"$I_z$ current")

bx.plot([0,1], [0,0], color = "black", alpha = 0.3)

ax.set_xlim(-1, 1)
ax.set_ylim(-1, 1)
ax.set_zlim(-1, 1)
ax.legend()

bx.set_xlim(0, 1)

ax.scatter(0,0,0, c='black', marker='none', s=80, label="\n".join([rf'$\alpha_1 = ${alpha_deg}', rf'$\beta = ${beta_deg}', rf'$B_1 = ${B_1}', rf'$B_2 = ${B_2}']))
bx.grid()

def update(i):

    global quiver
    quiver.remove()
    quiver = ax.quiver(*get_arrow(i), color='darkblue', arrow_length_ratio=0.1, label = "Field vector")

    global quiver_x
    quiver_x.remove()
    quiver_x = ax.quiver(*get_x(i), color='black', arrow_length_ratio=0.1, label = "x-projection")

    global quiver_y
    quiver_y.remove()
    quiver_y = ax.quiver(*get_y(i), color='red', arrow_length_ratio=0.1, label = "y-projection")

    global quiver_z
    quiver_z.remove()
    quiver_z = ax.quiver(*get_z(i), color='goldenrod', arrow_length_ratio=0.1, label = "z-projection")

    global Textbox
    Textbox.remove()
    Textbox = ax.text(16, 16, 0,'\n'.join((
    rf'$B={round(parameter(i)[0],1)}$ G',
    rf"$\theta={round(parameter(i)[1]*360/(2*np.pi),1)}$ ",
    rf"$\phi={round(parameter(i)[2]*360/(2*np.pi),1)}$ ",
    rf"$\xi={round(parameter(0)[3]*360/(2*np.pi),1)}$ "))
```

```
    , transform=ax.transAxes, fontsize=14,verticalalignment='top', bbox=props)

    global lx_plot
    lx_plot = bx.errorbar(current(i)[0], current(i)[1], color='black', label = r"$I_x$
    current", marker = ".")

    global ly_plot
    ly_plot = bx.errorbar(current(i)[0], current(i)[2], color='red', label = r"$I_y$
    current", marker = ".")

    global lz_plot
    lz_plot = bx.errorbar(current(i)[0], current(i)[3], color='goldenrod', label = r"
    $I_z$ current", marker = ".")


    handles, labels = plt.gca().get_legend_handles_labels()
    by_label = dict(zip(labels, handles))
    plt.legend(by_label.values(), by_label.keys())


ani = FuncAnimation(fig, update, frames=np.linspace(0,1,200), interval=50, blit=False,
    repeat=False)
ani.save('Multiple_rotation_with_angle.gif', writer = 'ffmpeg', fps = 30)
```

Listing 3: Visualisation of the magnetic field transformations in Python. The visualisation code corresponds to the previously shown transformaton.

A.4.3 Solving two coupled nonlinear differential equations that describe a dipolar relaxation process via the Runge Kutter method numerically in Python

Here the code for a numerical solution of coupled differential equations via the Runge-Kutter method will be provided. For a small deviation from the analytical solution, it is necessary to consider a low total development time as well as a high number of time steps. The differential equations that are numerically solved here are displayed in equation (6.56) and equation (6.61).

```
# First we set the initial values:

N1 = np.array([ N_0 ])
N2 = np.array([ T_0 ])

# Here we define the prefactors in the differential equation:

Gamma1 = beta*omega**3 /2**(3/2)*(m/(2*np.pi*k_B))**(3/2)
Gamma2 = omega**3*beta/(8*np.sqrt(2))*(m/(2*np.pi*k_B))**(3/2)

# Here the maximal evolution time and the number of steps are defined:

time = .005     # in s
Steps = 100000

# Now we calculate the solution stepweise for small timesteps:

for step in range(0,Steps):
    N1  = np.append( N1, N1[step] + time/Steps*(-Gamma1*N1[step]**2 /N2[step]**(3/2)) )
    N2  = np.append( N2, N2[step] + time/Steps*( Gamma2*N1[step] /N2[step]**(1/2)) )
```

Listing 4: Numerical solution of the coupled differential equations of the dipolar relaxation via the Runge-Kutter method.

A.4.4 Calculation of the polarisabilities of dysprosium in C++ for a given wavelength interval

The calculation of the polarizabilities of dysprosium has been excluded from the actual Python analysis code. The reason for this is the long computation time that Python needs, especially when using for loops. C++ is much more efficient than Python in carrying out these calculations. A direct comparison showed that the C++ code was about a time factor of 20 faster than the Python code. The C++ code provided here stores the real and imaginary values of the scalar, vector and tensor polarizabilities in a .txt file. This text file can then be loaded into a Python code for further data analysis.

```
#include <iostream>
#include <fstream>
#include <cmath>
#include <vector>
#include <string>
#include <sstream>

// First of all we declare the functions:

void writeDataToFile();
void CoefEnergieShiftIJ_L();
void GlobalEnergyShift_L();

// We define some constants:

    double J0 = 8;
    double c = 299792458; // speed of light
    double e = 1.602176634e-19; // electric charge
    double me = 9.1093837015e-31; // electron mass
    double u = 1.660538921e-27; // Atomic mass unit
    double muB = 9.27400915e-24; // Bohr Magneton
    double h = 6.62606896e-34;
    double hbar = 1.05457e-34;
    double kb = 1.3806503e-23; // Boltzmann constant
    double g = 9.80553; // gravitation
    double a0 = 5.29e-11; // Bohr's radius
    double mu0 = 4 * M_PI * 1e-7; // magnetic constant
    double ascatt = 137 * a0;
    double epsilon0 = 8.854187817e-12;
    double atomic_unit = e * e * a0 * a0 * a0 * a0 * me / (hbar * hbar); // atomic unit
    for the polarizability
    double T = 100 * 1e-9; // temperature of the trap
    double m = 164 * u; // dysprosium mass

// Now we define the functions:

void writeDataToFile(const std::string& filename, const std::vector<double>& lambdaL,
    const std::vector<double>& alphaS,
                    const std::vector<double>& alphaV, const std::vector<double>&
    alphaT,
                    const std::vector<double>& alphaSimg, const std::vector<double>&
    alphaVimg,
                    const std::vector<double>& alphaTimg) {
    std::ofstream file(filename);
    if (!file.is_open()) {
        std::cout << "Fehler beim  ffnen  der Datei: " << filename << std::endl;
        return;
    }

    file << "lambda\talphaS\talphaV\talphaT\talphaSimg\talphaVimg\talphaTimg\n";

    for (size_t i = 0; i < lambdaL.size(); i++) {
```

```
        file << lambdaL[i] << '\t' << alphaS[i] << '\t' << alphaV[i] << '\t' << alphaT[i] << '\t'
             << alphaSimg[i] << '\t' << alphaVimg[i] << '\t' << alphaTimg[i] << '\n';
    }

    file.close();
}

double CoefEnergieShiftIJ_L(double GammaIJ, double OmegaIJ, double OmegaL) {
    double h = 6.62606896e-34;
    double hbar = h / (2 * M_PI);
    double c = 2.99792458e8;
    double epsilon0 = 8.854187817e-12;

    double coef = (3 * M_PI * epsilon0 * hbar * pow(c, 3));

    double kappaIJ = (GammaIJ / pow(OmegaIJ, 3)) * coef * 1 / (pow(hbar, 2) * (pow(OmegaIJ, 2) - pow(OmegaL, 2)));

    return kappaIJ;
}

std::vector<double> Return_Alphas(double alphaSTot, double alphaVTot, double alphaTTot, double alphaSimgTot, double alphaVimgTot, double alphaTimgTot){

     std::vector<double> Vec;

    Vec.push_back(alphaSTot);
    Vec.push_back(alphaVTot);
    Vec.push_back(alphaTTot);
    Vec.push_back(alphaSimgTot);
    Vec.push_back(alphaVimgTot);
    Vec.push_back(alphaTimgTot);

    return Vec;
}

std::vector<double> GlobalEnergyShift_L(double J0, const std::vector<double>& JExTable, const std::vector<double>& GammaExTable, const std::vector<double>& OmegaExTable, double OmegaL) {

    // Coefficient
    int NLevel = JExTable.size();

    // Calculation
    double kappaIJ = 0.0;
    double alphaSTot = 0.0;
    double alphaSimgTot = 0.0;
    double alphaVTot = 0.0;
    double alphaVimgTot = 0.0;
    double alphaTTot = 0.0;
    double alphaTimgTot = 0.0;
    double hbar = 1.05457e-34;

    for (int iEx = 0; iEx < NLevel; ++iEx) {

        double JEx = JExTable[iEx];

        double kappaIJ = (2 * JEx + 1) * CoefEnergieShiftIJ_L(GammaExTable[iEx], OmegaExTable[iEx], OmegaL);  // equation 42
        double alphaS = hbar * OmegaExTable[iEx] * kappaIJ * 2 / (3 * (2 * J0 + 1));
        double alphaSimg = hbar * GammaExTable[iEx] * ((pow(OmegaExTable[iEx], 2) + pow(OmegaL, 2)) / (pow(OmegaExTable[iEx], 2) - pow(OmegaL, 2))) * kappaIJ * 1 / (3 * (2 * J0 + 1));
```

```
105         double alphaV = hbar * OmegaL * kappaIJ * (JEx * (JEx + 1) - J0 * (J0 + 1) - 2)
    / ((J0 + 1) * (2 * J0 + 1));
106         double alphaVimg = hbar * OmegaL * OmegaExTable[iEx] * GammaExTable[iEx] / (pow(
    OmegaExTable[iEx], 2) - pow(OmegaL, 2)) * kappaIJ * (JEx * (JEx + 1) - J0 * (J0 + 1)
     - 2) / ((J0 + 1) * (2 * J0 + 1));
107         double alphaT = -hbar * OmegaExTable[iEx] * kappaIJ * (3 * (pow(JEx * (JEx + 1)
    - J0 * (J0 + 1), 2)) - 9 * JEx * (JEx + 1) + J0 * (J0 + 1) + 6) / (3 * (J0 + 1) * (2
     * J0 + 1) * (2 * J0 + 3));
108         double alphaTimg = -hbar * GammaExTable[iEx] * ((pow(OmegaExTable[iEx], 2) + pow
    (OmegaL, 2)) / (pow(OmegaExTable[iEx], 2) - pow(OmegaL, 2))) * kappaIJ * (3 * (pow(
    JEx * (JEx + 1) - J0 * (J0 + 1), 2)) - 9 * JEx * (JEx + 1) + J0 * (J0 + 1) + 6) / (6
     * (J0 + 1) * (2 * J0 + 1) * (2 * J0 + 3));
109
110         alphaSTot += alphaS;
111         alphaSimgTot += alphaSimg;
112         alphaVTot += alphaV;
113         alphaVimgTot += alphaVimg;
114         alphaTTot += alphaT;
115         alphaTimgTot += alphaTimg;
116     }
117     std::vector<double> Vec = Return_Alphas(alphaSTot, alphaVTot, alphaTTot,
    alphaSimgTot, alphaVimgTot, alphaTimgTot);
118     return Vec;
119 }
120
121 int main() {
122
123 std::ifstream inputFile("lineDy_latest.txt");
124     if (!inputFile) {
125         std::cout << "Fehler beim   ffnen   der Datei." << std::endl;
126         return 1;
127     }
128
129     std::vector<double> column3;
130     std::vector<double> column4;
131     std::vector<double> column6;
132     std::vector<double> Jex;
133     std::vector<double> Gammacr;
134     std::vector<double> E_cr;
135     std::vector<double> omegacr;
136     std::vector<double> lambdacr;
137
138     double value1, value2, value3, value4, value5, value6, value7;
139     while (inputFile >> value1 >> value2 >> value3 >> value4 >> value5 >> value6 >>
    value7) {
140         Jex.push_back(value4);
141         E_cr.push_back(value5);
142         Gammacr.push_back(value7);
143         omegacr.push_back(2 * M_PI * c / (1e-2 / E_cr.back()));
144         lambdacr.push_back(2 * M_PI * c / omegacr.back() * 1e9);
145     }
146
147     inputFile.close();
148
149 std::vector<double> OmegaExTable = omegacr;
150 std::vector<double> GammaExTable = Gammacr;
151 std::vector<double> JExTable = Jex;
152
153
154 const int num_points = 300000;
155 const double lambda_min = 500.0e-9;
156 const double lambda_max = 800.0e-9;
157
158 double lambda_step = (lambda_max - lambda_min) / (num_points - 1);
```

```
159
160 std::vector<double> lambdaL;
161 std::vector<double> OmegaL;
162 std::vector<double> Scalar_real;
163 std::vector<double> Vector_real;
164 std::vector<double> Tensor_real;
165 std::vector<double> Scalar_imag;
166 std::vector<double> Vector_imag;
167 std::vector<double> Tensor_imag;
168 std::vector<double> Werte;
169
170 for (int ind = 0; ind < num_points; ++ind) {
171     double lambda = lambda_min + ind * lambda_step;
172     double Omega = 2 * M_PI * c / lambda;
173     lambdaL.push_back(lambda);
174     OmegaL.push_back(Omega);
175
176     Werte = GlobalEnergyShift_L(J0, JExTable, GammaExTable, OmegaExTable, OmegaL[ind]);
177     Scalar_real.push_back(Werte[0] / atomic_unit);
178     Vector_real.push_back(Werte[1] / atomic_unit);
179     Tensor_real.push_back(Werte[2] / atomic_unit);
180     Scalar_imag.push_back(Werte[3] / atomic_unit);
181     Vector_imag.push_back(Werte[4] / atomic_unit);
182     Tensor_imag.push_back(Werte[5] / atomic_unit);
183 }
184
185 std::string filename = "Resonance_cpp.txt";
186 writeDataToFile(filename, lambdaL, Scalar_real, Vector_real, Tensor_real, Scalar_imag,
        Vector_imag, Tensor_imag);
187    return 0;
188 }
```

Listing 5: Calculation of the real and imaginary part of the scalar vector and tensor polarizability of dysprosium in a variable wavelength interval. The results are saved in a .txt file.

List of Figures

List of Tables

Listings

Acronyms

2D	Two dimensional
3D	Three dimensional
BS	Beam splitter
BEC	Bose-Einstein condensate
BNC	Bayonet Neill Concelman
DM	Dichroic mirror
DPS	Differential pumping stage
Dy	Dysprosium
FOV	Field of view
FWHM	Full width at half maximum
HV	High vacuum
IR	Infrared
IVP	Initial value problem
MOT	Magneto optical trap
NPBS	Non polarising beam splitter
OSM	Open-Short-Match
ODT	Optical dipole trap
PBS	Polarising beam splitter
PET	Polyethylene terephthalate
PLA	Polylactide
PV	Peak to valley
RF	Radio frequency
RWE	Reflected wavefront error
RMD	Root-Mean-Square deviation
RWA	Rotating wave approximation
SF	Small field
TTL	Transistor–transistor logic
UHV	Ultra high vacuum
VdW	Van der Waals

References

[Lam83] Horace Lamb. “XIII. On electrical motions in a spherical conductor”. In: *Philosophical Transactions of the Royal Society of London* 174 (1883), pp. 519–549.

[Fes58] Herman Feshbach. “Unified theory of nuclear reactions”. In: *Annals of Physics* 5.4 (1958), pp. 357–390. ISSN: 0003-4916. DOI: https://doi.org/10.1016/0003-4916(58)90007-1. URL: https://www.sciencedirect.com/science/article/pii/0003491658900071.

[MC61] William Frederick Meggers and Charles H Corliss. *Tables of spectral-line intensities*. Vol. 32. National Bureau of Standards, 1961.

[Kur65] Kaneyuki Kurokawa. “Power waves and the scattering matrix”. In: *IEEE transactions on microwave theory and techniques* 13.2 (1965), pp. 194–202.

[Not72] Agilent Application Note. “154: S—Parameter Design”. In: *Hewlett-Packard, Palo Alto, CA* (1972).

[FDG74] J Ferch, W Dankwort, and H Gebauer. “Hyperfine structure investigations in DyI with the atomic beam magnetic resonance method”. In: *Physics Letters A* 49.4 (1974), pp. 287–288.

[HR76] David I Hoult and RE Richards. “The signal-to-noise ratio of the nuclear magnetic resonance experiment”. In: *Journal of Magnetic Resonance (1969)* 24.1 (1976), pp. 71–85.

[Gus+79] M Gustavsson et al. “Lifetime measurements for excited states of rare-earth atoms using pulse modulation of a cw dye-laser beam”. In: *JOSA* 69.7 (1979), pp. 984–992.

[Mat79] R. A. Matula. “Electrical resistivity of copper, gold, palladium, and silver”. In: *Journal of Physical and Chemical Reference Data* 8.4 (Oct. 1979), pp. 1147–1298. ISSN: 0047-2689. DOI: 10.1063/1.555614. eprint: https://pubs.aip.org/aip/jpr/article-pdf/8/4/1147/11982514/1147_1_online.pdf. URL: https://doi.org/10.1063/1.555614.

[Pea81] G Peach. “Theory of the pressure broadening and shift of spectral lines”. In: *Advances in Physics* 30.3 (1981), pp. 367–474.

[SSJ82] GM STORR, LA SMITH, and RE JOHNSTONE. “Applied Biological Sciences”. In: *Nature* 300.23130 (1982), p. 23130.

[Gia84] D Giancoli. *25: Electric Currents and Resistance; Physics for Scientists and Engineers with Modern Physics*. Tech. rep. ISBN 0-13-149508-9, 1984.

[VMK88] D A Varshalovich, A N Moskalev, and V K Khersonskii. *Quantum Theory of Angular Momentum*. WORLD SCIENTIFIC, 1988. DOI: 10.1142/0270. eprint: https://www.worldscientific.com/doi/pdf/10.1142/0270. URL: https://www.worldscientific.com/doi/abs/10.1142/0270.

[And+95] Mike H Anderson et al. “Observation of Bose-Einstein condensation in a dilute atomic vapor”. In: *science* 269.5221 (1995), pp. 198–201.

[Hor98] Joseph P. Hornak. *The basics of NMR*. 1998. URL: https://www.cis.rit.edu/htbooks/nmr/bnmr.htm.

[TWK98] Manfred Thumm, Werner Wiesbeck, and Stefan Kern. *Hochfrequenzmesstechnik*. Springer, 1998.

[Dal+99] Franco Dalfovo et al. “Theory of Bose-Einstein condensation in trapped gases”. In: *Reviews of modern physics* 71.3 (1999), p. 463.

[DK99] Nikolai Borisovich Delone and Vladimir P Krainov. “AC Stark shift of atomic energy levels”. In: *Physics-Uspekhi* 42.7 (1999), p. 669.

[GWO00] Rudolf Grimm, Matthias Weidemüller, and Yurii B Ovchinnikov. “Optical dipole traps for neutral atoms”. In: *Advances in atomic, molecular, and optical physics*. Vol. 42. Elsevier, 2000, pp. 95–170.

[NG00] Gillian Nave and Ulf Griesmann. “New energy levels and classifications of spectral lines from neutral and singly-ionized dysprosium (Dy I and Dy II)”. In: *Physica Scripta* 62.6 (2000), p. 463.

[Vis+00] Ram Viswanath et al. “Thermal performance challenges from silicon to systems”. In: *Intel Technology Journal* 4.3 (2000), pp. 1–16.

[FS01] Alexander L Fetter and Anatoly A Svidzinsky. “Vortices in a trapped dilute Bose-Einstein condensate”. In: *Journal of Physics: Condensed Matter* 13.12 (2001), R135.

[GGP02] Stefano Giovanazzi, Axel Görlitz, and Tilman Pfau. “Tuning the dipolar interaction in quantum gases”. In: *Physical review letters* 89.13 (2002), p. 130401.

[Lev02] Barbara Goss Levi. “From Superfluid to Insulator: Bose–Einstein Condensate Undergoes a Quantum Phase Transition”. In: *Physics Today* 55.3 (2002), pp. 18–20.

[Hen+03] S Hensler et al. “Dipolar relaxation in an ultra-cold gas of magnetically trapped chromium atoms”. In: *Applied Physics B* 77 (2003), pp. 765–772.

[SM03] Endre Süli and David F Mayers. *An introduction to numerical analysis*. Cambridge university press, 2003.

[Web+03] Tino Weber et al. “Three-body recombination at large scattering lengths in an ultracold atomic gas”. In: *Physical review letters* 91.12 (2003), p. 123201.

[Bau04] Philip Baumeister. *Optical coating technology*. Vol. 137. SPIE press, 2004.

[Lid04] David R Lide. *CRC handbook of chemistry and physics*. Vol. 85. CRC press, 2004.

[Col05] Edward Collett. “Field guide to polarization”. In: Spie Bellingham, WA. 2005.

[Ein05] Albert Einstein. “Quantentheorie des einatomigen idealen gases. zweite abhandlung”. In: *Albert Einstein: Akademie-Vorträge: Sitzungsberichte der Preußischen Akademie der Wissenschaften 1914–1932* (2005), pp. 245–257.

[Kra06] Phillip-Tobias Kraemer. *Few-body interactions in an ultracold gas of cesium atoms*. na, 2006.

[Pre+07] William H Press et al. “Numerical recipes in C++”. In: *The art of scientific computing* 2 (2007), p. 1002.

[Ste07] Daniel A Steck. *Quantum and atom optics*. 2007. URL: http://www.nadirpoint.de/Physik_Lit_PDF/62.pdf.

[BDZ08] Immanuel Bloch, Jean Dalibard, and Wilhelm Zwerger. “Many-body physics with ultracold gases”. In: *Reviews of modern physics* 80.3 (2008), p. 885.

[Cla08] Richard A Clarke. “Magnetic properties of materials”. In: (2008). URL: http://info.%20ee.%20surrey.%20ac.%20uk/Workshop/advice/coils/mu.

[Gau08] GaussianBeam. 2008. URL: https://gaussianbeam.sourceforge.net/.

[KS08] Fritz Kurt Kneubühl and Markus Werner Sigrist. *Laser*. Springer-Verlag, 2008.

[Fra09] Alexander Franzen. “ComponentLibrary (a vector graphics library for illustrations of optics experiments)”. In: (2009). URL: https://www.gwoptics.org/ComponentLibrary/.

[Mat09] Jermey NA Matthews. “Commercial optical traps emerge from biophysics labs”. In: *Physics Today* 62.2 (2009), pp. 26–28.

[Phi09] Thompson Phillips. *Dynamo-Electric Machinery; a Manual for Students of Electrotechnics*. BiblioBazaar, LLC, 2009.

[Chi+10] Cheng Chin et al. “Feshbach resonances in ultracold gases”. In: *Reviews of Modern Physics* 82.2 (2010), p. 1225.

[Kla+10] Jan Klaers et al. “Bose–Einstein condensation of photons in an optical microcavity”. In: *Nature* 468.7323 (2010), pp. 545–548.

[Krz+10] Kowalski Krzysztof et al. “Magneto-optical trap: fundamentals and realization”. In: *CMST* 2 (2010), pp. 115–129.

[Pas+10] B Pasquiou et al. “Control of dipolar relaxation in external fields”. In: *Physical Review A* 81.4 (2010), p. 042716.

[Ems11] John Emsley. *Nature’s building blocks: an AZ guide to the elements*. Oxford University Press, USA, 2011.

[LYL11] Mingwu Lu, Seo Ho Youn, and Benjamin L Lev. “Spectroscopy of a narrow-line laser-cooling transition in atomic dysprosium”. In: *Physical Review A* 83.1 (2011), p. 012510.

[Mar11] Michael Margraf. *QucsStudio – ein freier und leistungsstarker Schaltungssimulator*. 2011. URL: http://qucsstudio.de.

[Sch+13] M Schmitt et al. “Spectroscopy of a narrow-line optical pumping transition in atomic dysprosium”. In: *Optics Letters* 38.5 (2013), pp. 637–639.

[Sta+13] P. T. Starkey et al. “A scripted control system for autonomous hardware-timed experiments”. In: *Review of Scientific Instruments* 84.8 (Aug. 2013), p. 085111. DOI: 10.1063/1.4817213. URL: https://doi.org/10.1063%2F1.4817213.

[CK14] Fritz Caspers and Piotr Kowina. “RF measurement concepts”. 2014.

[Kar14] Klaus W Kark. *Antennen und Strahlungsfelder: Elektromagnetische Wellen auf Leitungen, im Freiraum und ihre Abstrahlung*. Springer-Verlag, 2014.

[Gur15] Gurgel. *University of Hamburg HF-Radar Home Page*. Nov. 2015. URL: http://wera.cen.uni-hamburg.de/DBM.shtml (visited on 04/25/2023).

[MLB15] Joël Mispelter, Mihaela Lupu, and André Briguet. *NMR probeheads for biophysical and biomedical experiments: theoretical principles and practical guidelines*. World Scientific Publishing Company, 2015.

[Son15] Sony. *IMX249LLJ/IMX249LQJ Diagonal 13.4mm (Type 1/1.2) 2.35M-Effective Pixel Monochrome and Color CMOS Image Sensors*. 2015. URL: https://www.phase1vision.com/userfiles/product_files/imx249lqj_llj_flyer.pdf (visited on 09/08/2023).

[Li+16] Hui Li et al. “Optical trapping of ultracold dysprosium atoms: transition probabilities, dynamic dipole polarizabilities and van der Waals C6 coefficients”. In: *Journal of Physics B: Atomic, Molecular and Optical Physics* 50.1 (2016), p. 014005.

[Str16] Frieder Strauß. *Grundkurs Hochfrequenztechnik*. Springer, 2016.

[Dre17] Davide Dreon. “Designing and building an ultracold Dysprosium experiment: a new framework for light-spin interaction”. PhD thesis. Paris Sciences et Lettres (ComUE), 2017.

[Li+17] Hui Li et al. “Anisotropic optical trapping as a manifestation of the complex electronic structure of ultracold lanthanide atoms: The example of holmium”. In: *Phys. Rev. A* 95 (6 June 2017), p. 062508. DOI: 10.1103/PhysRevA.95.062508. URL: https://link.aps.org/doi/10.1103/PhysRevA.95.062508.

[Min17a] Mini Circuits. *Datasheet - Absorptive SPDT RF Switch ZASWA-2-50DRA+*. 2017. URL: https://www.minicircuits.com/pdfs/ZASWA-2-50DRA+.pdf (visited on 08/16/2023).

[Min17b] Mini Circuits. *Datasheet - High Power Amplifier LZY-22+*. 2017. URL: https://www.minicircuits.com/pdfs/LZY-22+.pdf (visited on 04/27/2023).

[Nat17] Gabriele Natale. “Spin physics in dipolar quantum gases of erbium atoms”. 2017.

[Pol17] Claudia Politi. “Optical dipole trap for an erbium and dysprosium mixture”. PhD thesis. Master’s thesis (Università di Pisa, 2017.

[GS18] David J Griffiths and Darrell F Schroeter. *Introduction to quantum mechanics*. Cambridge university press, 2018.

[Ilz+18] P Ilzhöfer et al. “Two-species five-beam magneto-optical trap for erbium and dysprosium”. In: *Physical Review A* 97.2 (2018), p. 023633.

[LLC18] IDEX Health Science LLC. “Practical Flatness - Understanding Laser Dichroic Performance”. In: (2018). URL: https://www.idex-hs.com/docs/default-source/tech-notes/practical-flatness---tech-note.pdf?sfvrsn=17e8d8c7_3.

[Klu19] J Kluge. “Design of a Zeeman slower for a second generation experimental setup on quantum degenerate Dysprosium gases”. PhD thesis. Master’s thesis, Universität Stuttgart, 2019.

[Wal20] Florian Wallner. “New tools for controlling strontium atoms with high spectral and spatial resolution”. PhD thesis. Technische Universität München, 2020.

[Göl21] Christian Amos Gölzhäuser. “Building a new Dy quantum gas experiment”. Ruprecht-Karls-Universität Heidelberg, 2021.

[Pat+21] Alexander Patscheider et al. “Observation of a narrow inner-shell orbital transition in atomic erbium at 1299 nm”. In: *Physical Review Research* 3.3 (2021), p. 033256.

[Sca+21] F Scazza et al. “An efficient high-current circuit for fast radio-frequency spectroscopy in cold atomic gases”. In: *arXiv preprint arXiv:2104.12730* (2021).

[Cho+22] Lauriane Chomaz et al. “Dipolar physics: A review of experiments with magnetic quantum gases.” In: *Reports on Progress in Physics* (2022).

[Gao22] Jianshun Gao. “A First Two-Dimensional Magneto-Optical Trap for Dysprosium”. Ruprecht-Karls-Universität Heidelberg, 2022.

[Han+22] Stephan Handschuh-Wang et al. “The subtle difference between Galinstan (R) and eutectic GaInSn”. In: *Materialia* 26 (2022), p. 101642. ISSN: 2589-1529. DOI: https://doi.org/10.1016/j.mtla.2022.101642. URL: https://www.sciencedirect.com/science/article/pii/S2589152922003234.

[Hoe22] Lennart Hoenen. “Fast, High Precision Low Noise Bipolar Power Supply for Magnetic Field Coils in Ultra-Cold Dysprosium Experiment”. Ruprecht-Karls-Universität Heidelberg, 2022.

[Len22] Paul Lennart. “An Optical Dipole Trap with Tunable Geometry for Dysprosium”. Ruprecht-Karls-Universität Heidelberg, 2022.

[Sch22] Joschka Hannes Schöner. “Magnetic-Field Setup for Magneto-Optical-Trapping and Interaction-Tuning in Novel Dysprosium Quantum Gas Experiment”. Ruprecht-Karls-Universität Heidelberg, 2022.

[All23] Allied Vision. *GigE VISION CAMERAS Mako User Guide*. 2023. URL: https://cdn.alliedvision.com/fileadmin/content/documents/products/cameras/Mako/techman/Mako_TechMan_en.pdf (visited on 09/08/2023).

[Bou23] Thibault Bourgeois. *Tailorable optical trap with Digital Micromirror Device for Dysprosium experiment*. 2023.

[Dre23] Charles Drevon. *Caractérisation d’un réseau optique en accordéon pour une expérience de gaz quantique dipolaire en dimensions réduites*. 2023.

[Sal23] Valentina Salazar. “The Accordion Lattice: Towards Trapping of Dysprosium Ultracold Gases in Two Dimensions”. Ruprecht-Karls-Universität Heidelberg, 2023.

[Wel+23] K Welz et al. “Anomalous loss behavior in a single-component Fermi gas close to a p-wave Feshbach resonance”. In: *Physical Review A* 107.5 (2023), p. 053310.

Acknowledgments

At the end of this thesis, I wanted to thank several people that accompanied me along this incredible journey of writing my Bachelor Thesis. First and foremost, I would like to express my deepest gratitude to my supervisor Prof. Dr. Lauriane Chomaz. I am indescribably grateful for the warm welcome into the Quantum Fluids group and the opportunity to actually contribute to one of the most promising experiments in ultracold atom physics. I have been able to contact her at any time with questions, and could rely on receiving a very detailed answer and extensive help. This was not only limited to physics related matters regarding my Bachelor's thesis, but also applied to other topics such as stays abroad, the choice of my Master's university or other private matters. I know that this is anything but a matter of course and I can say with certainty that joining her working group is one of the best things that could have happened to me. Her example and trust in me was motivating and led me to discover my passion for research and to learn an extremely broad range of new things in the course of this bachelor thesis. I wish her and her research group all the best and am deeply convinced that she will make an invaluable contribution to the research community. I would be delighted if our paths crossed again at another time and look forward to seeing the further development of her research group.

Secondly, I would like to thank Prof. Dr. José Ramon Crespo López-Urrutia for agreeing to do the second correction of my Bachelor thesis. It was a pleasure to meet him in the seminar Key Experiments in Quantum Mechanics and I would like to thank him here again for his patience in answering my questions about my lecture topic as well as a richly diversified and exciting composition of his seminar.

Next I thank my working group, which supported me in all situations. I would like to thank Shuwei Jin in particular for supporting me in the implementation of my projects and for the fact that I could always approach him. No matter whether I needed space on the optical table in the preparation laboratory, help with an order, a 3D print or help with the technical drawings, he always made time for me.

I thank Jianshun Gao for his constant helpfulness and patience. I could ask him about almost any topic and always received a detailed answer. He ignited the blazing fire of passion for programming in me and it was his idea to integrate my animations into my Bachelor Thesis by means of a website and QR codes. Through his advice, I migrated the calculations of the polarizabilities from Python to C++, which resulted in a time saving of a factor of 20 for me. I am also grateful to him for educating me about the difference between *real* Chinese food and restaurants with „China“ in the name.

I also thank Karthik Chandrashekara for his helpfulness in countless situations. He had shown me around the lab on my first day in the group and tried to explain the entire experimental setup to me with a lot of patience. His adventurousness for group activities is a real enrichment and his supportive nature extends beyond the university context. I also remember a lot of fun German lessons where we deciphered the safety instructions of the charcoal briquettes together. *Wird ein Grill in Innenräumen betrieben, stellt eine erhöhte Kohlenmonoxid-Konzentration eine besondere Gefahr dar!*

I thank Christian Gölzhäuser for the tip to write at least 300 words every day. Without his advice, the bachelor thesis would not have become what it is. I also remember a fun time winding coils, which turned out to be a physical test of endurance due to the repetitive and slow motion (and a hard to turn lathe).

Joschka Schöner only returned from his stay abroad towards the end of my thesis, although he had previously worked in the working group as a Master's student. In fact, however, we had already

been in contact beforehand, as he convinced me with very persuasive arguments at the working group inspiration fair to take up a project internship in Laurianes group. I am deeply grateful to him for introducing me to such a nice and open minded working group.

Sarah Philips has always listened carefully to my explanations about e-scooters and my dream of one day creating a P-scooter powered by kerosene and a valveless pulsejet engine. She supported me especially at the beginning in the working group when everything was still new to me and at the end of my thesis with my optics setup in the lab. Despite a fiber coupling efficiency of $\leq 2.5 \cdot 10^{-3}\,\%$ she encouraged me and gave me strength to continue for roughly three more hours until I exceeded 50%.

I would like to thank Charles Drevon that during a joint e-scooter ride I was able to spark in him the joy of this means of transport. The next time we meet, we will have an intense race with 20 $\mathrm{km/h}$ maximum speed. He was also one of the few people who understood the charm of working at night in the university in a similar way to myself.

I thank Thibault Bourgeois who, together with Charles and on Sarah's initiative, gave lectures on the French language at lunchtime. A key moment was when Sarah and I realised that French pronunciation almost always leaves out the last letters. Also, thank you for trying to make me understand the French education system and introducing us all to a *more natural way* of throwing a bowling ball.

I also thank Britta Bader, who completed her Bachelor Thesis at the same time as me and with whom I was sharing an office. I always enjoyed working with her and she was always happy to help me with any problems. It was a pleasure to talk to her about literature and I had a great time with her book recommendations. Even extreme situations like the invasion of our office by „Susie“ (a mouse) could be handled by us without any problems.

I had the pleasure of meeting Wyatt Kirkby towards the end of my thesis. Even though the time we knew each other was rather short, I remember many funny and interesting conversations over lunch. Also, his droplet formation animations inspired me to improve the quality of my animations despite a computation time of several hours (which is however negligible compared to the time the droplet formation requires). I wish him all the best in his future career as a postdoc in the Dy Lab team!

I thank all past members of the Dy Group. Their contribution to the experiment was an inspiration for me to find a solution even for complex problems. In particular, I would like to thank Lenny Hoenen, whose office place I was able to use during my project internship, Paul Holzenkamp and Valentina Salazar Silva, whom I was able to get to know personally.

I also thank the *secret mysterious cult* for accepting me as a recruit, which has given my life lasting meaning. For reasons of confidentiality, the names of its members are not mentioned here. The persons involved are aware of the event to which this paragraph refers.

Thanks also goes to the e-scooter company Bolt, who provided me with an inexpensive (initially 15 ct per minute) and safe way to travel home after my late night excesses in the office. The new pricing policy (25 ct per minute) has deeply devastated me, but I remain a strong advocate of the freedom that e-scooters bring.

Speaking of late night excesses: I would also like to thank Guoxian Su for his nightly company. Even though he is not an official part of our working group, we have all already accepted him as an informal member. He also impressively demonstrated to me that the university kitchen is perfectly suitable for preparing meals. I have probably never been as close to *real* Chinese food as I was in

those nights. I also thank him for the Chinese lessons at lunch, 我的名字是! Especially the explanation of the difference between „ma“ (妈), „ma“ (马), „ma“ (麻) and „ma“ (吗) was very helpful.

Many thanks also go to Kilian Welz and Michael Rautenberg from the LiCs experiment from the QD group. Their support was invaluable at the beginning of my project internship. Michael recommended the QUCS Studio software to simulate impedance matching circuits and we had many fruitful discussions. Kilian made a decisive contribution to the analytical solution of the dipolar relaxation DE and the discussions with him were of unspeakable value. I would also like to thank Eleonora Lippi, Tobias Krom and all the other members of the institute who always helped me with small things like finding a network analyser.

I thank Dr. Gerhard Zürn for the best 1-person laser safety instruction I could have imagined. Thank you for finding the time so quickly so I could start my work in the lab. The entire mechanical workshop has performed an unspeakable service for our working group, which includes not only the precision production of components, but also the provision of tools and advice on design issues. In particular, I would like to thank Andreas Düll for critically reviewing my technical drawings and Thomas Haaf for giving me a key to the physics institute, which I definitely couldn't live without in the last few months. For all the administrative work, especially at the beginning of my time in the working group, I would like to thank Claudia Krämer, who could always be contacted, also with questions like where to find a kitchen scale for weighing dichroic mirrors.

On the way to my Bachelor Thesis, I ran into countless inspiring people and made many new acquaintances and friends. In particular, I would like to thank: Cyrus Walther, the current president of the International Association of Physics Students, who showed me the possibilities of getting involved outside the university. Constantin Krause, whose position as federal president for vocational preparation in the young German Physical Society I was allowed to take over, for introducing me to his position in detail and with a lot of patience. Alexandra Beikert, who accompanied me as a tutor from the first to the third semester and was always a valuable and supportive mentor, even outside of her tutorial work. And of course also my friends in Heidelberg: Julian, Sophia, Dana, Noa, David, Jannis, Sebastian and my friends in Koblenz: Manuel, Hoang, Kevin, Yanik and Annitschka. Thank you for making studying so much more fun and your help with all sorts of different things.

Finally, I thank my family for their indescribable support on my path to physics enlightenment. Their belief in me and their willingness to help have accompanied me my whole life and made me the person I am. Without them, not only would this thesis never have been written, but also my studies in Heidelberg at Germany's oldest university would have been impossible. No matter what time of day or night, I could always rely on them and am eternally grateful to have grown up in such an environment.

Erklärung

Ich versichere, dass ich diese Arbeit selbstständig verfasst und keine anderen als die angegebenen Quellen und Hilfsmittel benutzt habe.

Heidelberg, den 09.09.2023,